Greenland Monthly Accumulation Maps (1960-2022): A Statistical Semi-Empirical Bias-Adjustment Model

Josephine Lindsey-Clark[1], Aslak Grinsted[1], Baptiste Vandecrux[2], and Christine Schøtt Hvidberg[1]

[1]Physics of Ice, Climate, and Earth, Niels Bohr Institute, University of Copenhagen, Jagtvej 132, 2200 Copenhagen, Denmark
[2]Geological Survey of Denmark and Greenland, Øster Voldgade 10, 1350 Copenhagen, Denmark

Correspondence: Josephine Lindsey-Clark (josephine.lindsey-clark@nbi.ku.dk)

Abstract.

Accurate estimates of snow accumulation over the Greenland ~~Ice Sheet (GrIS)~~ ice-sheet are essential for reliable projections of sea-level rise. These are typically obtained from ~~Regional Climate Models (RCMs)~~regional climate models, which carry ~~substantial~~ systematic temporal and spatially variable biases, contributing to ~~the metre-scale~~ substantial uncertainties in sea-level rise projections. ~~While numerous studies have evaluated RCM bias using select in-situ observational datasets, many assessments are deduced from comparison to reanalysis datasets, which too carry substantial uncertainties. Such biases stem partly from the inability of RCMs and reanalysis products to assimilate point-based in-situ precipitation measurements directly. As a result, the rich network of observations from radar, ice cores, snow pits and stake networks remains under-utilised in systematic bias-correction of model accumulation.~~

~~In this study,~~ Here we present a novel statistical-semi-empirical model for bias-correcting gridded accumulation output from any ~~RCM~~ regional climate model or reanalysis product, utilising ~~two million observational data points from the SUMup~~ the SUMup dataset, which provides the most comprehensive spatial and temporal coverage of surface mass balance ~~dataset~~observations to date. The method ~~applies an empirical orthogonal function (EOF) decomposition to~~ employs Empirical Orthogonal Function analysis to decompose the model accumulation output ~~and adjusts the mean, climatology, EOFs and corresponding principle components (PCs) through a set of coefficients. The coefficients are calibrated by using a least squares optimisation that minimises the misfit between each component of the model accumulation and the in-situ observations. This allows us to reconstruct spatially complete~~into the dominant patterns of spatial variability and their temporal evolution. Adjustment coefficients derived by fitting SUMup data enable the reconstruction of spatially complete, bias-corrected accumulation ~~maps. Here we apply this method~~ fields.

We apply this approach to monthly accumulation output from the HIRLAM–ECHAM Regional Climate Model (HIRHAM5~~(1960-2022), ; 1960–2022~~), the Modèle Atmosphérique Régional (MAR3.14; 1960–2022), the Regional Atmospheric Climate Model (RACMO 2.4p1~~(1980-2022; 1980–2022~~), and ~~CARRA reanalysis (1991-2022), identifying initial mean biases of -8.7~~the Copernicus Arctic Regional Reanalysis (CARRA; 1991–2022). Initial mean point-wise biases of -7.4% (HIRHAM), ~~+0.5% (~~-0.5% (MAR), 0.0% (RACMO) and +~~10.9~~10.1% (CARRA) ~~. After adjustment, these~~ are reduced to ~~-0.1% , -0.1% and -0.2%, respectively~~±0.3% following adjustment. Resulting bias-corrected mean annual accumulation rates over the ice sheet are estimated at ~~321~~ 469 mm yr^{-1} (HIRHAM~~, 1960-2022), 375~~), 412 mm yr^{-1} (MAR), 435 mm yr^{-1} (RACMO~~, 1980-2022) and 384~~) and 408 mm

yr^{-1} (CARRA~~,~~) between 1991-2022~~)~~. Inter-model agreement improves significantly in the observation-rich accumulation zone, with a 68% reduction in standard deviation of mean accumulation estimates, but deteriorates by 27% in the sparsely sampled ablation zone, highlighting the need for additional observational constraints. Model bias is dominated by the southern ice-sheet, with the largest contribution from the south-east for HIRHAM (43-53 Gt yr^{-1}; 35-44%) and MAR (30-34 Gt yr^{-1}; 26-27%), and the south west for RACMO (20-27 Gt yr^{-1}; 28-33%) and CARRA (34 Gt yr^{-1}; 32%). Temporal trends and temperature sensitivities exhibit a pronounced east-west contrast, with the east dominated by strong positive responses and negative responses in the west.

The framework outlined in this study offers a scalable, transferable solution ~~for enhancing accumulation estimates , applicable to other climate models, variables, regions and observational datasets. The resulting bias-corrected accumulation fields offer~~ to improve accumulation estimates through enhanced integration of observational data, providing an improved input to ice-sheet models, with the potential to reduce uncertainties in future sea-level rise projections~~through enhanced integration of observational data~~.

1 Introduction

The Greenland Ice Sheet (GrIS) has become the greatest single cryospheric contributor to present-day global sea-level rise ~~(Hofer et al., 2020; Fettweis et al., 2020; van den Broeke et al., 2016)~~(Chen et al., 2017; van den Broeke et al., 2017, 2016), accounting for approximately 22% of the ∼3.3 mm yr^{-1} total mean sea-level rise between 2002 to 2022 (Hanna et al., 2024; Jia et al., 2022). Since the mid 1990s, mass loss from the GrIS has been driven by changes in Surface Mass Balance (SMB) (Hofer et al., 2020; van den Broeke et al., 2016, 2009), overtaking ice loss from calving. SMB is defined as the mass accumulated through precipitation, minus the mass lost through meltwater runoff, sublimation, evaporation, and wind redistribution. As the ~~largest component of SMB~~only net mass input, accumulation is crucial to constrain for accurate modelling of ice-sheet evolution. However, due to the ~~high spatial and temporal complexity of precipitation patterns,~~ complexity of the processes governing precipitation, coupled with limitations in model resolution and simplified cloud microphysics, accumulation over the GrIS remains poorly constrained by models. As a result, regional climate models (RCMs) often fail to adequately capture this variability, leading to biased estimations of ice mass loss ~~(Hanna et al., 2024)~~ (Ryan et al., 2020) and substantial discrepancies between climate model projections (Otosaka et al., 2023).

~~Understanding and quantifying accumulation over the GrIS has been a long-standing challenge in polar research.~~ The first studies investigating snow accumulation began in the early 20th century, establishing techniques such as stake measurements, snow pits, and shallow cores to deduce accumulation from snow height and seasonal layering. Ice core projects starting in the late 1950s analysing stable oxygen-isotope ratios provided new insights into past climate, later leading to the systematic use of ice cores for detailed accumulation studies (e.g. Box et al., 2013, 2009; Buchardt et al., 2012; Mosley-Thompson et al., 2001; Clausen et al., 1988). ~~In the mid-1960s, the~~ The introduction of ice-penetrating radar systems in the mid-1960s to track reflections from internal ice layers revealed that stratified ice layers formed by seasonal snowfall could be used to infer accumulation rates. Unlike ice cores, snow pits and stake measurements~~–~~, which provided point observations~~–~~, radar techniques enabled continuous mapping over vast ~~areas~~regions. Early radar studies, such as (Robin et al., 1969), demonstrated the effectiveness of radar in revealing accumulation variability over broad regions, laying the foundation for further ground-based radar surveys (Hawley et al., 2014; Miège et al., 2013; Medley et al., 2013), as well as airborne campaigns (Montgomery et al., 2020; Lewis et al., 2017; Koenig et al., 2016). These advances allowed for systematic coverage of regions of the ice sheet that were previously inaccessible to in situ measurements, dramatically improving our understanding of accumulation patterns~~and spatial variability~~.

One of the earliest comprehensive efforts to synthesise a diverse range of observational data to map accumulation across the GrIS was by Ohmura and Reeh (1991). Using spatial interpolation of measurements from snow pits, ice cores and coastal weather stations, they estimated the mean accumulation ~~over GrIS~~ to be 310 mm.w.e, and provided one of the most accurate maps of accumulation over the ice sheet at the time. This influential study played a crucial role in improving understanding of how topography and weather systems influence regional snowfall patterns ~~, and the impact on the ice sheet 's~~ and ice sheet mass balance. Subsequent studies incorporated additional data with improved interpolation techniques (Cogley, 2004; Calanca et al., 2000; Ohmura et al., 1999), and enhanced understanding of regional variability (McConnell et al., 2001).

Regional climate models provided a way to estimate accumulation patterns on a spatially complete, high resolution grid (Ettema et al., 2009; Fettweis et al., 2008; Box et al., 2006; Box, 2005; Box et al., 2004). Similarly, climate reanalysis data were used to provide accumulation grids (Hanna et al., 2008, 2006, 2005), with the advantage of assimilating ~~in situ atmospheric observationssuch as~~ remotely-sensed and in-situ observations, such as atmospheric measurements of pressure and temperature (Simmons and Gibson, 2000). Reanalysis datasets could also serve as boundary conditions for RCM simulations, alongside ancillary observational datasets such as those from weather stations and remote sensing. However, both RCMs and reanalysis products inherently carry biases ~~due to limitations in model physics~~ arising from coarse spatial resolution failing to resolve complex terrain, simplified cloud microphysics schemes, and sparse observational constraints.

To address model bias, Box et al. (2006) calibrated accumulation output from the Fifth Generation Mesoscale Model for polar climates (Polar MM5) using snow pit observations, identifying and correcting for systematic errors. Expanding on these advances, Burgess et al. (2010) combined firn core measurements and meteorological station precipitation data with high-resolution Polar MM5 output to create a spatially complete reconstruction of Greenland Ice Sheet accumulation. This hybrid methodology resolved inconsistencies in earlier studies that relied on sparse datasets or models alone, providing a new accumulation grid with enhanced regional accuracy. Using spatial interpolation of linear correction functions derived by region, Burgess found a mean snow accumulation rate of 337 ± 48 mm yr^{-1} w.e, 16-21% higher than previous estimates by Ohmura et al. (1999), Calanca et al. (2000) and Cogley (2004). This increase was primarily attributed to better representation of higher orographic precipitation provided by the hybrid approach, affecting the south east in ~~particular- a~~ particular—a region with limited ice core coverage. Accumulation rates in the south-east were found to exceed 2000 mm yr^{-1} and dominate the inter-annual variability. Representing 31% of the total accumulated mass, this region was found to have a substantial impact on the ice-sheet surface mass balance as a whole~~, highlighting the importance of studying regional variability~~.

Providing one of the first spatially complete reconstructions of accumulation, Burgess et al. (2010) remains a cornerstone for understanding Greenland's climate-driven ice loss. Since then, numerous studies have continued to improve on this foundation through incorporating new observational data and enhanced model simulations (Mouginot et al., 2019; Sandberg Sørensen et al., 2018; van den Broeke et al., 2016; Khan et al., 2015; Velicogna et al., 2014; Box et al., 2013; Shepherd et al., 2012). Despite these advances, ~~SMB~~ accumulation remains a major source of uncertainty in projections of future sea-level rise (van den Broeke et al., 2009).

Ice sheet models, and thus sea-level rise projections, require spatially complete gridded accumulation maps and are therefore typically obtained from RCMs. RCMs are often validated using a combination of remote sensing data and in-situ point observations from weather stations and ~~, occasionally,~~ firn cores. ~~However, as~~ Although remote sensing technology ~~cannot accurately measure surface mass fluxes such as snowfall (Bennartz et al., 2019) and~~ can provide snowfall estimates, the accuracy of retrievals is restricted by challenges in sampling limitations and ground clutter (Ryan et al., 2020; Bennartz et al., 2019). Combined with the sparse distribution of weather stations and firn cores leaving vast regions without ~~data~~ in-situ coverage, RCM accumulation maps still carry significant uncertainties today ~~(Vernon et al., 2013)~~(Ryan et al., 2020; Vernon et al., 2013). Though in situ accumulation data from ice cores, radar, snow pits and stake measurements can fill some ~~of these~~ in-situ data gaps,

uncertainties introduced by point-to-pixel differences, coupled with challenges in aligning the inconsistent temporal resolutions, means that the full range of available data ~~remains~~ has remained under-utilised in systematic RCM validation.

Here we present a flexible statistical-semi-empirical model designed to utilise the full range of available in-situ data to bias-adjust any gridded model accumulation output. ~~The SUMup dataset (Vandecrux et al., 2024) includes a compilation of SMB data derived from a diverse range of different sources including radar, ice-core, snow pit and stake measurements, providing an extensive~~ This study advances prior work through leveraging the SUMup surface mass balance dataset (Vandecrux et al., 2024), providing the most comprehensive basis for model correction to date. Using this ~~set of over two million data points in Greenland,~~ diverse compilation of in-situ data derived primarily from ice-cores, airborne and ground-based radar, snow pits, stake measurements and automated weather stations, we produce a data cube of monthly bias-adjusted spatially complete accumulation maps. While previous studies have used techniques such as universal kriging (Ohmura and Reeh, 1991), triangulated irregular networks (Burgess et al., 2010) and least-squares regressions (Box et al., 2013) to estimate or correct model fields with point-based observations, these approaches typically do not explicitly account for patterns of both spatial and temporal bias variability.

We base our method on Empirical Orthogonal Function (EOF) decomposition of the model accumulation output~~; first centring the data to remove the temporal mean and climatology, and then computing the first 10 EOFs and corresponding Principle Components (PCs) on the anomaly matrix. The EOF modes reveal the preferred~~, which reveals the dominant patterns of spatial ~~variability captured in the model accumulation, while the principle components describe how each mode contributes to the variability through time~~and temporal variability. Utilising robust least-squares optimisation, we fit ~~the model data to the SUMup dataset~~ each component of the decomposition to SUMup observations to derive a set of coefficients which adjust each component of the decomposition. This approach enables targeted correction of the model's spatial and temporal structure~~, offering physical interpretability of how each component influences model bias. Limiting the adjustment to the first 10 EOF modes captures 90% of the variability, while avoiding over-fitting noise captured by the higher order modes.~~ .

The aim of this ~~paper~~ study is to present ~~the method alongside key data considerations, as well as providing bias-corrected accumulationmaps from three models: the HIRHAM regional climate model~~ a flexible bias-correction model for improving estimates of GrIS accumulation, which offers the potential to improve GrIS SMB estimates and downstream modelling of sea-level rise. We first present four model products to which the bias-adjustment is applied: the HIRLAM–ECHAM Regional Climate Model (HIRHAM) version 5, the Modèle Atmosphérique Régional (MAR) version 3.14, the Polar Regional Atmospheric Climate Model (RACMO) version 2.4p1, and the Copernicus Arctic Regional Reanalysis (CARRA)~~west domain. We focus on the accumulation zone, a region characterised by negligible runoff, making precipitation the most dominant component of the accumulation. While the method could be extended to adjust full SMB over the whole ice sheet with additional data, our focus here is to test the approach using key variables available across models. This ensures a consistent comparison, targetting the largest component of SMB, rather than multiple, less well constrained physical elements simultaneously. We provide an analysis~~ , followed by an overview of the SUMup dataset and key data considerations. We then provide a detailed outline of the bias-adjustment method. Results are subsequently analysed in terms of mean and seasonal

biases before and after bias-adjustment~~and~~ , and we examine the impact on long-term accumulation trends and ~~their sensitivity to temperature .~~ temperature sensitivity. Lastly, we discuss the implications and limitations of these findings.

2 Data

2.1 Gridded Model Accumulation

We present bias-corrected accumulation maps ~~from three modelsincluding two~~ for four models, including three RCMs and one reanalysis dataset: (1) the ~~HIRHAM regional climate model~~ HIRLAM–ECHAM Regional Climate Model (HIRHAM) version 5 ~~, forced with ERA5 reanalysis (Hersbach et al., 2020) between January 1960 to December 2022,~~ (Langen et al., 2017) , (2) the Modèle Atmosphérique Régional (MAR) version 3.14 (Fettweis et al., 2020), (3) the Polar Regional Atmospheric Climate Model (RACMO) version 2.4p1 ~~also forced with ERA5 reanalysis, between January 1980 and December 2022, and (3~~(van Dalum et al., 2024), and (4) the Copernicus Arctic Regional Reanalysis (CARRA) ~~data between January 1991 and December 2022. For each model, accumulation is obtained by merging the total precipitation (rainfall and snowfall) with the evaporation and sublimation fields, providing an appropriate representation of net accumulation within the accumulation zone. The specific variable names for each model are stated below. All output~~ dataset (Schyberg et al., 2020). All models are forced with ERA5 (Hersbach et al., 2020) at their lateral boundaries. As none of the models are coupled with an ice-sheet model, the ice extent and topography are fixed through the simulations. Output data is obtained at monthly temporal resolution~~.~~ , with accumulation approximated using SMB components excluding runoff. The implications of this approximation relative to SUMup observations are discussed in section 2.3.

2.1.1 HIRHAM5 Regional Climate Model (1960-2022, 5.5 km)

HIRHAM5 (DMI et al., 2017), is the fifth ~~version of the HIRHAM~~ generation of the HIRHLAM-ECHAM regional atmospheric climate model, which combines the dynamics of the HIRLAM model (Undén et al., 2002) with the physical parametrisation schemes of the ECHAM model (Roeckner et al., 2003). ~~The model~~ Over the Greenland domain used here, HIRHAM5 is run on a horizontal rotated latitude–longitude grid with ~5.5 km ~~horizontal resolutionover the Greenland/Iceland domain. The precipitationand evaporation /sublimationfields are the variables named 'pr', which includes rainfall and snowfall, and 'evspsbl'–evaporation including sublimation and transpiration.~~ resolution, using 31 atmospheric levels and a time step of 90 s Langen et al. (2017). The model is 6-hourly forced at its lateral boundaries by ERA5 reanalysis (Hersbach et al., 2020) which provides atmospheric fields of temperature, humidity, wind and surface pressure. ERA5 sea surface temperatures and sea-ice concentrations are prescribed at the lower boundary. HIRHAM5 has been extensively evaluated against observations over Greenland (Langen et al., 2017, 2015; Lucas-Picher et al., 2012).

In HIRHAM, SMB is parametrised as:

$$SMB_{HIRHAM} = P - E - RU, \quad (1)$$

where P is the total precipitation, E, is evaporation including sublimation, and RU is surface meltwater runoff. Excluding runoff, we define accumulation as:

$$Acc_{HIRHAM} = P - E. \quad (2)$$

2.1.2 MARv3.14 Regional Climate Model (1960-2022, 5 km)

The Modèle Atmosphérique Régional (MAR) version 3.14 (Fettweis and Grailet, 2024) couples an atmospheric module Gallée and Schayes to Soil Ice Snow Vegetation Atmosphere Transfer (SISVAT) scheme (Ridder and Schayes, 1997), including a snow model based on CROCUS (Brun et al., 1992). The snow module resolves the dominant physical processes governing snowpack evolution, including thermal stratification, densification, meltwater percolation, grain size and snow drift. The model is forced at its lateral boundaries by ERA5 in 6-hour intervals, which also provides sea surface temperatures and sea ice cover over ocean grid cells (Haacker et al., 2024).

The model configuration has been calibrated over the GrIS (Fettweis et al., 2020) and extensively validated, showing improved agreement with in-situ atmospheric measurements (Delhasse et al., 2020), remote-sensing derived melt extent (Fettweis et al., 2011) and SMB observations (Fettweis et al., 2020), compared to earlier versions.

For MAR, SMB is parametrised as:

$$SMB_{MAR} = P - SU - SW - RU, \quad (3)$$

where P is total precipitation, SU is sublimation from snow/soil, SW is surface water and RU is surface meltwater runoff. Excluding runoff, accumulation is defined here as:

$$Acc_{MAR} = P - SU - SW. \quad (4)$$

2.1.3 ~~RACMO 2.4~~RACMO2.4p1 Regional Climate Model (1980-2022, 11 km)

RACMO 2.4p1 (van Dalum et al., 2024), is a hydrostatic model that integrates the atmospheric dynamics of HIRLAM ~~(Undén et al., 2002)~~ version 5.0.3 (Undén et al., 2002) with the physical parametrisations of the ECMWF Integrated Forecasting System. ~~Here, the variables 'pr' (rainfall + snowfall), and 'evspsbl' (evaporation including sublimation and transpiration) are used~~ At the lateral boundaries, RACMO2.4p1 is forced by ERA5 reanalysis fields at 3-hourly intervals, including wind, temperature, humidity, and surface pressure, with sea surface temperature and sea-ice concentration also prescribed from ERA5. The polar version of RACMO includes specialised parameterisations for glaciated surfaces and polar boundary-layer processes, with a dedicated ice-sheet surface tile and a multilayer snow model that resolves snow metamorphism, compaction, melt, refreezing, and drifting-snow processes (Noël et al., 2018; Ettema et al., 2010). The simulations used here are taken from the R24 experiment ~~(van Dalum et al., 2024) on the~~ on a pan-Arctic domain ~~grid on a~~ following the Arctic CORDEX standard, with a horizontal grid spacing of ~11 km ~~grid~~and 40 atmospheric layers.

RACMO2.4p1 shows generally good agreement with observations over Greenland, with improved representation of cloud microphysics, precipitation, and surface mass balance compared to the previous version (R23p3) (van Dalum et al., 2024).

In RACMO2.4p1, SMB is parametrised as:

$$SMB_{RACMO} = P - SU - ER - RU, \quad (5)$$

where P is precipitation, here SU is sublimation including surface sublimation and sublimation of wind blown snow, ER is drifting snow erosion and RU is surface meltwater runoff (van Dalum et al., 2024). Excluding runoff, we define accumulation as:

$$Acc_{RACMO} = P - SU - ER. \quad (6)$$

2.1.4 CARRA Reanalysis (1991-2022, 2.5 km)

The CARRA reanalysis dataset ~~(Copernicus Climate Change Service, 2021a) is produced using the HARMONIE-AROME non-hydrostatic regional numerical weather prediction model on a~~ (Schyberg et al., 2020) is built on the weather forecast model HARMONIE, standing for HIRLAM–ALADIN Research on Mesoscale Operational NWP in Euromed, which integrates developments from HIRLAM (High Resolution Limited Area Model) and ALADIN (Aire Limitée Adaptation Dynamique Développement International) (Bengtsson et al., 2017). It is forced at its lateral boundaries by the ERA5 reanalysis (Hersbach et al., 2020) and applies three-dimensional variational (3D-Var) data assimilation to incorporate multiple datasets (Schyberg et al., 2020) , including, in Greenland, remotely sensed surface albedo (Kokhanovsky et al., 2023) and temperature, humidity, and wind speed measured by on-ice weather stations (Fausto et al., 2021; Vandecrux et al., 2023b). With 2.5 km ~~grid, providing the highest resolution gridded model data available over the Arctic. CARRA reanalysis uses~~ horizontal resolution and an improved representation of cold surfaces (Yang et al., 2020), CARRA agrees substantially better with in situ observations than ERA5 ~~global reanalysis as lateral boundary conditions for input together with additional observational data. The west domain has a 1069x1269 lambert conformal grid covering Greenland. The variable 'tp',~~ (Køltzow et al., 2022). It has been used to investigate the recent warming over the Barents Sea (Isaksen et al., 2022), Arctic sea ice (Batrak et al., 2024) and increased glacier melt in Svalbard (Schmidt et al., 2023).

In CARRA, a dedicated SMB variable is not available, and we therefore define accumulation as:

$$Acc_{CARRA} = P - E - SU, \quad (7)$$

where P is the total precipitation, ~~is merged with the variables 'eva',~~ E is evaporation, and ~~'tisef',~~ SU is the time integrated snow evaporation flux~~, which are the closest equivalent variables to 'evspsbl' used for HIRHAM and RACMO~~. Monthly data is obtained by ~~downloading~~ subtracting the 30 hour and 6 hour ~~forecasts, which are subtracted to obtain daily values and then resampled~~ daily forecasts and resampling to monthly sums.

2.2 Analysis Domain

We ~~apply a mask to restrict the analysis domain to the interior accumulation zone. This zone is defined as the area where both HIRHAM and RACMO simulate no runoff; the CARRA runoff product is excluded from this criterion due to known~~

quality issues affecting its reliability. This masked region designates where bias adjustment is performed, and only SUMup observations falling within this area are used in the analysis and discussion. We focus on accumulation rather than net surface mass balance for several reasons: (perform the bias-adjustment across the entire ice-sheet, defining a common ice mask derived from the PROMICE-2022 Ice Mask (Luetzenburg et al., 2025). This product provides a high-resolution delineation of the Greenland Ice Sheet and interior nunataks, encompassing a glacierised area of 1) observations within the accumulation zone are less impacted by melt-related uncertainties and thus are generally more reliable; (2) we gauge that the SUMup datasetdoes not provide sufficient information on melt processes to reliably constrain runoff biases; and (3) extrapolating biases derived from interior observations of SMB to lower-elevation melt zones would likely be unreliable due to differing processes and conditions. ,725,648 km^2. Mapped from August 2022 Sentinel-2 imagery, it captures the GrIS margin with greater than 20 m horizontal accuracy, offering the most up-to-date and internally consistent representation of the GrIS extent currently available. Drainage basin boundaries used are also adopted from the PROMICE dataset.

Inside We define the accumulation zone mask, where simulated runoff is zero, accumulation, Acc,is approximated as $Acc = P - E$, where P is precipitation and E is evaporation/sublimation. This approximation neglects smaller components such as melt, refreezing, wind redistribution and drifting snow erosion, which are not represented in precipitation and evaporation/sublimation variables. While SUMup observations significantly affected by melt are not included in the dataset, the cumulative influence of these un-modelled processes may contribute to model-observation discrepancies in some regions within the mask, potentially affecting the reliability of the approximationusing the mask presented in (Vandecrux et al., 2019), which applies end-of-summer snow lines from Fausto et al. (2018) to identify the minimum firn area observed between 2000-2017. This region, covering 1,405,500 km^2, corresponds to the area where snow was persistent through the 2000-2017 period, with a boundary uncertainty of 1%, estimated by shifting the firn line by $\pm$1 km (Fausto et al., 2018). Within the PROMICE ice mask, this firn area represents $\sim$80% of the ice-sheet, with the remaining $\sim$20% classified here as the ablation zone (table 1).

In RACMO2.4p1, a full SMB variable is available, which includes variables for drifting snow erosion, D, and sublimation including wind blown snow, S. RACMO SMB is defined as $SMB = P - R - D - S$ (van Dalum et al., 2024). We evaluate the performance of RACMO $P - E$ versus SMB by a point-wise comparison with SUMup data inside the mask (Table **??**) . We find slightly reduced RMSE for SMB (0.0067) versus $P - E$ (0.0068) with near identical correlation (0.91) , while absolute bias and percentage bias are smaller for $P - E$ (+1.6 mm yr^{-1},+0.5%) compared to SMB (-5.3 mm yr^{-1}, -1.7%) . The greater bias for SMB may point to uncertainties in the additional drifting snow erosion and wind blown sublimation terms,which are difficult to validate directly,or reflect measurement uncertainties in the SUMup data. Given the comparable performance,we asses that $P - E$ is sufficient for our analysis,as uncertainties in both model and observational values likely overshadow any differences observed. This choice facilitates a consistent comparison with HIRHAM,which does not include drifting snow erosion and wind-blown snow sublimation in SMB (Langen et al., 2017), and CARRA, for which a dedicated SMB product is not available.

~~Variable~~

Table 1. Ice-sheet area, accumulation and precipitation distribution across the full PROMICE ice mask (Ice sheet), the accumulation (Acc.) and ablation (Abl.) zones, shown for the 1991-2022 overlap period.

	~~Bias~~ ~~mm yr^{-1}~~	**Area** [km^2]		~~Bias~~ ~~%~~	**Accumulation** [Gt yr^{-1}]		~~R~~ **Precipitation** [Gt yr^{-1}]	
Model	~~RMSE~~ Ice sheet	Acc. (%)	Abl. (%)		Ice sheet	Acc. (%)	Abl. (%)	Ice sheet
~~RACMO P-E~~ heightHIRHAM	~~+1.6~~ 1,803,373	~~+0.5~~ 1,412,429 (78%)	~~0.91~~ 390,943 (22%)		~~0.0068~~ 805	528 (66%)	277 (34%)	837
~~RACMO SMB~~ MAR	~~-5.3~~ 1,803,203	~~-1.7~~ 1,415,090 (78%)	~~0.91~~ 388,113 (22%)		~~0.0067~~ 779	572 (73%)	207 (27%)	836
RACMO	1,839,800	1,411,192 (77%)	428,608 (23%)		820	555 (68%)	265 (32%)	853
CARRA	1,790,894	1,424,244 (80%)	366,650 (20%)		808	607 (75%)	200 (25%)	883

~~Model mean bias, correlation (R), and root mean square error (RMSE) before bias-adjusting with SUMup data. Bias is expressed both in mm yr^{-1} and as the mean percentage deviation from in-situ observations.~~

2.3 SUMup In-Situ Observational Data

The SUMup collaborative database is a compilation of in situ measurements of SMB as well as subsurface temperature and density for the Greenland and Antarctic ice ~~sheet~~ sheets from published and unpublished sources (Vandecrux et al., 2024). The 2024 edition contains, in ~~an~~ a harmonised format, more than 2.4 million SMB values given between two dates or, if dates are unknown, between two years. Of these, over ~~1.7 million~~ 2.1 million fall within the PROMICE ice mask, >95% of which lie within the accumulation zone ~~,~~ (Fig. 1). The data are derived primarily from airborne radar (Montgomery et al., 2020; Lewis et al., 2017; Koenig et al., 2016), ground based radar (Lewis et al., 2019; Miège et al., 2013), ice/firn-cores ~~(Kawakami et al., 2023; Freitag et al., 2022a, b, c; Vinther et al., 2022; Osman et al., 2021; Lewis et al., 2019; Graeter et al., 2018; Miège~~ (Kawakami et al., 2023; Freitag et al., 2022a, b, c; Vinther et al., 2022; Osman et al., 2021; Lewis et al., 2019; Graeter et al., 2018; Miege , snow pits ~~(Kjær et al., 2021; Schaller et al., 2016; Bolzan and Strobel, 2001a, b, 1999a, b, c, d, e, f, g, 1994) and stake measurements (Dibb and Fahnestock, 2004).~~ (Kjær et al., 2021; Niwano et al., 2020; Schaller et al., 2016; Bolzan and Strobel, 2001a, b, 1999a, b, c, d, e, , stake measurements (Chandler et al., 2021, 2015; Hermann et al., 2018; Machguth et al., 2016; Dibb and Fahnestock, 2004) , SnowFox sensors (Fausto, 2021) and estimated from mass balance profiles (Machguth et al., 2016). An overview of their spatial coverage by decade and season is provided in Appendix figures A1 and A2, respectively.

To focus on constraining accumulation and not runoff, for which SUMup data are not sufficient, we filter out negative SMB observations in the ablation and percolation zones, thereby excluding measurements which may describe melt or runoff. This removes all data from automated weather stations, as well as a subset of those derived from stake measurements, SnowFox sensors records, and mass balance profiles. Any measurements that are substantially impacted by melt are already excluded in the SUMup release. Consequently, we consider the remaining observations to represent a reliable dataset for comparison with model accumulation output.

Most accumulation estimates in SUMup, particularly those derived from radar and ice cores, rely on density corrections to convert observed layer thicknesses into snow-water-equivalent values. This introduces additional uncertainty, especially where density profiles are sparse, inferred, or inconsistently applied. Prior to bias-adjustment, the SUMup data ~~is filtered to remove suspected errors, including negative radar-derived accumulation, which likely reflect~~ were inspected for potential issues,

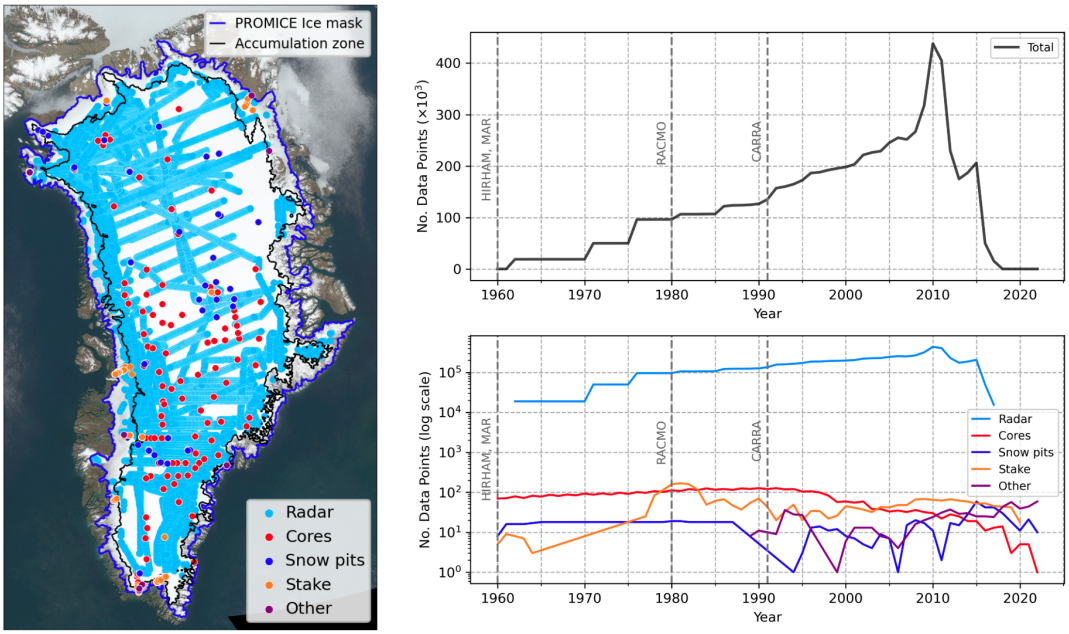

Figure 1. Left: geographical distribution of SUMup data points used in this study between 1960 and ~~2022.~~ 2022, illustrated by measurement type. The ~~colour of map markers indicate the~~ method ~~used to derive the accumulation data, with the total number of data points available for each method~~ type ~~in this time period~~ 'other' includes mass balance profiles and SnowFox sensors. Right upper: time dependence of total number of data points with markers for the start year of model data. Right lower: time dependence of data points by measurement ~~method~~type, with counts in log scale.

including inconsistencies resulting from processing or calculation errors. ~~After detailed inspection of data from Koenig et al. (2016), we identified that accumulation estimates derived from the 2009 and 2010 surveys appeared largely unrealistic, containing many values either less than half or more than double the corresponding model estimates and also contradicting other measurements in the SUMup dataset. Koenig et al. (2016) also reported worse statistics for 2009 and 2010 than for other years, when comparing radar-derived values to accumulation from the MAR regional climate model. Consequently, we assume that values from the 2009 and 2010 surveys are subject to improper horizon identification or density assumptions and are excluded from the analysis. Additionally, Koenig et al. (2016) state that the picked end-of-melt-season horizons could be assigned an approximate date of 1st July. Based on multiple examples of melt or rain events in late July (Tedesco and Fettweis, 2020), August (Box et al., 2022) and some time as late as October (Harper et al., 2023), the date of these horizons in the 2024 SUMup release was set to 1st September. Lastly, we~~ For example, we found discrepancies between the timestamps associated to accumulation values in Miège et al. (2013)~~and~~, the related dataset Miege et al. (2014) and those reported in the SUMup 2024 release. After testing ~~several possibilities~~alternative interpretations, pre-summer start and end dates were set to 1st January ~~,~~ ~~while~~ and 31st December, respectively, and post-summer start ~~dates are~~ and end dates were set to 1st January the following year ~~. Similarly, pre-summer end date are changed to~~ and 31st ~~December of the previous year and post-summer end date are~~

changed to 31st December, respectively. This interpretation , based on typical seasonal snowfall patterns, was seen to improve the consistency with the rest of the dataset and model estimates.

Fig. 1 shows the geographical distribution of SUMup data points used in this study and their time dependence. A breakdown of their spatial coverage by decade is provided in Fig. A1 in the Appendix.

The temporal resolution of the in-situ SUMup data varies between method types, where ice core and radar measurements are primarily based on annual and : ice cores, mass balance profiles and radar estimates (with the exception of surface layers) provide annual to multi-annual periods. Snow pit measurements are provided at varying resolution between 8-12 months, while stake measurements cover between 1-9 months. As shown in table 2, the vast majority of data points are annual averages; snow pits span between 5-12 months; stake measurements range from daily up to two years; and snowfox sensors record at weekly intervals. Sub-monthly data are resampled to monthly sums to match the temporal resolution of the model outputs. Annual or multi-annual means , making up 84-88% . comprise ~80% of the resulting data (Table 2).

Measurement start and end dates are rounded to the nearest month start/end to align with the monthly model outputs. In cases where this rounding produces a mismatch of greater than 15% of the total measurement duration, the data is excluded to avoid introducing artificial biases from temporal misalignment. For measurements where only the start year and end year are provided in the SUMupdataset, new start date and end date fields are introduced based on reported in SUMup, start and end dates are inferred from the original studies if statedpossible. For example, some sources measuring cores with H_2O_2 dating use the distance between summer peaks to derive annual accumulation (e.g. Kjær et al., 2021), while others use the mid-winter peak peaks (e.g. Miège et al., 2013). When start and end dates are not explicitly details of measurement dating are not provided in the source text, default values corresponding to the first and last days of the reported year(s) are assigned. This applies to 3748% of entries for HIRHAM (1960–2022), 28% for RACMO (, 43% for 1980–2022), and 18% for CARRA (, and 37% for 1991–2022). Dates are rounded to the nearest month start/end to limit the temporal precision to monthly resolution to match the temporal precision of the RCM output. 2022.

We assign a dating uncertainty to every SUMup record to account for errors in the time bounds of each SMB measurement, stated in months. This uncertainty is taken from the original study, if stated, otherwise, a default value is assigned based on commonly stated dating uncertainties in studies using similar methods. For radar and ice/firn-core measurements, we assign a dating uncertainty of 12 months ,to account for the possibility of a missed annual layer. Snow pits, for which precise start dates are unknown, are assigned a dating uncertainty of 2 months, while stake measurements and snowfox sensors, which have defined start and end dates are given a dating uncertainty of 0. Estimates from mass balance profiles are also assigned an uncertainty of 0. The dating uncertainty is assigned to each measurement as a gaussian implemented as a Gaussian weighted uncertainty distribution, allowing the measurements model output to be bias-adjusted with the monthly RCM data against each measurement within the given uncertainty range.

The latitude and longitude coordinates of each measurement are then matched with the nearest grid cell from the respective model. To reduce computational time required for the fitting, radar data points from the same source and year range–which are thus not independent–are grouped and averaged within grid cells. This leads to a different number of individual data points for fitting each model due to their different spatial resolutions. As illustrated in table 2, for the same 1991-2022 period, HIRHAM

Period	Model	Annual/multi-annual	Sub-annual	Monthly	Total
1960–2022	HIRHAM	~~92,743 (88.0~~98,181 (83.2%)	~~12,487 (11.8~~19,690 (16.7%)	~~161~~ 191 (0.2%)	~~105,391~~ 118,062
	MAR	97,296 (82.3%)	20,765 (17.6%)	191 (0.2%)	118,252
1980–2022	HIRHAM	~~77,770 (86.0~~82,779 (80.7%)	~~12,487 (13.8~~19,589 (19.1%)	~~161~~ 191 (0.2%)	~~90,418~~ 102,559
	MAR	82,423 (79.8%)	20,664 (20.0%)	191 (0.2%)	103,278
	RACMO	~~34,139 (85.8~~36,621 (80.1%)	~~5,466 (13.7~~8,888 (19.4%)	~~161~~ 191 (0.4%)	~~39,766~~ 45,700
1991–2022	HIRHAM	~~69,643 (84.6~~74,199 (79.1%)	~~12,478 (15.2~~19,402 (20.7%)	~~161~~ 191 (0.2%)	~~82,282~~ 93,792
	MAR	74,097 (78.2%)	20,477 (21.6%)	191 (0.2%)	94,765
	RACMO	~~30,062 (84.3~~32,254 (78.4%)	~~5,457 (15.3~~8,701 (21.1%)	~~161~~ 191 (0.5%)	~~35,680~~ 41,146
	CARRA	~~150,862 (85.1~~160,588 (79.5%)	~~26,200 (14.8~~41,210 (20.4%)	~~161~~ 191 (0.1%)	~~177,223~~ 201,989

Table 2. Number and percentage of observational data points fitted for each model and time period by type and total.

~~has 69,643 points for the fitting, while RACMO with lower resolution has 30,062, and CARRA has 150,862–over twice as many HIRHAM and over five times as many as RACMO. This approach effectively smooths radar data to a greater degree for the lower-resolution models.~~

~~Fig. **??** shows a point-wise comparison of each SUMup data point (with radar values averaged within grid cells)~~ The latitude and longitude coordinates of each measurement are then matched with the ~~corresponding model grid point value. With respect to the SUMup data , HIRHAM shows a negative percentage bias and standard deviation of the three models, underestimating mean annual accumulation by -8.3% with a standard deviation of 85.3 mm yr^{-1} for the 1991-2022 overlap period. RACMO exhibits the lowest mean bias of 1.3%, and a standard deviation of 81.0 mm yr^{-1} for the same period, which is lower for the 1980-2022 period at 0.5%. CARRA shows the greatest positive bias of +10.9%, and the lowest standard deviation of 79.6 mm yr^{-1}. These differences likely reflect a combination of model resolution, parametrisation schemes, as well as potential issues with observational data, which are discussed in greater detail in section 4. A small number of points with anomalously high negative bias—visible as secondary and tertiary peaks in the log-scale histogram (Fig. **??**)—originate from airborne radar estimates by Koenig et al. (2016) and Montgomery et al. (2020). These may arise from an incorrect density conversion or missed annual layers in radargrams, resulting in two or more years of accumulation being recorded as one. Apart from the data from the Koenig et al. (2016) 2009 and 2010 surveys that we discarded, we could not find specific criteria to isolate these potentially erroneous measurements, and since the radar-derived SMB observations bring a highly valuable spatial coverage, we retain the remaining radar measurements~~nearest grid cell for each model. Radar data points from the same source and year range, which are thus not independent, are grouped and averaged within grid cells, reducing the computational time for the fit. This leads to a different number of individual data points for fitting each model due to their differing spatial resolutions (Table 2). This approach effectively smooths radar data to a greater degree for the lower-resolution models.

~~Left: histogram of model bias before bias-correction (model - SUMup data) covering the full time period of available data for each model. Right: table showing the mean bias for different time periods.~~

3 Methods

3.1 EOF analysis

~~The EOFs are obtained by performing~~ Our method relies on Empirical Orthogonal Function (EOF) analysis, performed via a Principle Component Analysis (PCA) on ~~the masked RCM accumulation output~~ model accumulation output within the PROMICE ice mask, using the eofs.xarray module from the ~~eofs~~ *eofs* Python library (Dawson, 2016).

~~The model data~~The model output, $\mathbf{X}(x,y,t)$, is first centred by removing the temporal mean, $\mathbf{M}(x,y)$, and the climatology, $\mathbf{C}(x,y,m)$, where $\mathbf{C}$ is the mean deviation of each month, m, from the temporal mean~~:~~

$$\mathbf{C}(x,y,m) = \frac{12}{N_t}\sum_{i=1}^{N_t/12}(\mathbf{X}(x,y,12(i-1)+m) - \mathbf{M}(x,y)),$$

~~where $m = \mathrm{month}(t)$ and N_t is the total number of months. The centred data, $\mathbf{X}'(x,y,t)$ is thereby expressed as:~~

$$\mathbf{X}'(x,y,t) = \mathbf{X}(x,y,t) - \mathbf{M}(x,y) - \mathbf{C}(x,y,m).$$

. The EOFs, $\mathbf{EOF}(x,y)$, reveal the preferred patterns of spatial variability, while the principle components, $\mathbf{PC}(t)$, describe their monthly temporal evolution for each mode, i.

~~The centred data, $\mathbf{X}'(x,y,t)$, is masked to the accumulation zone and rearranged into matrix form $\mathbf{X}'$, where each row (i) corresponds to a time index, and each column, (j), represents a location, (x_j, y_j), within the mask. As the regional model grids are optimised for near-equal area, no area weighting is applied during the analysis.~~

~~To compute the EOFs, the covariance matrix, $\mathbf{\Psi}$, of the anomalies, $\mathbf{X}'$, is calculated as:~~ The reconstructed model accumulation, $\mathbf{Acc}(x,y,t)$ can thereby be expressed as:

$$\mathbf{\Psi}\mathbf{Acc}(x,y,t) = \frac{1}{N_t - 1}\mathbf{X}'^{\mathrm{T}}\mathbf{X}'\mathbf{M}(x,y,t) + \mathbf{C}(x,y,m) + \sum_{i=1}^{N}\mathbf{PC}_i(t)\cdot\mathbf{EOF}_i(x,y). \quad (8)$$

The ~~EOFs are derived by solving the eigenvalue problem, $\mathbf{\Psi E} = \mathbf{EA}$, where the eigenvectors, $\mathbf{E}$, are the EOFs and $\mathbf{A}$ are the eigenvalues arranged in a diagonal matrix. The EOFs are ordered by their corresponding eigenvalues such that the first EOF captures the greatest amount of variance in the data. The Principle Components (PCs) are obtained by projecting the centred data onto the EOFs:~~

$$\mathbf{PC} = \mathbf{E}^T\mathbf{X}',$$

~~where each column of $\mathbf{PC}$ represents the time series of the corresponding mode, expressing how much each mode contributes to~~ EOF computation is weighted by the ~~variability through time. The PCs are computed at the temporal resolution of the RCM, which is monthly in this analysis.~~

~~The reconstructed RCM accumulation, $\mathbf{RCM}(x,y,t)$ can thereby be expressed as:~~

$$\mathbf{RCM}(x,y,t) = \mathbf{M}(x,y,t) + \mathbf{C}(x,y,m) + \sum_{i=1}^{N}\mathbf{PC}_i(t)\cdot\mathbf{EOF}_i(x,y).$$

square root of the fractional area of each cell to ensure that the covariance-based EOFs reflect area-averaged variability. In this study, ~~the~~ we limit the adjustment to the first 10 EOF modes~~are used, capturing over 90~~, capturing 86-91% of the variance in ~~each of the models~~the output, while avoiding over-fitting noise captured by the higher order modes. Using a truncation such as this, a truncation residual term, $\mathbf{R}(x,y,t)$, is introduced to describe the remaining variability and noise not captured by the first 10 modes. Further details of the EOF method are provided in appendix A1.

~~It is common to de-trend data prior to EOF decomposition to prevent a long-term linear or low-frequency signal from dominating the leading modes. However, as accumulation trends vary strongly by region and no clear trend was seen to dominate the PCs, there was no advantage in removing a single linear trend over the accumulation zone as a whole. By not de-trending the data, the resulting modes can reflect both the variability and long-term evolution, allowing the bias-adjustment to account for trends in a way that appropriately scales with the rest of the data.~~

~~To extrapolate values beyond the accumulation zone mask, EOF maps for the full ice-sheet, $\mathbf{EOF}_{\text{full}}$, are calculated using the PCs derived from the EOF decomposition of the accumulation zone. For the full ice sheet, the anomalies, $\mathbf{X}'_{full}(x,y,t)$ can be expressed as:~~

$$\mathbf{X}'_{full}(x,y,t) = \sum_{i=1}^{N_t} \mathbf{PC}_i(t) \cdot \mathbf{EOF}_{full,i}(x,y).$$

~~Eq. A4 is projected onto $\mathbf{PC}_i(t)$ and rearranged to obtain an expression for $\mathbf{EOF}_{full,i}(x,y)$:~~

$$\mathbf{EOF}_{\text{full},i}(x,y) = \frac{\mathbf{PC}_i(t) \cdot \mathbf{X}'_{full}(x,y,t)}{\sum_{i=1}^{N_t} \mathbf{PC}_i^2}.$$

3.2 The model

The SUMup dataset is used to find a set of coefficients to adjust each component of the ~~reconstructed model accumulation~~ accumulation reconstruction, derived by fitting the in-situ SUMup data points using the python package scipy.optimize.least_squares for least-squares optimisation (Virtanen et al., 2020).

~~We introduce a set of parameters to adjust the mean and EOFs (temporally independent) and climatology and PCs (temporally dependent) components of the reconstruction.~~ The bias-adjusted reconstructed accumulation, $\mathbf{Acc}(x,y,t)$ is ~~thereby~~ then expressed as:

$$\mathbf{Acc}(x,y,t) = a_0 + \mathbf{M}(x,y,t) + b_0\mathbf{C}(x,y,m) + \sum_{i=1}^{10} (b_i\mathbf{PC}_i(t) + a_i)\,\mathbf{EOF}_i(x,y) + \mathbf{R}(x,y,t), \quad (9)$$

where a_0 adjusts the ~~temporal~~ mean, $\mathbf{M}(x,y)$, a_i adjust the EOFs, $\mathbf{EOF}_i$, b_0 adjusts the climatology, $\mathbf{C}$, b_i adjusts the PCs, $\mathbf{PC}_i$, and the truncation residual term, $\mathbf{R}$ is not adjusted. The initial guess (no adjustment) is set to 0 for the time-independent a parameters and 1 for the time-dependent b parameters. Using 10 ~~EOFS, there are~~ EOFs results in 22 ~~unknowns.~~ free parameters.

The dominant EOF patterns and associated PCs are often interpreted in terms of physical processes that drive climate variability, however, here they are solely used to create a smooth, reduced-dimensional basis for bias estimation.

We minimise the misfit between ~~the~~ SUMup observations and ~~the modelled grid-point values using a residual formulation that accounts for the varying temporal coverage of the observational data. To ensure that each data point contributes appropriately to the overall fit, we scale the residual by dividing by the number of months spanned by the observation and multiplying by twelve, normalising to an annual scale. This effectively gives~~ modelled accumulation using residuals scaled to an annual basis, giving proportionally greater weight to ~~higher resolution data containing more temporal detail.~~ higher-resolution measurements. Due to the temporal uncertainty inherent in much of the SUMup dataset, of which ~~over 84~~ ~80% consists of annual or multi-annual averages, the precise timing of individual accumulation events is often uncertain in the observations. Therefore, to prevent over-fitting and mitigate the impact of dating errors, we implement Tikhonov regularisation on the b-parameters, constraining them towards the initial guess via a ~~regularization~~ regularisation parameter λ. The optimum λ is found through 5-fold cross-validation, determined by where the average mean squared error (MSE) of the residuals is minimised. To ~~ensure that the cross-validation process accounts~~ account for potential dependencies within SUMup, we ensure that temporally or spatially linked measurements~~—~~, such as data points from the same ice core, snow pit, stake network, or radar horizon~~—~~, are grouped and assigned to the same fold during cross-validation. The ~~resulting~~ assignment of data to folds is otherwise random. The optimal λ ~~values were 12.6~~ is determined independently for each model and evaluation period. For 1991-2022 period, the cross-validation yields λ values of 8.9 for HIRHAM, 15.8 for MAR, 8.9 for RACMO, and ~~7.9 for CARRA, reflecting differences in how each model's bias structure affects the fit, as determined independently by the cross-validation procedure~~12.6 for CARRA. Over the 1980-2022 period, the corresponding values are 14.1 for HIRHAM, 11.2 for MAR, and 11.2 for RACMO, and for 1960-2022, the optimal λ for HIRHAM and MAR are again 14.1 and 11.2.

~~Several~~ To reduce the influence of outliers, several data transformation techniques, including log and arcsinh transforms, were tested ~~to reduce the influence of outliers. The impact of each transformation was~~ and evaluated using the same ~~5-fold~~ cross-validation approach~~described above~~. However, as these provided no measurable improvement in fit quality, ~~and thus~~ subsequent development and optimisation ~~of the method continued~~ was performed in linear space. As an alternative, ~~we evaluated~~ the five loss functions available in the scipy.optimize.least_squares package ~~–linear, soft_l1, huber, cauchy and arctan–~~were evaluated across a range of outlier threshold values (f_scale). ~~We found that the~~ The arctan loss function with f_scale = 1 ~~, yielded the greatest reduction in MSE for HIRHAM and RACMO, while still achieving an acceptable improvement for CARRA. Based on the residual distributions shown in Fig. **??**, we infer a high probability that observations differing by more than 1 myr~~m yr^{-1} ~~from all three models can be regarded as outliers. We therefore adopt the arctan loss function with f_scale = 1 in our final configuration.~~ was found to provide the best performance on average in MSE reduction, and was therefore adopted across all models for consistency.

3.3 ~~Bias Analysis~~

~~The coefficients derived from fitting the output data from each model are used to reconstruct the bias-adjusted accumulation according to eq. 9. As the models are bias-adjusted with SUMup data only within the accumulation zone mask,~~

3.3 Bias Analysis

Bias-adjusted mean accumulation values are provided with uncertainty intervals, estimated through spatial cross-validation. The adjustment model is trained by withholding all observations from one of the seven ice-sheet basins and validated on the remaining basin in turn. The uncertainty, σ, is expressed as the standard deviation of the seven reconstructions, R_i, relative to the ~~reconstructed data for the full ice-sheet is extrapolated using eq. A5. The model bias is presented~~ mean the full-data reconstruction, $\bar{R}$:

$$\sigma = \sqrt{\frac{1}{7}\sum_{i=1}^{7}\left(\bar{R}_i - \bar{R}\right)^2}. \tag{10}$$

This value, representing the sensitivity of the adjusted reconstructed mean accumulation to variations in the training dataset, is hereafter referred to as cross-validation uncertainty.

Model bias is quantified both as the ~~absolute~~ net difference (original mean minus bias-adjusted mean) ~~, as well as the percentage difference~~and as a relative bias, calculated at each grid point as~~the following~~:

$$Bias\ \% = \frac{\overline{X} - \overline{X'}}{\overline{X}} \cdot 100, \tag{11}$$

where $\overline{X}$ is the original model temporal mean and $\overline{X'}$ is the bias-adjusted temporal mean. ~~The seasonal bias~~Seasonal biases, grouped by winter (DJF), spring (MAM), summer (JJA) and autumn (SON), ~~is also assessed by the same metrics~~are reported in terms of relative bias.

The ~~effect of the~~ bias-adjustment is also ~~assessed~~ evaluated through analysis of ~~the~~ linear trends and ~~the~~ accumulation sensitivity to temperature, ~~both analysed~~ evaluated by grid-point-wise and domain-wide regressions. ~~The sensitivity~~ Sensitivity is defined as the percent change in accumulation per degree Celsius~~increase in temperature~~, derived from the Clausius-Clapeyron relationship (Clausius, 1850; Clapeyron, 2006) describing the saturation water vapour pressure, e_s as a function of temperature, T. Using a similar approach to Nicola et al. (2023) and Bochow et al. (2024), ~~we can express~~ the Clausius-Clapeyron relationship can be expressed as:

$$\frac{\mathrm{d}\ln e_s}{\mathrm{d}T} = \frac{L}{R_v T^2} = k, \tag{12}$$

where L is the latent heat of vaporisation, R_v is the specific gas constant for water vapour and k is the growth constant. Assuming precipitation, P, scales with the saturation vapour pressure, ~~it is common to model~~ the response of precipitation to temperature is commonly modelled via a log-linear relationship (Nicola et al., 2023; Bochow et al., 2024). ~~In this study, we~~ We extend this approach to net accumulation, ~~here defined as $(\mathrm{Acc} = P - E)$, where E represents evaporation/sublimation. We assume~~ assuming that under cold~~and/or~~, high-latitude conditions where sublimation and evaporation are ~~limited~~ minimal

relative to precipitation, accumulation approximately scales with precipitation. Therefore we fit $\ln(Acc)$ against Northern Hemisphere mean temperature anomalies from the Hadley Centre dataset (Morice et al., 2021, HadCRUT5 analysis), which combines near-surface (2 m) air temperature and sea surface temperature (SST) anomalies. The growth factor, k, is determined from the slope of the linear regression, and therefore represents the fractional change in precipitation per degree Celsius. To express this as a percent change, we define the sensitivity, s, expressed by Bochow et al. (2024):

$$s = 100 \times \left(e^{k} - 1\right), \tag{13}$$

where s is the percent change in accumulation per degree of warming.

A sensitivity analysis comparing HadCRUT5 with Berkeley Earth (Rohde and Hausfather, 2020) and GISTEMP (Lenssen et al., 2024) reconstructions confirms that the choice of dataset has negligible impact on the results over the post 1960 period investigated here.

4 Results

4.1 Bias-Adjustment ~~Parameters~~Coefficients

~~The bias-adjustment coefficients derived from fitting each of the three model outputs to SUMup SMB data within the accumulation zone mask are displayed in~~ Bias-adjustment coefficients quantify how each component of the model decomposition (eq. 9) is scaled to fit SUMup data (Fig. 2~~. Coefficients are shown for the full available model period, as well as the shorter periods of overlap. The 1991–2022 period covered by all 3 models is highlighted for comparison. Error bars reflect confidence in the fitted parameters rather than spatial variability.~~).

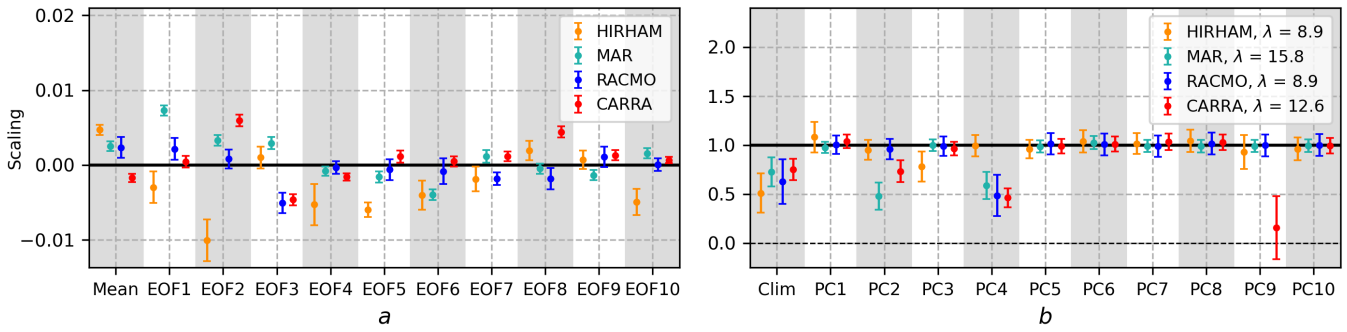

Figure 2. Bias-adjustment coefficients derived from fitting ~~HIRHAM, RACMO and CARRA data~~ the 1991-2022 overlap period using the arctan loss function~~, with error~~. Error bars ~~reflecting~~ represent the uncertainty in the parameter estimates~~. The~~, reflecting the confidence in the fitted coefficients ~~derived from each model period are highlighted separately for comparison~~rather than spatial variability. The initial guess (no adjustment) is denoted by the solid black line. Left: ~~the time-independent~~ a parameters adjusting the time-independent mean bias and 10 EOF modes. Right: ~~the~~ b ~~coefficients~~ parameters adjusting the time-dependent climatology and 10 PC modes, with λ ~~value~~ values derived ~~from~~ independently for each model via cross-validation.

Adjusting the mean, a_0 is positive for HIRHAM, MAR and RACMO, reflecting a mean negative bias, but negative for CARRA, to correct a mean positive bias. The ~~a parameters adjust spatial patterns with no temporal dependency. The coefficient adjusting the meanbias is close to 0 for all models over all periods, ranging from a minimum of -0.003 for CARRAand a maximum of 0.007 for HIRHAM between 1991-2022. This suggests that all models capture the mean accumulation relatively well relative to observations, with minimal systematic bias.~~

~~The~~ EOF coefficients ~~adjust~~ $(a_1 - a_{10})$ scale the amplitude of ~~the spatial patterns of variability . The corresponding EOF maps for the first three modes in each model can be found in Appendix~~ spatial variability patterns (EOF modes shown in appendix Fig. A5~~. Among the model~~). HIRHAM shows the greatest spread in EOF coefficients, ~~CARRA shows the greatest variation and widest error bars, with a mean deviation from the initial guess of 0.36 and a standard error of 0.41. For the same 1991-2022 period, HIRHAM and RACMO show smaller mean deviations of 0.23~~ with a standard deviation of 0.004, while RACMO shows the smallest (0.002). Differences in the EOF coefficients between models are associated with differing EOF patterns, bias structures, and ~~0.12, respectively, and smaller uncertainties with standard errors of 0.3 and 0.11~~radar grouping.

The b coefficients ~~adjust the time-dependent components of the accumulation reconstruction in eq. A3. Their values~~ are influenced by the ~~λ~~ regularisation parameter, ~~applied to penalise~~ λ, which penalises deviations from the initial guess ~~due to~~ to account for the temporal uncertainty in ~~dating the observational data and the limited number of monthly measurements (table 2). Lambda values are derived for each model individually through cross-validation. For HIRHAM, the highest lambda value of 12.6 limits deviation from the initial guessmore aggressively than for RACMO and CARRA with values of 8.9 and 7.9, respectively. This is reflected by a mean deviation from the initial guess of 0.06 for HIRHAM, 0.1 for RACMO and 0.28 for CARRA, between 1991-2022~~observational dating. Models with higher λ are more strongly constrained to remain close to the initial guess.

~~For all three models, the coefficient adjusting the climatology is within $\pm$0.1 of~~ Adjusting the climatology, b_0 is scaled down for all models to between 0.51 (HIRHAM) and 0.75 (CARRA), reflecting the smoothing of sub-annual variability due to the the ~~initial guess, leaving the seasonal signal largely unchanged. Few~~ dominance of annual/multi-annual measurements constituting ~80% of the SUMup data (table 2). Most PC adjustment coefficients $(b_1 - b_{10})$ ~~deviate substantially from their initial value~~ remain close to the initial guess of 1~~for all three models. The most notable exceptions are HIRHAM PC3, RACMO~~ , with a few notable exceptions (MAR PC2, PC4 ~~, and CARRA PCs 4 and 6, which are adjusted by 0.5, 0.2, 0.3~~for MAR, RACMO and CARRA, and ~~2 respectively.~~ PC9 CARRA). Despite the largest regularisation terms, MAR (λ=15.8) and CARRA (λ=12.6) show the greatest spread, with standard deviations of 0.18 and 0.29, respectively, driven by strong scaling of a few select coefficients.

4.2 Bias-Adjustment Assessment Metrics

~~Table 3 presents the model mean bias, correlation and RMSE before and after~~ Prior to bias-adjustment~~based on point by point comparisons–i.e., each SUMup data point (with radar values averaged within grid cells) matched with the corresponding model grid point value~~, CARRA exhibits the largest mean point-wise bias of +10.1% (Table 3), followed by HIRHAM with

a consistent negative mean bias of -7.5% to -7.4% over all fitting periods. MAR shows minimal initial mean bias (-0.5% to +0.7%), and RACMO exhibits negligible (~0%) mean bias in both the 1980-2022 and 1991-2022 periods.

Period	Model	Bias [%]	Bias_{adj} [%]	R	R_{adj}	ΔR [%]	RMSE	RMSE_{adj}	ΔRMS
1960–2022	HIRHAM	~~-8.7~~ -7.4	+0.2	0.84	0.85	+1.2	0.0108	0.0102	-5.4
	MAR	-0.5	-0.1	~~0.87~~ 0.88	~~0.90~~ 0.88	~~2.4~~ +0.7	~~0.0074~~ 0.0106	~~0.0065~~ 0.0092	~~-12.2~~ -
1980–2022	HIRHAM	~~-8.8~~ -7.5	+0.3	0.84	0.85	+1.0	0.0110	0.0105	-4.6
	MAR	-0.1	-0.0	0.88	~~0.91~~ 0.89	~~2.8~~ +0.7	~~0.0074~~ 0.0108	~~0.0063~~ 0.0093	~~-14.4~~ -
	RACMO	-0.0	+~~0.5~~ 0.1	~~-0.1~~ 0.88	~~0.91~~ 0.89	~~0.92~~ +0.5	~~0.9~~ 0.0103	~~0.0068~~ 0.0097	~~0.0062 -8~~
1991–2022	HIRHAM	~~-8.3~~ -7.4	~~-0.1~~ +0.3	~~0.88~~ 0.85	~~0.91~~ 0.85	~~3.0~~ +0.2	~~0.0074~~ 0.0111	~~0.0063~~ 0.0109	~~-15.3~~ -
	~~RACMO~~ MAR	+~~1.3~~ 0.7	-0.1	~~0.91~~ 0.89	~~0.92~~ 0.89	~~1.0~~ +0.6	~~0.0068~~ 0.0108	~~0.0062~~ 0.0093	~~-8.5~~ -1
	RACMO	-0.0	0.0	0.89	0.90	+0.3	0.0099	0.0096	-3.8
	CARRA	+~~10.9~~ 10.1	~~-0.2~~ -0.1	0.89	0.90	~~0.92~~ +0.8	~~1.8~~ 0.0092	~~0.0071~~ 0.0083	~~0.0058 -18~~

Table 3. Model mean bias, correlation (R), and root mean square error (RMSE) before and after ~~bias-adjusting~~ bias adjustment, based on a point-wise comparison with SUMup data (with radar values averaged within grid cells). Bias is expressed as the mean percentage deviation from in-situ observations.

~~Prior to bias-adjustment, CARRA exhibits the largest mean bias of +10.9%. This is followed by HIRHAM, showing negative mean bias of -8.3% to -8.8%, while RACMO exhibits a minimal initial bias of +0.5% for 1980-2022 and +1.3% for 1991-2022.~~ After adjustment, ~~the~~ mean bias is reduced to near-zero in all models~~; -0.1% for HIRHAM and RACMO, and -0.2%for CARRA, with~~ : ±0.1% for MAR, RACMO and CARRA and +0.2%-+0.3% for HIRHAM, representing substantial reductions in the ~~high initial bias for HIRHAM and CARRA. Notably, all models , including RACMO, show increased correlationafter bias-adjustment, improving by 1-3%. In addition, RMSE is reduced for all models by 8-18~~largest initial biases. All models show modest improvements in correlation, increasing by 0.3-1.2%, reduced RMSE by 1.6-14.1%, with the smallest ~~reductions for~~ improvements for HIRHAM and RACMO and the largest for ~~CARRA. A comparison of model performance against observations from 6 individual ice core sites before and after bias-adjustment is provided in Fig. ??.~~ MAR and CARRA.

4.3 Mean Accumulation and Spatial Bias Patterns

~~Fig. 3 shows spatially complete mean fields for original model values, bias-adjusted values and mean bias, expressed as the absolute difference as well as the percentage bias, calculated by eq. ??. Spatial patterns are shown here for HIRHAM (1960-2022), RACMO (1980-2022) and CARRA(1991-2022), and periods of overlap are provided in the appendix, Fig. ??. Mean values for the full periods as well as overlaps are presented in Table 4 (in mm yr^{-1}) and Table ?? in the Appendix (in Gt yr^{-1}). As the models are bias-adjusted with SUMup data only within the accumulation zone mask, detailed analysis of spatial pattern biases will be focussed on the region inside the accumulation zone mask.~~

~~Mean maps of model accumulation and bias over for HIRHAM (1960-2022), RACMO (1980-2022) and CARRA (1991-2022). Values stated in the lower corners indicate the spatial mean calculated over the accumulation zone (left) and ice sheet (right). First row: original mean model accumulation before bias-adjustment. Second row: mean bias-corrected accumulation. Third row: mean bias in mm yr^{-1}, mean(original - bias-adjusted). Fourth row: mean percentage bias, mean(original - bias-adjusted) / mean(original).~~

Before bias-adjustment, ~~the three models share a similar overall spatial pattern: low accumulationin the north-east, gradually increasing southward, with the highest values in the south and south-east, increasing rapidly towards the ice sheet margins. After bias-adjustment, this overall behaviour~~ all models share similar spatial patterns of mean accumulation. The large-scale structure of accumulation remains largely unchanged ~~, however the~~ following adjustment, however, marked differences in spatial bias patterns reveal considerable differences between models ~~. While HIRHAMunderestimates accumulation across the majority of the ice-sheet, CARRA overestimates almost everywhere. RACMO 's bias pattern shares features with both HIRHAMand CARRA, resembling HIRHAM across the northern two-thirds of the ice-sheet but appearing more similar to CARRA in the southern third. One consistent feature across all three models is a region of positive bias in the north west , where accumulation is overestimated increasingly towards the margins. This shared tendency is also seen to a lesser degree at the central west and central east margins outside of the accumulation zone.~~ (Fig. 3).

~~HIRHAM is consistently biased low over all time periods, underestimating by -12.4% in the accumulation zone and -8.4% over the entire ice sheet for the full 1960-2022 period. This bias diminishes as earlier data is excluded (4). Prior to bias-adjustment, a distinct area of low accumulation (0-100 mm yr^{-1}) is apparent in the northern part of the accumulation zone, which is no longer evident after bias-adjustment. This change is reflected in the map of percentage bias~~

HIRHAM, ~~which shows that the areas surrounding the ice divide in the north-east carry the most negative bias~~ MAR and RACMO are consistently biased low in relative mean bias over all periods (Table 4). In HIRHAM, ~~with values reaching up to -60%. The map of absolute bias reveals that the highest accumulation regions in the~~ negative bias dominates most of the ice-sheet, reaching -50% in the north and north east basins. High-accumulation regions in the south west and south east basins contribute disproportionately to net bias, where underestimation locally exceeds 150 mm yr^{-1}. MAR also underestimates across much of the ice-sheet, with biases reaching -40% in the north and north east basins, but differs from HIRHAM through a pronounced fringe of positive bias in the south and central east, exceeding 150 mm yr^{-1}. RACMO exhibits the smallest mean bias of all models, with a modest -4% underestimation over the ice-sheet in both the 1980-2022 and 1991-2022 periods. Negative relative bias is most prominent in the north east basin, reaching -30%, while high positive net occurs in the south west and central east basins, exceeding 150 mm yr^{-1}. Unlike MAR, RACMO shows a small region of negative bias along the south-east ~~also contribute significantly to model error, where HIRHAM underestimates accumulation by over 120~~ margin, reaching up to -120 mm yr^{-1} ~~towards the ice sheet margins~~.

~~RACMO shows the smallest average~~

CARRA exhibits the only mean positive relative bias of the ~~three models, underestimating accumulation by -4.9% in the accumulation zone and -1.3%~~ models, at +9% over the ice sheet~~for the full 1980-2022 period. Before bias-adjustment, RACMO also shows a distinct area of low accumulation (0-100 mm yr^{-1}) in the northern interior, which vanishes after bias-adjustment.~~

~~The strongest negative percentage bias in RACMO is likewise located in the north-east interior, reaching up to -40%. However, towards the south , a prominent positive absolute bias emerges in RACMO, where values exceed~~ . The largest net biases are similarly associated with high-accumulation regions in the south and east, with positive bias exceeding +150~~mm~~ mm yr^{-1} ~~towards~~ in the south west ~~ice-sheet margins. In contrast, a small area~~ and central east basins. Like RACMO, CARRA exhibits a narrow band of negative bias ~~is observed at the south-east margin, reaching up to -60 mm~~along the south east margin, with values exceeding -150 mm yr^{-1}.

~~CARRA shows the highest accumulation of all three models, overestimating by a mean of 8.6%~~ Low initial mean biases in MAR and RACMO reflect compensating positive and negative regions, while HIRHAM and CARRA exhibit more spatially consistent low and high biases.

Relative mean bias decreases in later fitting periods. Over the ice-sheet, HIRHAM bias reduces from -15% (1960-2022) to -13% (1980-2022) to -11% (1991-2022), MAR decreases from 13% to 8% to to 7%, while RACMO remains approximately constant. Similar trends occur in the accumulation ~~zone and 9.6% over the ice sheet. Before bias-adjustment, the area of low accumulation in the northern interior–visible in both HIRHAM and RACMO–is not present in CARRA~~ and ablation zones.

Within the observation-rich accumulation zone, inter-model standard-deviation in mean accumulation is reduced by 68% following adjustment for 1991-2022. MAR, RACMO, and CARRA converge closely, scaled down to 389$\pm$9, ~~which shows that the mean accumulation does not fall below 100~~ 389$\pm$7 and 387$\pm$6 mm yr^{-1} ~~anywhere within the accumulation zone. However, a small region with values of 0-100~~ , respectively. HIRHAM, initially at 374 mm yr^{-1} ~~does emerge after bias-adjustment. Like RACMO, CARRA exhibits its strongest positive bias in the south-west, where values exceed +150~~ , is scaled up to 404$\pm$14 mm yr^{-1} after adjustment, falling outside the uncertainty bounds of other models.

In the ablation zone, where data coverage is sparse, inter-model standard deviation increases from 68 to 86 mm yr^{-1} ~~,~~ ~~contrasted by a narrow regionof negative bias in the south east~~for 1991-2022 following adjustment, with larger cross-validation uncertainties reflecting greater spread between individual reconstructions for this region. This disparity in drives an increase in ice-sheet-wide inter-model standard-deviation from 7 mm yr^{-1} to 24 mm yr^{-1} after adjustment.

4.4 ~~Seasonal Bias Maps~~

~~Fig. 4 shows the mean seasonal percentage bias for each model over the full model period. It is important to note that 84–88% of the SUMup observations used in this study are annual or multi-annual means, with many start and end dates estimated from mid-winter or mid-summer measurement peaks. Among the sub-annual records, most span 8–10 months, where the end date is when the measurement was taken–typically between April and July–and the start date is estimated as the previous summer peak, often assumed to be 1st July (e.g. Montgomery et al., 2020; Lewis et al., 2017) or September (assigned in SUMup for snowpits from Vandecrux et al. (2023a). Only a small fraction (0.1-0.5%) are monthly measurements matching the temporal resolution of the model output. Thus, the seasonal bias patterns should be interpreted within the context of these limitations, as they are unlikely to be as robust as the long-term annual means. For this reason, only the full model periods are examined without comparisons across the overlap periods.~~ All models show their greatest contributions to absolute bias (Table 5) in the

		Ice Sheet			Accumulation Zone			Ablation Zone		
Period	Model	Acc [mm yr^{-1}]	Acc$_{adj}$ [mm yr^{-1}]	Bias [mm yr^{-1}]	~~Bias %~~ Acc [~~%~~mm yr^{-1}]	Acc$_{adj}$ [mm yr^{-1}]	Bias [mm yr^{-1}]	~~Bias %~~Acc [mm yr^{-1}]	Acc$_{adj}$ [~~%~~mm yr^{-1}]	Bias [mm yr^{-1}]
1960–2022	HIRHAM	434	458 ± 26	−25 (−15%)	364	393 ± 18	−29 (−15%)	687	695 ± 59	−8 (−15%)
	MAR	418	393 ± 12	+26 (−13%)	393	375 ± 9	+18 (−9%)	512	459 ± 22	+53 (−28%)
1980–2022	HIRHAM	441	467 ± 27	−26 (−13%)	369	400 ± 16	−30 (−14%)	700	710 ± 65	−10 (−10%)
	MAR	424	400 ± 11	+24 (−8%)	397	380 ± 8	+17 (−8%)	523	475 ± 20	+49 (−8%)
	RACMO	440	425 ± 13	+15 (−4%)	388	381 ± 9	+7 (−5%)	612	573 ± 25	+39 (0%)
1991–2022	HIRHAM	446	469 ± 24	−23 (−11%)	374	404 ± 14	−31 (−12%)	709	704 ± 58	+5 (−6%)
	MAR	432	412 ± 12	+20 (−7%)	404	389 ± 9	+15 (−7%)	533	494 ± 23	+39 (−8%)
	RACMO	446	435 ± 10	+11 (−4%)	393	389 ± 7	+4 (−5%)	619	586 ± 21	+33 (0%)
	CARRA	451	408 ± 8	+43 (+9%)	427	387 ± 6	+39 (+9%)	546	489 ± 17	+58 (+10%)

Table 4. Mean annual accumulation over the ice sheet, accumulation zone, and ablation zone before and after bias adjustment. Adjusted accumulation values are shown with cross-validation uncertainties (eq. 10). Bias is reported as both the net (mean(original - bias-adjusted), mm yr^{-1}) and in relative (%) terms, calculated by eq. 11.

Period	Model	Acc	Acc$_{adj}$	Bias$_{tot}$	N	NE	CE	SE	SW	CW	
1960–2022	HIRHAM	~~260~~ 782	~~284~~ 827 ± 48	~~−24~~ 132	~~−12.4%~~11 (8%)	~~321~~ 16 (12%)	~~340~~ 21 (16%)	~~−20~~ 53 (40%)	~~−8.4%~~14 (11%)	6 (5%)	1
	MAR	754	708 ± 21	127	10 (8%)	17 (13%)	27 (21%)	34 (27%)	21 (16%)	7 (6%)	1
1980–2022	HIRHAM	~~265~~ 795	~~289~~ 842 ± 48	~~−24~~ 135	~~−11.7%~~10 (7%)	~~326~~ 15 (11%)	~~346~~ 22 (17%)	~~−20~~ 59 (44%)	~~−7.9%~~11 (8%)	6 (5%)	1
	MAR	765	722 ± 19	125	12 (10%)	14 (11%)	27 (22%)	33 (26%)	21 (17%)	8 (6%)	1
	RACMO	~~297~~ 809	~~296~~ 783 ± 23	~~+1~~ 81	~~−4.9%~~5 (7%)	~~375~~ 10 (13%)	~~358~~ 18 (22%)	~~+16~~ 8 (10%)	~~−1.3%~~27 (33%)	3 (4%)	10
1991–2022	HIRHAM	~~268~~ 805	~~290~~ 846 ± 43	~~−22~~ 123	~~−10.4%~~9 (7%)	~~329~~ 14 (12%)	~~348~~ 24 (20%)	~~−18~~ 43 (35%)	~~−6.9%~~17 (14%)	6 (5%)	1
	MAR	779	742 ± 21	110	11 (10%)	10 (9%)	24 (22%)	30 (27%)	18 (16%)	8 (7%)	11
	RACMO	~~301~~ 820	~~298~~ 800 ± 19	~~+3~~ 73	~~−3.5%~~4 (6%)	~~379~~ 10 (14%)	~~361~~ 18 (25%)	~~+18~~ 8 (11%)	~~−0.1%~~20 (28%)	3 (5%)	9
	CARRA	~~322~~ 808	~~292~~ 730 ± 14	~~+30~~ 108	~~+8.6%~~4 (4%)	~~384~~ 7 (6%)	~~344~~ 27 (25%)	~~+40~~ 21 (20%)	~~+9.6%~~34 (32%)	6 (6%)	8

Table 5. ~~Mean~~ Spatially integrated mean annual accumulation ~~in the accumulation zone and ice sheet~~ before (Acc) and after ~~bias~~ adjustment ~~. Bias is shown in both absolute~~ (~~mm yr^{-1}~~Accadj)~~and relative percentage~~ , with total absolute bias (~~%~~Biastot) and basin-wise contributions to Biastot. ~~Corresponding~~ All values are in Gt yr^{-1}. Accumulation and net bias for the accumulation and ablation zones are provided in Appendix Table ~~??~~ A1, with temporal evolution of net and cumulative bias shown in ~~the~~ Appendix Fig. A6.

highest accumulation regions; either in the south east (HIRHAM; 43-53 Gt yr^{-1} (35-44%, MAR; 30-34 Gt yr^{-1} (26-27%)) or the south west (RACMO; 20-27 Gt yr^{-1} (28-33%, CARRA; 34 Gt yr^{-1} (32%)), closely followed by the central east.

~~Model mean seasonal percentage bias: mean(original - bias-adjusted)/mean(original). Mean seasonal patterns are shown for HIRHAM between 1960-2022, RACMO between 1980-2022 and CARRA between 1991-2022.~~

~~For HIRHAM, the highest mean negative bias occurs during the winter and spring months, reaching up to -16%in the accumulation zone and -11%over the ice sheet. This bias is reduced in the summer, decreasing to -10.5%and -6.5%, before~~

~~increasing slightly in the autumn to 10.6% and 7.3%, respectively. The overall spatial pattern remains relatively consistent through the year, with regions of strongest negative bias around the ice divide in the northern interior and in the south. In the winter, the northern interior shows a large region where bias exceeds -50%. This area is reduced in size in the spring, reaching a maximum of -40% in small regions in the summer.~~

~~RACMO also shows the lowest mean bias in the winter and spring months in the accumulation zone, at -7%, becoming less~~

4.4 Seasonal Bias Patterns

Seasonal pattern biases show strong seasonal contrasts (Fig. 4). All models show a seasonal shift in ice-sheet wide relative mean biases, from more negative (or less positive) in colder months towards least negative or most positive in autumn. For HIRHAM, MAR and RACMO, the greatest negative ~~for the summer and autumnmonths at -4%. However for the whole ice sheet, which includes larger areas of positive bias, the winter and spring mean biases are only -2%, while the summer shows the greatest negative bias at -5%, becoming least negative in autumn at -1%. Though overall spatial patterns are relatively consistent throughout the year, maximum biases~~ biases occur in winter and spring and reach a minimum in ~~the south-west reach up to +40% in the winter and gradually decrease through the year to +20% in~~ autumn. ~~Negative biases~~ In summer, these models exhibit an expanded area of positive bias in the north ~~east are also more pronounced in the winter and spring reaching -50%, reducing to up to -40% in summer and autumn~~west, which retreats and shifts to central regions in autumn, bringing mean bias to ∼0% for HIRHAM and slightly positive for MAR and RACMO. CARRA maintains net positive mean relative bias in all seasons, with minimum values in the winter and spring, and peaking in autumn.

~~CARRA shows a consistent overall positive bias throughout the year. In the accumulation zone, the highest mean bias occurs during the autumn and summer months at +9%, reducing to +8% in the spring and winter months. Over the full ice sheet, the lowest bias is also seen in spring and winter at +9%, with the highest bias in the summer at +12%. In the winter , regions of negative bias are seen in the north and central west interior, with values in the accumulation zone between 0 and -20%. These areas reduce in size through the year, while other areas of negative bias emerge in the north-east. In the autumn, almost no areas of negative bias remain within the accumulation zone, leaving a relatively uniform and low positive bias of less than +30%.~~

4.5 ~~Temporal Trends~~

~~Fig. 5 shows the temporal trends captured in the full model data before and after bias-adjustment. The maps represent the spatial variation in trend fits, calculated by regressing each grid-point accumulation over the full data period. Below, the mean annual accumulation over the whole domain (accumulation zone or ice sheet)is plotted against time with the linear fit. Mean accumulation trends resulting from fitting the models to each of the three time periods are shown in table 6.~~

~~HIRHAM shows a positive trend across the accumulation zone between 1960-2022. The rate of accumulation increase is highest towards the south and central east margins, reaching over 30 mm yr^{-1} $decade^{-1}$. There are few small areas which show a decrease in accumulation, in the central west, north and south, all of which are outside the accumulation zone mask. This pattern remains largely unchanged~~

4.5 Temporal Trends

Spatial patterns of temporal trends reveal a pronounced east-west contrast in all models (Fig. 5). Positive trends dominate east of the central ice divide and largely negative trends to the west. This behaviour is largely preserved after bias-adjustment, ~~and is reflected by the linear trends for both domains decreasing by only 0.1 mm yr^{-1} decade^{-1}.~~ with a few exceptions. HIRHAM shows slightly expanded regions of positive trends in the north west basin, while isolated areas of positive trends present prior to adjustment in MAR, RACMO and CARRA become negative in this basin. Consequently, spatial patterns and basin-wise means (Table A2) in MAR, RACMO and CARRA show closer agreement after adjustment, while HIRHAM diverges.

~~For RACMO between 1980-2022, areas of decreasing accumulation rates are observed in the south west and along the north margin before bias-adjustment. In addition, a small pocket of sharply decreasing accumulation rates is present above areas of strong positive increasing accumulation in the south east. After bias-adjustment, the negative area in the south west are now positive, while the negative area in the north now covers a wider region, stretching further south into the accumulation zone. The adjustment decreases mean trends over the accumulation zone and ice sheet more significantly than for HIRHAM, from 5.7 mm yr^{-1} decade^{-1} and 7.4 mm yr^{-1} decade^{-1}, to 4.7 mm yr^{-1} decade^{-1} and 6.8 mm yr^{-1} decade^{-1} respectively.~~

~~CARRA (1991-2022) shows negative trends spanning most of the western ice sheet, with the exception of small areas near the north-west margins and in the south-central-west, while the north and south east are dominated by positive trends. After bias-adjustment, the negative areas are interrupted by a region of positive trends covering the central ice sheet from west to east. More positive trends appear across the centre, while larger areas of more intense negative trends exceeding -30~~

In all models, the strongest trends occur in the south-east, with basin mean values of up to 66 mm yr^{-1} decade^{-1} ~~emerge in the north west. CARRA shows the lowest mean trends of the three modelsof 1.0 mm yr^{-1} decade^{-1} in the accumulation zone and 1.8 mm yr^{-1} decade^{-1} over the ice sheet, reducing to 0.5~~ (Table A2), contrasted with strong negative means in the south west.

Ice-sheet wide mean accumulation trends are positive across all models, fitting periods, and spatial domains, and bias adjustment generally leads to a small reduction in trend magnitude (typically $\leq$2 mm yr^{-1} decade^{-1}~~and 1.5~~). Notable exceptions include HIRHAM, for which bias adjustment maintains or slightly increases trend magnitudes, and the CARRA ablation zone trend, where trends increase marginally by 0.3 mm yr^{-1} decade^{-1} ~~after bias-adjustment~~following adjustment.

~~Mean accumulation trends resulting from fitting the models to each of the three time periods are shown in 6. Accumulation trends decrease unanimously after bias-adjustment across all models and domains. For the bias-adjusted HIRHAM and RACMO data, it can be seen that trends decrease~~ MAR shows the strongest mean trends overall, coupled with the lowest p-values, while CARRA shows the weakest trends and highest p-values. Confidence intervals widen and p-values increase as earlier data ~~is excluded , while uncertainties and p-values increase. The temporal trend in bias for each model is further analysed in Fig. A6, illustrating how each model bias evolves through time.~~ are excluded from the fitting period, reflecting the reduced temporal coverage and greater influence of inter-annual variability in shorter records.

4.6 Temperature Sensitivity Analysis

		Ice Sheet		Accumulation Zone	
Period	**Model**	**Trend**	**Trend$_{adj}$**	**Trend**	
	~~mm yr^{-1} decade^{-1}~~	~~mm yr^{-1} decade^{-1}~~	[mm yr^{-1}decade^{-1}]	~~mm yr^{-1} decade^{-1}~~	[mm y
~~1960–2022~~ 1960–2022	HIRHAM	~~4.6 ± 3.5~~8.1 ± 5.9, p=0.01	~~4.5 ± 3.4~~8.1 ± 5.9, p=0.01	~~5.1 ± 4.4~~6.4 ± 4.9, p=~~0.02~~ 0.01	~~5.0 ± 4.3~~6.4 ±
	MAR	8.4 ± 5.4, p<0.01	7.7 ± 5.2, p<0.01	7.0 ± 5.1, p=0.01	6.4 ±
~~1980–2022~~ 1980–2022	HIRHAM	~~4.4 ± 6.4~~9.8 ± 9.6, p=~~0.18~~ 0.05	~~4.1 ± 6.3~~10.0 ± 9.4, p=~~0.20~~ 0.04	~~5.2 ± 8.2~~7.7 ± 8.2, p=~~0.21~~ 0.07	~~4.9 ± 8.0~~7.
	MAR	13.6 ± 9.1, p<0.01	11.4 ± 8.5, p=0.01	12.4 ± 8.5, p=0.01	10.2
	RACMO	~~5.7 ± 7.1~~10.0 ± 9.5, p=~~0.12~~ 0.04	~~4.7 ± 7.0~~9.8 ± 9.3, p=~~0.18~~ 0.04	~~7.4 ± 8.9~~8.9 ± 8.8, p=~~0.10~~ 0.05	~~6.8 ± 8.7~~8.
~~1991–2022~~ 1991–2022	HIRHAM	~~3.1 ± 10.0~~8.7 ± 15.2, p=~~0.54~~ 0.26	~~3.0 ± 9.9~~10.8 ± 13.5, p=~~0.55~~ 0.12	~~3.3 ± 13.2~~6.7 ± 12.9, p=~~0.62~~ 0.31	~~3.2 ± 12.9~~8.
	MAR	13.0 ± 14.5, p=0.08	12.0 ± 13.3, p=0.08	11.7 ± 13.8, p=0.10	10.6 ±
	RACMO	~~4.0 ± 11.4~~8.6 ± 15.1, p=~~0.49~~ 0.26	~~3.2 ± 11.1~~7.9 ± 14.6, p=~~0.57~~ 0.29	~~5.6 ± 14.6~~7.4 ± 14.1, p=~~0.45~~ 0.30	~~5.1 ± 14.2~~6.
	CARRA	~~1.0 ± 12.2~~5.1 ± 15.9, p=~~0.88~~ 0.52	~~0.5 ± 9.7~~5.0 ± 15.3, p=~~0.92~~ 0.52	~~1.8 ± 14.8~~3.9 ± 15.0, p=~~0.81~~ 0.60	~~1.5 ± 11.9~~3.

Table 6. ~~Mean temporal~~ Spatial mean linear trends ~~calculated~~ in accumulation over the ~~full time series and overlap periods~~ice sheet, accumulation zone, and ablation zone before and after bias adjustment. Trends are reported with confidence intervals and p-values. Basin-wise mean trends are provided in appendix Table A2.

~~Fig. 6 shows the results of the temperature sensitivity analysis, calculated according to eq. 12. The maps represent the spatial variation in sensitivity, s, defined in eq. 12, resulting from the grid-point wise regression of log-scaled model accumulation against northern hemisphere temperature (NHT)anomalies. White regions inside the ice sheet area are caused by negative accumulation values, which are undefined. Below, the domain-wide mean annual accumulation is plotted in log-scale against NHT anomalies with the resulting linear fit and sensitivities indicated in the legend.~~

~~Temperature sensitivity analysis for HIRHAM (1960-2022), RACMO (1980-2022) and CARRA (1991-2022). Upper: maps representing spatial patterns of sensitivity derived from grid-point wise regressions of log-scaled model accumulation against NHT anomalies. Empty grid points resulting from negative values in the accumulation are excluded in the calculation of the mean sensitivities. Lower: accumulation zone wide and ice-sheet wide mean annual accumulation (log-scaled) plotted against NHT anomalies with linear regressions and sensitivities indicated in the legend.~~

~~HIRHAM (1960-2022) exhibits the highest mean sensitivities of all three models. Before bias-adjustment, these are 8.1%K^{-1} for the accumulation zone and 7.1%K^{-1} over the ice-sheet, with areas across the central- to north-east exceeding~~ Spatial patterns of temperature sensitivity share a similar spatial structure to the temporal regressions (6). MAR shows the strongest positive sensitivities, concentrated in the north- and south-east exceeding +25 % K^{-1} ~~towards the ice-sheet margins. Negative sensitivities reaching up to 15%K^{-1} are observed in narrow regions near the north-, central- and south-western margins outside the accumulation zone, though positive sensitivitiesdominate the ice sheet overall. After bias-adjustment, mean sensitivities are reduced by 8-12% to values of 7.1%K^{-1} (accumulation zone) and 6.8%K^{-1} (ice-sheet). While the overall spatial pattern remains largely the same, the regions of highest sensitivity (>10%K^{-1})in~~ locally, while CARRA shows the most widespread negative sensitivities, reflected by the ~~north-east are slightly reduced in size and shift further east. This leaves the sensitivity across the west and south largely between 0-5%K^{-1}~~weakest mean responses (Table 7). Bias-adjustment reduces positive

sensitivities in the north west for MAR, RACMO and CARRA, resulting in near zero values for 1991-2022 (Table A3), while HIRHAM's positive trends in this region remain relatively consistent.

~~RACMO (1980-2022) shows lower mean sensitivities with values of 6.8%K^{-1} (accumulation zone) and 5.7%K^{-1} (ice-sheet) before bias-adjustment. Like HIRHAM, RACMO also exhibits areas of high sensitivity across the central- to north-east reaching up to a maximum of 25%K^{-1}, though these are slightly smaller in size and are located further inland. Areas of negative sensitivity of between 0-20%K^{-1} are present in the north-west towards the ice sheet margins, appearing more prominently than in HIRHAM. In the south, RACMO shows high positive sensitivities in the east reaching up to 20%K^{-1}, contrasted with negative sensitivities in the west up to -5%K^{-1}. After bias-adjustment, mean sensitivitiesare reduced by 27-35%, to values of 4.7%K^{-1} in the accumulation zone and 4.1%K^{-1} over~~ Mean spatial sensitivities, calculated as the grid-point average of localised responses, differ systematically from the temporal regression-derived sensitivities which reflect the ice-sheet~~. The highest positive values in the east are reduced in magnitude, now reaching up to a maximum of 20%K^{-1}. Regions of negative values in the north now reach further inland, while the region of negative sensitivity in the south-west is reduced in size.~~

~~CARRA (~~'s integrated response to inter-annual temperature variability (Table 7). With the exception of the 1960-2022 period, temporal sensitivities exceed spatial averages. For 1991-2022~~)~~, CARRA shows the lowest mean sensitivities~~of all three models, with values of~~ , with an ice-sheet-wide temporal mean approximately four times lower than MAR, and six times lower in the spatial mean.

Bias adjustment generally reduces both spatial and temporal sensitivity means (Table 7), with the exception of HIRHAM and CARRA for the 1991-2022 period and RACMO for 1980-2022, for which sensitivities increase slightly following adjustment.

Period	Model	Sensitivity	
1960–2022	HIRHAM	8.2	
	MAR	8.5	
1980–2022	HIRHAM	4.8	
	MAR	8.9	
	RACMO	6.1	
1991–2022	HIRHAM	1.2	
	MAR	6.5	
	RACMO	3.0	1.9 ~~%K^{-1} over the accumulation zone and 0.7%K^{-1} over the ice sheet before bias-adjustment. Negative sensitivities dominate~~
	CARRA	1.1	

Table 7. Mean spatial (grid-point wise) and temporal (ice-sheet wide) accumulation sensitivities derived from linear regressions of log-transformed model accumulation against HadCRUT5 NHT anomalies before and after bias adjustment. Basin-wise spatial mean sensitivities are provided in appendix Table A3.

~~Sensitivities derived from the domain-wide regressions are lower in most cases. An exception is RACMO over the ice sheet, where the domain-wide sensitivity is higher at 5.5%K^{-1} compared to the~~

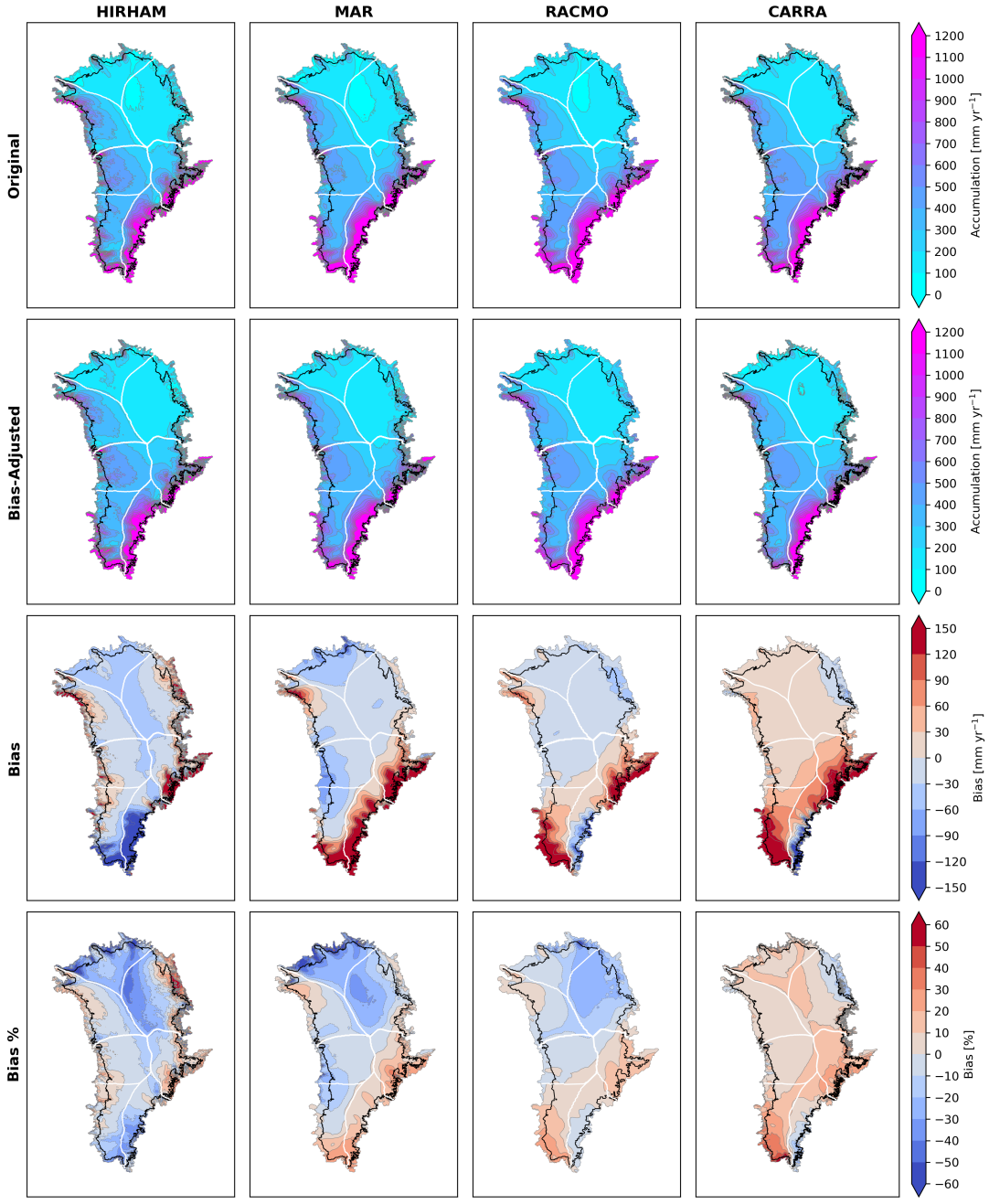

Figure 3. Mean maps of model accumulation and bias over over the 1991-2022 common period. The black line indicates the boundary of the accumulation zone. First row: original mean model accumulation before bias-adjustment. Second row: bias-corrected mean accumulation. Third row: mean bias in mm yr^{-1}, mean(original - bias-adjusted). Fourth row: mean relative bias, calculated by (eq. 11). PROMICE drainage basins boundaries are shown in white. Maps for the full model periods are provided in the appendix, Fig. A4.

~~Temporal regressions before and after bias-adjustment shown for HIRHAM (1960-2022), RACMO (1980-2022) and CARRA (1991-2022). Upper: maps showing the grid-point-wise regression representing spatial variation in linear trends. Lower: mean annual accumulation over the accumulation zone (mask) and full ice sheet with linear fits.~~

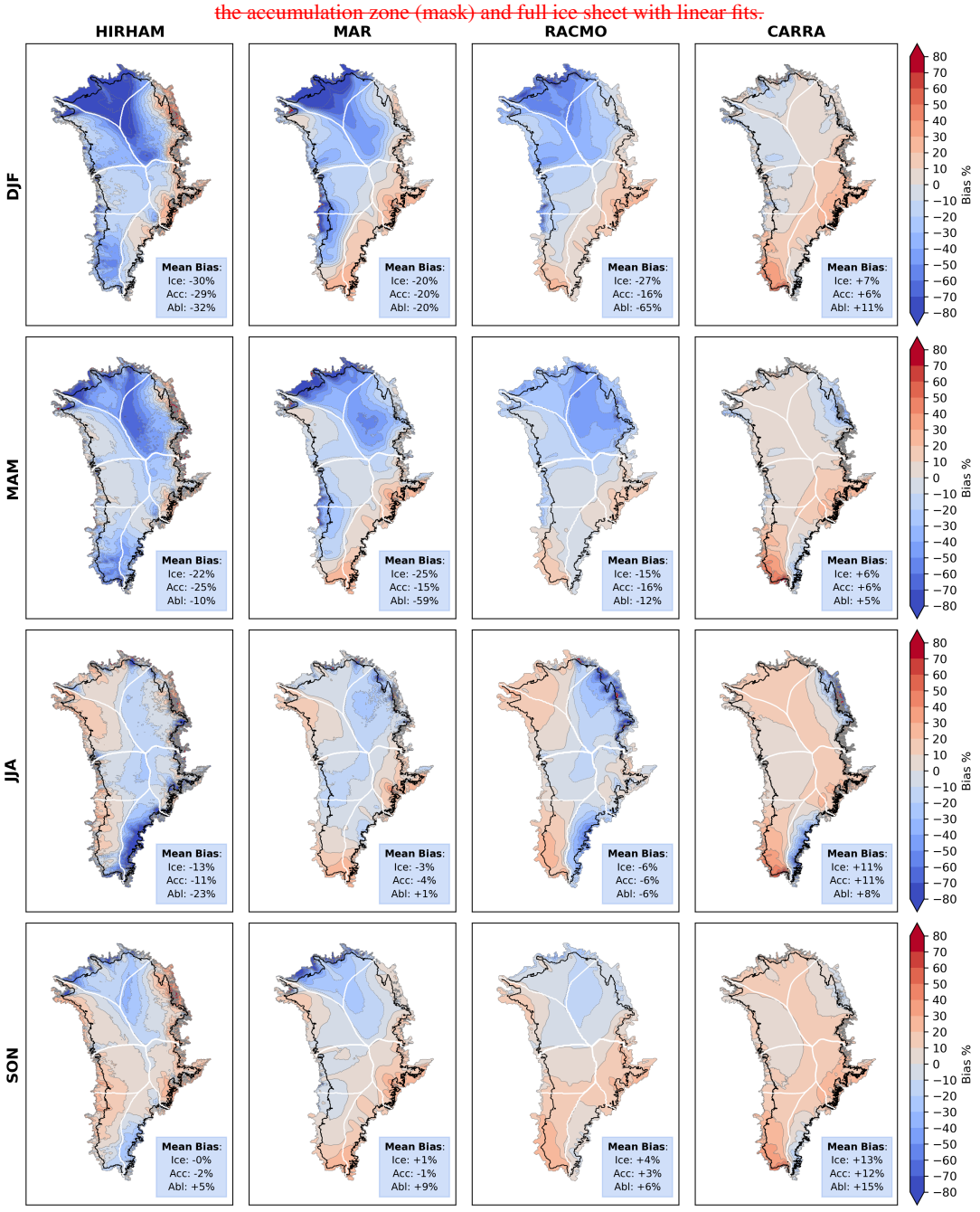

Figure 4. Model mean seasonal relative bias over the 1991-2022 common period: mean(original - bias-adjusted)/mean(original). Values stated in the lower right corners represent the mean bias for each season over the ice-sheet (Ice), accumulation zone (Acc) and ablation zone (Abl).

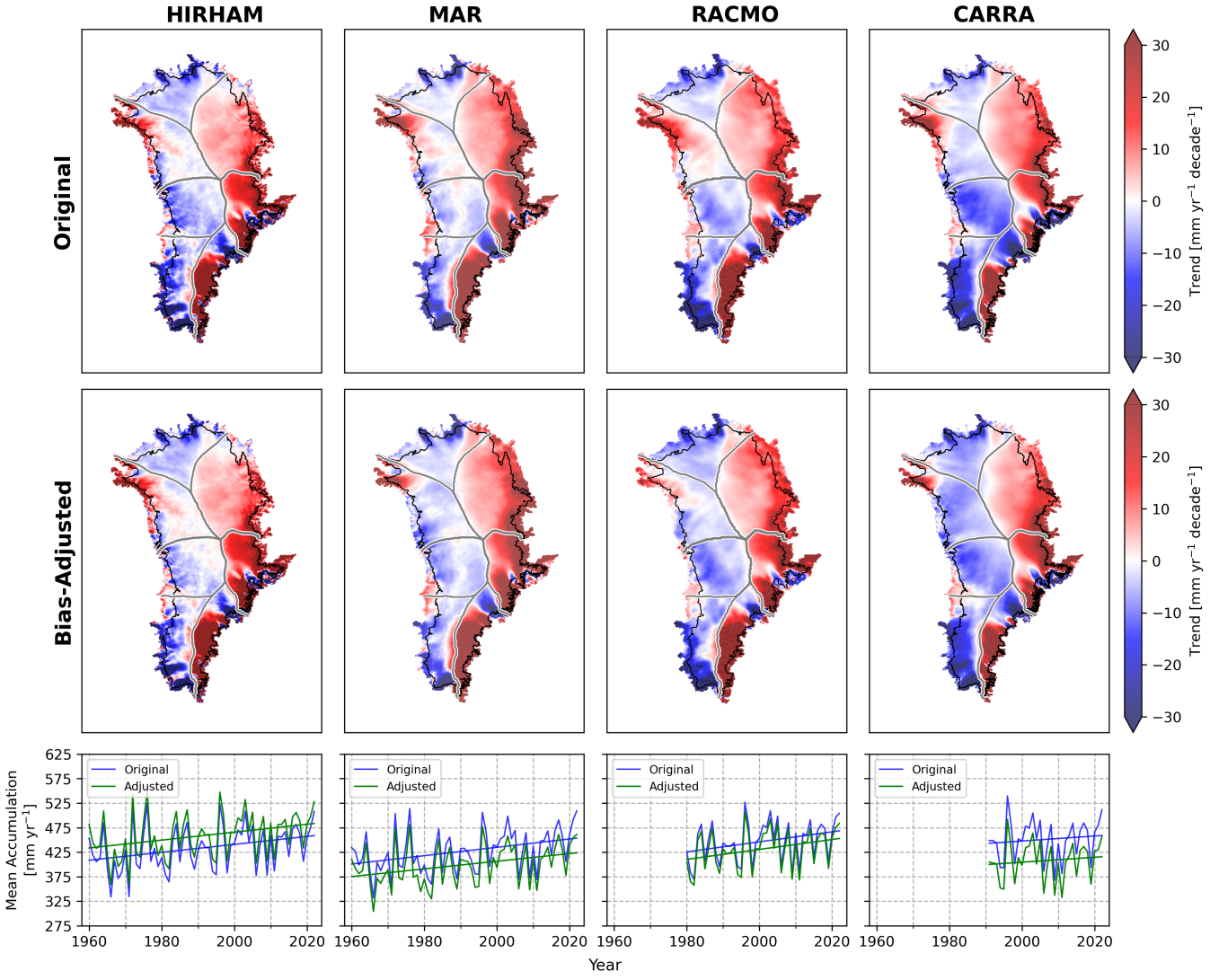

Figure 5. Temporal regressions before and after bias-adjustment. Upper: grid-point-wise regression for the 1991-2022 fitting period, representing spatial variation in linear trends. Lower: mean annual accumulation over the ice sheet with linear fits for HIRHAM (1960-2022), MAR (1960-2022), RACMO (1980-2022) and CARRA (1991-2022).

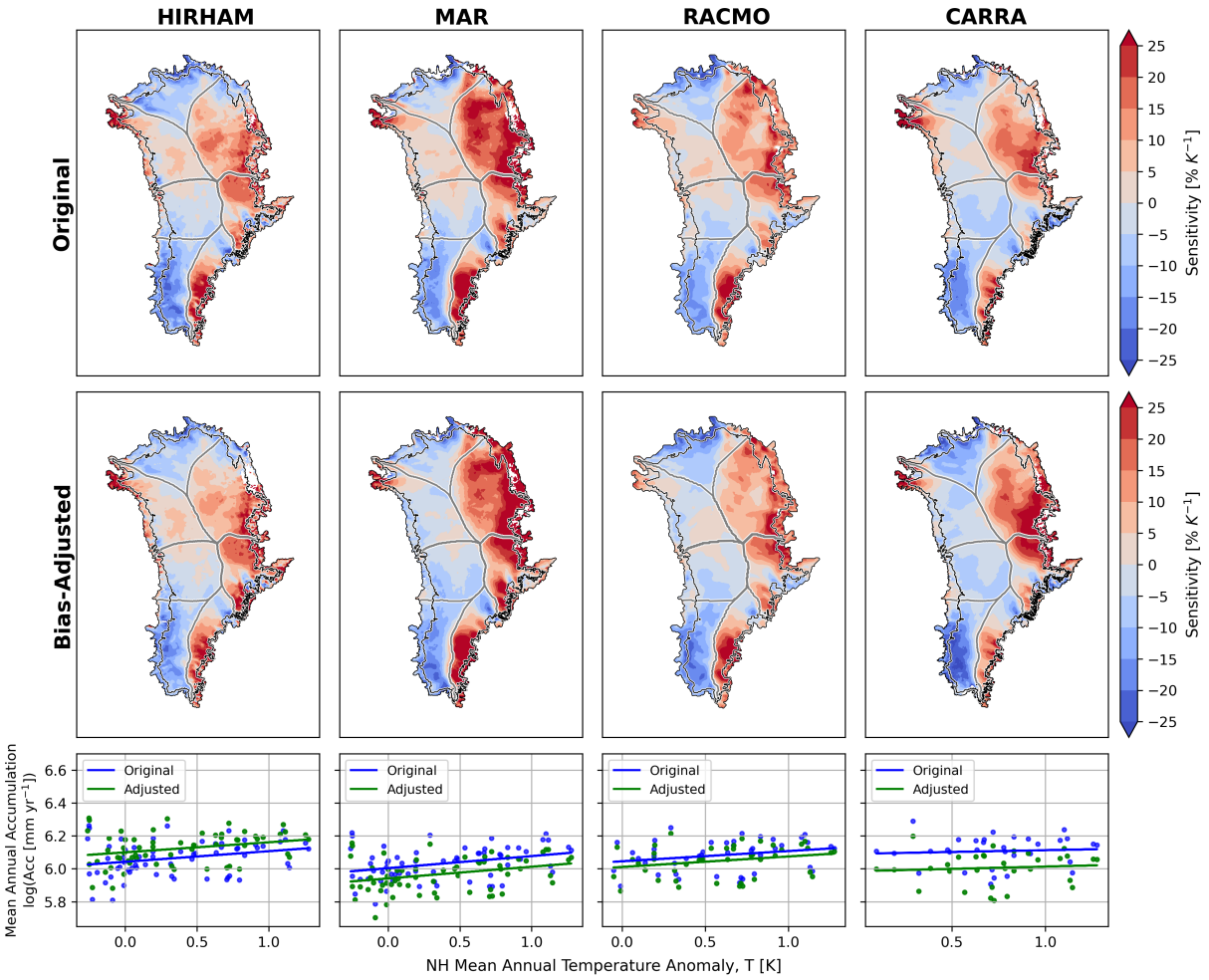

Figure 6. Temperature sensitivity analysis following eq. 12. Upper panels show spatial patterns of sensitivity over 1991-2022, derived from grid-point wise linear regressions of log-transformed annual model accumulation against NHT anomalies from HadCRUT5. Empty grid points resulting from negative accumulation values are excluded from calculation of mean ice-sheet sensitivities. Lower panels show ice-sheet wide mean annual accumulation (log-transformed) as a function of NHT anomalies with linear fits for HIRHAM (1960-2022), MAR (1960-2022), RACMO (1980-2022) and CARRA (1991-2022).

5 Discussion

5.1 Mean Bias and Seasonal Bias Patterns

The adjustment successfully reduces mean point-wise ~~mean of 4.2%K~~biases to near zero in all models (Table 3), but occasionally over-corrects, resulting in a reversal of the residual mean bias (e.g., HIRHAM from -7.4% to +0.3%). This tendency is also apparent in the mean bias-adjusted fields (Table 4), where HIRHAM, initially biased low, is scaled up, beyond the uncertainty intervals of the other models, which converge to within ± 2 mm^{-1}~~, and notably, CARRA exhibits negative domain-wide sensitivities for the accumulation zone~~.

6 ~~Discussion~~

5.1 ~~Mean Bias and Seasonal Bias Patterns~~

~~For all models ,~~ This may reflect a combined effect of the ~~bias-correction substantially improves mean percentage bias , correlation and RMSE compared to observations (3). Inter-model agreement also improves significantly, with the standard deviation between modelsdecreasing from 27 mm yr^{-1} to 4 mmyr^{-1} after adjustment. Interestingly, a consistent slightly negative bias of -0.1% to -0.2% remains in all models, despite initial positive biases in RACMO and CARRA. This demonstrates that the~~ robust loss function~~successfully limits the influence of outliers, which are mostly negative~~ , which down-weights extreme deviations while preserving overall model-data agreement, and inherent differences in each model's EOF patterns (Fig. ~~??~~). ~~As the RMSE metric gives full weight to the outliers, it thus becomes negative~~A5). Consequently, cross-validation uncertainties may be underestimated; a complementary measure could use the spread across the four bias-adjusted means, reflecting inter-model differences in addition to training sample uncertainty.

~~Despite having the coarsest resolution of the three models, RACMO, shows the lowest initial point-wise mean bias of +0.5% for the full 1980-2022 period and 1.3% for 1991-2022. Comparison of the initial accumulation fields with the bias corrected fields also shows that RACMO has the lowest mean biases, ranging from -0.1% to -4.9%~~

The influence of observational density and inter-model differences is most pronounced in the ablation zone, where high initial inter-model spread further increases after adjustment (Table 4)). This likely reflects sparse observational coverage, particularly earlier decades with as few as three stake measurements prior to 1970 (Fig. ~~3). Inspection of the spatial bias patterns, however, reveals that RACMO exhibits areas of both strong positive and negative bias. These spatial contrasts may explain its low overall mean bias, while CARRA and HIRHAM, with significantly higher mean biases, have more consistent positive and negative spatial bias patterns, respectively.~~ A1), coupled with complex topography. Previous studies have similarly found poorer agreement in the ablation area, both between models and observations (Vernon et al., 2013) and between models themselves Fettweis et al. (2020), attributing this to uncertainties in ablation processes and ablation zone extent. Although melt and refreezing are not directly investigated in this study, our findings highlight the substantial uncertainty in ablation-zone accumulation estimates.

~~CARRA exhibits the highest initial point-wise mean bias of 10.9%, as well as high mean biases in the spatially complete fields of 8.6% in the accumulation zone and 9.6% for the whole ice-sheet. With the highest resolution (2.5 km) , one would expect CARRA's accumulation estimates to be the most accurate the three models. Yet, we find it to overestimates accumulation across the majority of ice-sheet, with bias exceeding +150 mm yr^{-1} in the south west. Previous~~

In both point-wise (Table A3) and spatially-complete field comparisons (Table 4), MAR and RACMO consistently perform best on average, exhibiting the lowest RMSE and mean bias. This is consistent with Fettweis et al. (2020), who find MAR3.9.6 and RACMO2.3 outperform thirteen other models, including HIRHAM5, when comparing SMB output against ice-core observations (Fettweis et al., 2020).

In contrast, while we find CARRA, biased high by ∼10%, performs worse than both MAR and RACMO, recent studies have found that CARRA ~~outperforms other modelscompared to observations. Comparing~~ shows better agreement with observations relative to other models. Evaluating CARRA and RACMO2.3p2 ~~with~~ against daily snow depth data from 9 coastal weather stations in Greenland, van der Schot et al. (2024) report ~~that~~ correlation coefficients between CARRA and observations are generally higher than for RACMO, with no clear overestimation or underestimation from either model. Similarly, (Box et al., 2023) evaluate CARRA, ERA5, NHM-SMAP, ~~RACMO and MAR against in-situ~~ RACMO2.3p2 and MARv3.11.5 against precipitation data from ~~7 sites in southern Greenland, finding that CARRA simulations correlate highest with field data from the relatively wet sites. They note, however, that correlations at drier locations vary substantially due to limited data resulting in less robust statistics. These studies are based on small, mostly coastal datasets, and do not reflect conditions across the broader ice sheet. In contrast, our analysis of CARRA uses over 170,000 observational data points spanning the entire accumulation zone over 31 years, revealing biases that may not be captured in more localised evaluations.~~ seven automated weather stations in two regions, four of which are on the ice-sheet, finding that CARRA simulations have the lowest average bias.

The CARRA Data User Guide (Copernicus Climate Change Service, 2021b) ~~notes that the model tends to overestimates precipitation compared to in-situ observations over northern Norway, Sweden and Finland. It also highlights ,~~ highlights that the model ~~is in better~~ shows improved agreement with the observations of high-precipitation events than ERA5, whose coarser resolution ~~is not able~~ limits its ability to predict the highest precipitation amounts. ~~Hence, CARRA'~~However, they note that the model tends to overestimate precipitation compared to in-situ observations over northern Scandinavia. Higher spatial resolution models can better resolve complex topography and associated mesoscale circulation, leading to stronger orographic enhancement of precipitation (Lucas-Picher et al., 2012). While this can improve the representation of intense precipitation events, it may also result in higher mean precipitation relative to coarser-resolution products. Similar resolution-dependent increases in precipitation have been documented for regional climate models over Greenland, where downscaling from ∼5 km to ∼1 km leads to enhanced precipitation, particularly through increased rainfall contributions (Huai et al., 2022). Consequently, CARRA's tendency towards overestimation may ~~in fact~~ be linked to its higher spatial resolution ~~, which enhances its sensitivity to intense precipitation events, potentially amplifying them beyond what is observed~~and sensitivity to orographically driven precipitation extremes.

Common to all models is a strong bias in the south; a region characterised by high snowfall and mountainous topography. Previous studies have identified the south-east, in particular, as a significant source of uncertainty, due to high spatial variability,

complex orographic effects and limited observational coverage ~~(Burgess et al., 2010; Miège et al., 2013; Koenig et al., 2016). This south-eastern bias is most prominent in HIRHAM~~ (Fettweis et al., 2020; Ryan et al., 2020; Koenig et al., 2016; Miège et al., 2013; Bu

.

Notably, HIRHAM underestimates in this region by up to -40%. Lucas-Picher et al. (2012) compare HIRHAM accumulation with ice cores from Andersen et al. 2006; Banta and McConnell (2007) and Bales et al. (2009), finding southern biases generally <10%. Our analysis, using a substantially larger observational dataset including radar-derived accumulation and covering previously unsampled areas, indicates that earlier evaluations may have underestimated biases near the complex southeastern margin. ~~Langen et al. (2015) identify that while HIRHAM tends to overestimate precipitation near the coastal margin due to overly strong topographic enhancement, lee-side precipitation is underestimated, consistent with (Herrera et al., 2010). With the coastal margin excluded from our accumulation-zone-only analysis, the strong negative bias observed here may reflect this lee-side underestimation.~~

~~While HIRHAM underestimates across the southern ice sheet,~~ Basin-wise spatially integrated accumulation means (Table 5), shows that south-west basin contributes the largest fraction of the total absolute bias for RACMO and CARRA~~show only a narrow region of negative bias along the south-eastern margin, and substantial overestimation in the south-west. These contrasting bias patterns may stem from differences in how each model represents topography–particularly important in southern Greenland, where steep gradients and strong orographic effects make precipitation highly sensitive to resolution and parametrisation schemes.~~ , while the south-east dominates bias in HIRHAM and MAR (Table 5).

The northern interior of the ice-sheet ~~also contributes significantly to model~~ contributes disproportionately to relative bias in HIRHAM~~and RACMO.~~ , MAR and RACMO, with local biases (Fig. 3) of up to 30-50%. This may reveal a shared tendency between these models to underestimate accumulation at cold, dry, high elevation sites, where atmospheric moisture is limited and snowfall events are infrequent, but significant for ~~SMB~~accumulation. Langen et al. (2017) also report that at high-elevation sites, HIRHAM5-based simulations underestimate net accumulation by 8–16%.

~~It is important to consider the spatial and temporal coverage of observations used in the bias adjustment, which is illustrated by decade in Fig. A1. Although the ice-sheet interior has relatively good and consistent~~ While the north interior benefits from relatively consistent observational coverage through time, the south-east ~~lacks data prior to 2000. Additionally,~~ has sparse coverage prior to 2000 (Fig. A1), and the south-west remains ~~poorly observed throughoutthe entire period, with only a few radar profiles and three core sites~~limited throughout. As a result, adjustments in the ~~south-east~~ south are less well constrained~~in the early record, while those in the south-west rely on limited input throughout~~, particularly in earlier periods, contributing to greater uncertainty in both regions. ~~Nonetheless, the south-east has frequently been identified as a significant source of bias in earlier studies (Burgess et al., 2010; Miège et al., 2013; Langen et al., 2015; Koenig et al., 2016), supporting the need for substantial correction in this region.~~ This may contribute to the decrease in mean relative bias in later fitting periods (Table 4).

~~In table 4, mean biases for HIRHAM and RACMO are seen to decrease as earlier data is excluded, suggesting that model performance improves in more recent periods . This trend may be influenced by two factors. Firstly, SMB observations~~ Observations also become increasingly uncertain further back in time: deeper ice-core layers are more prone to miscount-

ing (Steig et al., 2005), and radar horizons are more likely to be misidentified ~~. As a result, bias adjustments based on these older data may introduce more~~(Bingham et al., 2025), which may lead the bias-correction to apply larger, possibly unnecessary, corrections. ~~Secondly~~Furthermore, the number of observations assimilated into ERA5, which provides boundary conditions for all ~~three~~ models, declines drastically in earlier decades (Hersbach et al., 2019), degrading model performance in the past.

The ~~maps of seasonal bias (Fig. 4) reveal that bias patterns are broadly consistent throughout the yearin all three models. Mean seasonal bias values, however, fluctuate slightly between seasons, to a greater degree for HIRHAM and RACMO. Greater winter and spring biases over the accumulation zone in these models may be influenced by stronger winds during the winter and spring months. As the model accumulation is here represented only by the precipitation and evaporation/sublimation fields, wind-driven processes most important in the windier winter and spring months are not accounted for, possibly contributing the higher mean bias values in these months. This seasonal shift may also reflect limitations in how the models represent precipitation processes and orographic effects with respect to storm systems~~observed seasonal shift in ice-sheet-wide biases may reflect seasonally varying climatic processes that influence model performance differently over the year. However, seasonal biases must be interpreted within the context of the temporal limitations of the observations, of which only 0.1-0.5% are monthly measurements and ~80% are annual or multi-annual means (Table 2), with start and end dates often estimated from mid-winter or mid-summer measurement peaks or melt horizons. These dating assumptions, which vary ~~considerably over the course of the year. During winter and spring , when synoptic-scale storms are more frequent and spatially complex, moisture-rich air is more likely to be lifted over steep terrain. Coarser model grids (e.g., in HIRHAM and RACMO)may struggle to fully capture the resulting higher snowfall, contributing to the stronger negative biases observed during these seasons, particularly affecting regions with complex terrain. Conversely, CARRA~~between sources, combined with the filtering of negative SMB measurements, particularly affect the robustness of spring and summer bias estimates. These factors leave a small fraction with which to reliably constrain bias patterns on a seasonal scale (Fig. A2), ~~with higher spatial resolution, shows less pronounced seasonal variability in bias , which may indicate a better representation of these processes~~making them inherently less robust than the long-term annual means.

Ice-sheet wide mean annual biases of between 4-15% (Table 4) correspond to 20-77 Gt yr^{-1} (Table A1). Although small on an annual basis, these biases accumulate substantially over time, reaching -1300 Gt (HIRHAM), 1170 Gt (MAR), 640 Gt (RACMO) and +2500 Gt (CARRA) integrated from 1991-2022, and -2800 Gt (HIRHAM) and +2900 Gt (MAR) for 1960-2022 (Fig. A6). Over a century long run, a persistent 10% bias would amount to ~8,000 Gt, sufficient to alter sea-level rise projections by approximately 25 mm by 2100 (The IMBIE Team, 2020). Using the empirical relationship between SMB and temperature from AR5 (Intergovernmental Panel On Climate Change, 2014, Chapter 13 Supplementary Material), a ~80 Gt yr^{-1} SMB deviation corresponds to an equivalent warming bias of ~1°C. This is a substantial error, especially when viewed against critical thresholds for Greenland ice-sheet stability—~~though its overall positive bias also suggests possible overcorrection. However, as discussed in section 4.4, such speculations about the sources of seasonal biasesshould be viewed within the context of the temporal limitations of the SUMup data~~such as the ~1.6°C threshold identified by Robinson et al. (2012) , beyond which the GrIS is expected to undergo irreversible long-term melt. Such biases, if uncorrected, could obscure or misrepresent the proximity to tipping points in climate projections.

5.1 Temporal Trends and Temperature Sensitivity

~~A notable outcome of~~ The tendency for the bias-correction ~~is the consistent reduction in accumulation trends across all models and time periods following adjustment. This suggests that the~~ to temper mean accumulation trends for MAR, RACMO and CARRA may indicate that these models are overly sensitive to warming air temperatures, while HIRHAM, whose trends are slightly amplified by the adjustment, may be under-sensitive. All models show strong trends in the high accumulation south, coinciding with where net biases are largest. This region is also poorly sampled in earlier periods (Fig. A1). For MAR, RACMO and CARRA, with high positive biases dominating in the south, bias-adjustment ~~tempers model-derived accumulation trends. In addition, trends are seen to decrease as earlier data is excluded (table 6). This may reflect a combination of stronger bias~~ reduces accumulation means on average, more strongly in earlier periods fitting periods. Their mean trends are also reduced after adjustment. Conversely, for HIRHAM, initially biased low in the south, mean accumulation is scaled up by the adjustment, more so in earlier periods, and its mean trend is increased. This behaviour may be the result of both stronger corrections applied to earlier, less well-constrained ~~model data and a higher density of observations in recent decades~~periods.

~~Among the models, CARRA exhibits the lowest and least significant trends, paired with wide confidence intervals and p-values of 0.8-0.9, indicating a high degree of uncertainty. Estimates derived from shorter time series are inherently more uncertain due to both the natural variability and reduced statistical confidence. In contrast, HIRHAM -~~'HIRHAM and MAR's longer historical coverage (1960–2022) provides more statistically robust estimates, supported by lower uncertainties and statistically significant p-values of <=0.01~~within the accumulation zone and 0.02-0.03 over the ice-sheet~~. These longer-term trends are more resilient to inter-annual variability, which can dominate shorter records and obscure underlying trends. As such, the longer ~~HIRHAM-based estimates,~~ records provided by HIRHAM and MAR spanning 1960–2022, likely provide the most ~~reliable assessment~~ statistically reliable estimate of long-term accumulation trends~~.~~, due to their extended temporal coverage.

~~The temperature sensitivity estimates are similarly less robust over shorter time-scales (Fig. 6). An important distinction arises when comparing the point-wise mean sensitivities to those derived from domain wide regressions below. In most cases, domain-wide sensitivities are lower, reflecting the effect of spatial averaging before performing the regression. Notably, CARRA exhibits negative domain-wide sensitivities for the accumulation zone—further reflecting the instability of trends over this shorter period. In contrast, mean sensitivities for HIRHAM and RACMO show greater consistency between the two regression approaches, supporting the robustness of their long-term sensitivity estimates.~~ Although spatial trend patterns are illustrated for the shorter 1991–2022 period, the strong consistency in the sign and structure across models suggests that the broad-scale spatial contrasts, particularly the east–west contrast and strong southern gradients, are robust features (Fig. 5).

~~The spatial pattern in the RACMO derived temperature sensitivities resembles that found by Buchardt et al. (2012), who derive sensitivities using ice cores at 52 locations across the Greenland ice-sheet. They find the highest sensitivities over the central ice-sheet of 9.2~~Similarly, spatial patterns of temperature sensitivity (Fig. 6) are largely consistent between models. The patterns identified here share several consistent features with regional sensitivities reported in Buchardt et al. (2012), who find a pronounced east-west contrast in the south. In the south-east, where Buchardt et al. (2012) report sensitivities of +8.2±~~1.0~~0.8% K^{-1}~~(central east) and 9.4±0.1~~, we find basin-mean values ranging from +5.4 to +15.8% K^{-1} (~~central west), and the lowest~~

sensitivities in the north-east (1.5Table A3). In the south-west, their reported sensitivity of -4.0±2.80.1% K^{-1}) and north-west (6.7±0.2, corresponds to predominantly negative basin-mean sensitivities of -13.2 to +2.3 % K^{-1}). RACMO also shows a band of higher sensitivities across the centre, with values decreasing further north. . Similarly, in the south, where RACMO shows positive sensitivities in the eastcontrasted with negative values in the west, Buchardt et al. (2012) find a sensitivity of 8.2central east, where they find high sensitivities of +9.2±0.81.0% K^{-1} in the east and -4.0±0.1, adjusted values range from +8.1 to +20.6% K^{-1} in the west. .

5.2 EOF Analysis and Interpretation of Adjustment Coefficients

Interpretation of the EOFs and their adjustment coefficients (Fig. 2) may offer additional insights into model bias structure. The minimal adjustment of the mean bias coefficient for all three models suggests that a uniform offset is not the dominant source of error, and that biases are more effectively corrected through adjustments to the EOF and PC components. Similarly, the climatology parameter remains within In the central-west, however, where Buchardt et al. (2012) report their highest sensitivity of +9.4±0.1of the initial guess after adjustment. As the majority of the fitted data is made up of annual or multi-annual means, short-term or highly seasonal fluctuations are unlikely to be represented in the observational data, making the limited adjustment of the climatology both reasonable and expected.

The coefficients adjusting the EOFs representing spatial patterns of variability differ significantly between models. The larger variation and higher uncertainty in CARRA may point to greater sensitivity to localised processes or to internal variability as a result of the higher resolution grid. In addition, the smaller grid cell sizes have implications for the comparison between model output and observations: for radar-derived accumulation measurements which are grouped by source and averaged within grid cells, fewer measurement points are grouped within each grid cell. This leads to a greater number of points to fit for CARRA % K^{-1}, we find moderate values, which are further reduced or become negative following adjustment, ranging from -4.2 to +2.5 % K^{-1}. Conversely, we find our highest sensitivities in the north east basin ranging from +7.2 to +22.3 % K^{-1} after adjustment, while Buchardt et al. (2012) report their lowest sensitivities of +1.5±2.8% K^{-1}. These discrepancies may reflect a temporal shift in accumulation sensitivity in these regions, as Buchardt et al. (2012) derive their estimates from ice cores mostly drilled in the 1970s and 1980s. Meanwhile, the strong east–over twice as many than HIRHAM and almost five times as many for RACMO for the same time period (table 2). For the other independent measurement types (cores , snow pits and stake measurements) which are not grouped, the finer grid makes it less likely that multiple observations fall within a single cell. These factors increase the degrees of freedom in the fit, but also the potential for over-fitting and noise amplification, particularly in areas with sparse or uneven coverage. With fewer observations per cell, local discrepancies carry more weight, leading to greater variability in the fitted coefficients. Conversely, the coarser resolutions of HIRHAM and RACMO average more observational points within each grid cell, effectively smoothing localised anomalies and providing a more stable fit during optimisation. This is reflected by smaller mean deviations in their coefficients from the initial guess and lower uncertainties. west contrast in the south and high sensitivities in the central-east basin are consistent between both studies, suggesting these patterns have persisted over time.

The PCs coefficient adjustments may give insight into systematic temporal biases and potential links to large-scale climate drivers. Previous studies have linked leading EOF modes in Greenland snowfall with the North Atlantic Oscillation (NAO; Wong et al., 2015 , Greenland Blocking Index (GBI; Hanna et al., 2016) and sea ice cover (Kopec et al., 2016). Wong et al. (2015) show that the first and second EOFs are associated with NAO variability, Hanna et al. (2016) link the first EOF to GBI, and Kopec et al. (2016) correlate the second EOF with sea ice cover. In addition, Greenland surface temperatures, which influence atmospheric moisture and precipitation processes, have been shown to be impacted by El Niño events (Gan et al., 2023; Matsumura et al., 2021).

To explore whether these large-scale climate drivers can be linked with the EOF patterns

5.2 Limitations

The results presented in this study , and to understand what their PC adjustment coefficients may signify, we compute correlations between the first 10 PCs and the following indices: NAO, based on 500-hPa geopotential height anomalies from the NOAA/CPC (Barnston and Livezey, 1987); GBI, defined as the mean 500-hPa geopotential height over 60°–80°N, 280°–340°E (Hanna et al., 2016); Northern Hemisphere sea ice area from the NSIDC Sea Ice Index v3.0 (Fetterer, F.; Knowles K.; Meier W.; Savoie M.; ; and are subject to a number of methodological and observational limitations, which influence the magnitude, spatial structure and inter-model agreement in the Niño-3.4 index derived from ERSSTv5 SST anomalies over 5°N–5°S, 170°–120°W (Huang et al., 2017) . Annual correlations are presented in Fig. **??** for the full periods of HIRHAM (1960-2022) and RACMO (1980-2022) output, as well as the 1991-2022 overlap period with CARRA (1991-2022)final bias-adjusted accumulation, trend and sensitivity estimates.

Annual correlations of the first 10 PCs with the NAO, GBI, Northern Hemisphere sea ice area, and Niño3.4 indices. Correlations are shown for the full HIRHAM period (1960–2022), RACMO period (1980–2022), and the overlap period with CARRA (1991-2022).

PC2 shows consistent correlations with NAO and GBI of between 0.3 and 0.4 in magnitude across all models and time periods, aligning with relationships identified in previous studies. Weaker but persistent correlations with PC2 and sea ice are also seen, ranging from 0.1–0.2 in magnitude. While not previously emphasised in relation to PC2, moderate positive correlations with ENSO across all three models may suggest it has a secondary influence on this mode, possibly through its teleconnections with North Atlantic atmospheric conditions. As the 2nd PC shows correlations with these four climate indices of similar magnitude across models and the corresponding EOF maps Firstly, the EOFs are statistical constructs, which represent differing patterns of variability between models (Fig. A5) exhibit similar spatial patterns, this suggests that this mode represents similar pattern of variability across models, influenced by an interplay of these climatic circulation patterns.

The first PC only shows weak inter-annual correlations here. Wong et al. (2015), report correlations between NAO and precipitation at individual coastal stations, particularly in western Greenland, with the strongest relationships found in winter. However, they also note that the sign of the NAOand fitting period. In this study, we retain 10 EOFs, while higher-order EOFs account for an additional 8–precipitation correlation varies regionally, leading to opposing responses around the ice sheet margin. In contrast, our analysis is performed over the full ice sheet at an annual scale, potentially averaging out seasonally varying regional signals. This is consistent with the spatial structure of the first EOFs (Fig. A5), which are largely negative

across the accumulation zone in all three models, suggesting a dominant mode of coherent variability that does not capture regional contrasts.

As the PC adjustment coefficients are subject to the regularisation parameters, they deviate less than the EOF coefficients, with few notable exceptions: HIRHAM PC3, RACMO PC4, and CARRA PCs 4 14% of the variance. The higher order modes may represent physically meaningful variability rather than noise, and distinguishing between noise and signal in these higher modes is non-trivial. By construction, the EOF approach introduces a degree of spatial smoothing, meaning that highly localised differences accumulation captured in the observations may not be fully represented in the adjusted fields. Differences in EOF patterns and in how each mode is scaled by the observations may contribute to inter-model differences in the bias-adjusted results. A sensitivity test using up to 15 EOFs shows slight changes in spatial bias patterns and 6, which are adjusted mean accumulation values. Using 15 EOFs reduces the inter-model standard deviation in bias-adjusted mean accumulation over the ice sheet from 23 mm yr^{-1} (10 EOFs) to 0.5, 0.2, 0.3, and 2 respectively. A common feature among these PCs is their significant correlation with sea ice extent, which may suggest a misrepresentation of the influence of sea ice variability on accumulation. This is particularly relevant near the coast, where sea ice variability is known to strongly affect snowfall. The two-fold adjustment in CARRA 6th PC, which remains largely unchanged in HIRHAM and RACMO, may be linked to the opposing mean bias patterns seen in CARRA versus HIRHAM and RACMO along the north coast (Fig. 3) . A similar argument can be presented for CARRA PC2 and PC3 coefficients, which are adjusted down to 0.8 and 0.7, as a response to GBI.

While these examples do not prove causality, they may suggest potential links between specific modes of model bias and known large-scale atmospheric patterns. However, it is important to note that EOFs and PCs are statistical constructs whose ordering, spatial patterns and behaviour are not necessarily consistent across models. Therefore, while correlations with known climate indices can offer insight, physical interpretation of the adjustments should be viewed within the context that EOFs are not inherently structured to align themselves with physical drivers20 mm yr^{-1}, although both remain higher than the pre-adjustment standard deviation of 5 mm yr^{-1}. While this change is small relative to the overall level of inter-model agreement, it demonstrates that methodological choices in EOF truncation influence the adjustment outcome.

In practical terms, the EOF-based framework enables us to use the PCs derived from the accumulation zone to extrapolate EOFs for the full

Further sensitivity arises from the use of a common ice-sheet (eq. A5). The EOFs could be further extended beyond the spatial limits of observational coverage to infer bias-correcte precipitation/evaporation fields for the surrounding ocean, for example. In addition to spatial extrapolation, the PCs may also offer the potential for temporal extrapolation through their relations with correlated time series, enabling reconstructions of past accumulation patterns prior to availability of the RCM data. This could be implemented using a similar approach to that described in Box et al. (2013), which regress RACMO2 output between 1958-2010 with data from 86 ice cores to reconstruct net snow accumulation rates between 1600-2009. In our case, the mask rather than native model masks. Differences in glaciarised pixels near the margins of the mask may affect which spatial patterns are retained in the EOFs and therefore influence the final bias-adjusted PCs could be regressed against correlated climate drivers, temperature series, air pressure or ice-cores, for example. This approach could possibly be further extended to obtain future estimates, using projections of such correlated variables, though the reliability of future extrapolations

~~would strongly depend on the confidence in the projected regression variables, as well as the magnitude and stability of the underlying correlations~~fields and integrated accumulation estimates and total accumulation values in Gt yr^{-1}.

5.3 ~~Limitations~~

~~The reliability of the bias-corrected accumulation fields, associated temporal trends, temperature sensitivity estimates and any reconstructions based on temporal extrapolations ultimately hinge on one main factor – the qualityand confidence in~~

Despite the uncertainties associated with the method, comparison of the spatial bias patterns (Fig. 3, row 3) with point-wise biases (Fig. A3) lends confidence that the method captures the dominant bias structures present in the observations. While final mean accumulation values are sensitive to methodological choices, the bias-adjusted maps provide a robust representation of where models are biased according to observations.

Ultimately, however, our results are intrinsically dependent on the quality, representativeness and temporal coverage of the observational data used for bias adjustment. Though the ~~1.7~~ ~2 million data points in SUMup provide substantial statistical power compared to smaller-scale studies, observational uncertainties ~~ultimately~~ limit the accuracy of these final products. ~~Heavily dominated by annual and multi-annual means, the SUMup dataset lacks sufficient monthly observations in the accumulation zone matching the temporal resolution of the model data. This, in combination with the dating uncertainties inherent in radar, ice-cores and snow pit derived accumulation estimates, limits the reliability of bias-adjusted accumulation values on sub-annual scales. In addition, radar and ice coresestimates require density conversions~~Through detailed inspection of the SUMup database, we identified and removed a number of erroneous measurements, thereby improving the quality of the input dataset. However, despite extensive filtering and quality control, some erroneous or unrepresentative observations may remain. Radar-derived accumulation measurements, dominate the observational constraints, accounting for approximately 92–99% of the data used in the fitting. These measurements, as well as ice cores, rely on density assumptions, which vary between datasets and introduce further uncertainties. As a result, any systematic bias or methodological limitation inherent to radar surveys will have a pronounced influence on the adjusted fields. Experiments in which radar data were excluded lead to substantially larger apparent model biases and RMSE values. This likely reflects the drastic reduction in sample size and spatial coverage when radar data are omitted, increasing sensitivity to outliers. Continued efforts to improve the calibration of historical radar surveys and to identify outliers in point measurements will therefore be beneficial for any statistical analysis relying on SUMup.

To improve the accuracy of bias corrections, especially at sub-annual timescales, there is a pressing need for ~~more~~ additional high-resolution, ground-truth data such as direct snow-water-equivalent observations that are independent of density assumptions. High-temporal-resolution measurements from emerging technologies, such as those based on cosmic ray sensing (e.g. Howat et al., 2018), offer a promising means of providing continuous, density-independent accumulation data. Further work aimed at improving observational coverage and quality would enhance the robustness and reliability of future accumulation estimates.

6 Conclusions and Outlook

We have devised a novel statistical-semi-empirical framework to quantify and correct spatial and temporal biases in gridded model accumulation using any in-situ observational data. By providing spatially complete, bias-corrected accumulation fields, the method offers improved inputs for ice-sheet mass balance studies and other modelling efforts, such as the Ice Sheet Model Intercomparison Project (ISMIP).

Our method is applied here using observational SMB data from the SUMup dataset, to bias-adjust monthly accumulation output from ~~three~~ four high-resolution models over the Greenland Ice Sheet: HIRHAM5 (5.5 km, 1960-2022), MAR 3.14 (5 km, 1960-2022), RACMO2~~.41~~ .4p1 (11 km, 1980-2022), and CARRA reanalysis (2.5 km, 1991-2022). Relative to SUMup observations, we find point-wise initial mean biases of ~~-8.7~~-7.4% (HIRHAM), ~~+0.5% (~~-0.5% (MAR), 0.0% (RACMO) and +~~10.9~~10.1% (CARRA). ~~After~~ Following bias-correction, all models converge to near-zero mean bias (~~-0.1%to -0.2%~~±0.3%), with RMSE reduced by ~~8-18% and~~ 2-14% and modest improvements in correlation with observations ~~improving by~~ of ∼1~~–3~~%. The resulting bias-corrected mean annual accumulation over the ice sheet are estimated at ~~321~~ 469 ±24 mm yr^{-1} (HIRHAM~~, 1960-2022), 375~~), 412±12 mm yr^{-1} (MAR), 435±10 mm yr^{-1} (RACMO~~, 1980-2022) and 384~~) and 408±8 mm yr^{-1} (CARRA) for the 1991-2022 common period. Inter-1model agreement improves substantially in the accumulation zone, with standard deviation in mean accumulation estimates reducing by 68% for 1991-2022, indicating strong convergence where observational coverage is dense.

We compare the original and bias-adjusted accumulation maps to understand spatial bias patterns, identifying significant discrepancies between models. HIRHAM tends to underestimate across the ice-sheet, while CARRA largely overestimates. RACMO exhibits the lowest mean bias, ~~1991-2022) . By providing spatially complete, bias-corrected accumulation fields, the method offers improved inputs for ice-sheet mass balance studies and other modelling efforts, such as the Ice Sheet Model Intercomparison Project (ISMIP).~~ but exhibits strong spatial contrasts, with a high positive bias in the south and negative bias further north. All models show substantial bias in the south, consistent with previous studies, which have attributed substantial biases in the south to issues in resolving orographic precipitation over complex terrain (Langen et al., 2015; Box et al., 2013; Burgess et al., .

~~Given the calculated annual mean accumulation over GrIS is approximately 500 Gt yr^{-1} (Table **??**) and the total ice volume of GrIS is ∼2.5 million Gt (van den Broeke et al., 2016), a mean bias of 10% equates to 50 Gt yr^{-1}, or an annual error of ∼0.002% of total GrIS volume per year. Over a century long run, a 10% biasaccumulates to 5, 000 Gt, with the potential to alter sea-level rise projections by approximately 15 mm by 2100 (The IMBIE Team, 2020). Using the empirical relationship between SMB and temperature from AR5 (Intergovernmental Panel On Climate Change, 2014, Chapter 13 Supplementary Material), a 50 Gt yr^{-1} SMB deviation corresponds to an equivalent warming bias of ∼0.7°C. This is a substantial error, especially when viewed against critical thresholds for Greenland ice-sheet stability—such as the ∼1.6°C threshold identified by Robinson et al. (2012) , beyond which GrIS is expected to undergo irreversible long-term melt. Such SMB~~ Our results demonstrate that modest accumulation biases, if uncorrected, ~~could obscure or misrepresent the proximity to tipping points in climate~~ can translate

into temperature-equivalent errors large enough to obscure proximity to Greenland ice-sheet tipping points, highlighting the importance of bias-corrected accumulation reconstructions for both process understanding and long-term sea-level projections.

SMB Accumulation biases can also indirectly affect the ice dynamical response of ice-sheet models. Errors in SMB accumulation are absorbed into model calibration of ice dynamical parameters and thereby affect projections. As ice flow is driven by spatial gradients in SMBsurface mass balance, accurate spatial distribution pattern of accumulation are essential for simulating realistic ice flow, geometry, and evolution. Reliable projections are thus critically dependent not only on the total SMB, but on capturing its spatial variability across the ice sheet.

We compare the original and bias-adjusted accumulation maps to understand spatial bias patterns, identifying significant discrepancies between models. HIRHAM tends to underestimate across the accumulation zone, while CARRA largely overestimates across this domain. RACMO exhibits the lowest mean bias, but exhibits strong spatial contrasts, with a high positive bias in the south and negative bias further north. All three models show substantial bias in the south, consistent with previous studies, which have attributed substantial biases in the south to issues in resolving orographic precipitation over complex terrain (Langen et al., 2015; Box et al., 2013; Burgess et al., 2010).

These results underline the continued importance of bias-correcting model accumulation using in-situ observations to improve both the spatial fidelity and physical realism of SMB fields. However, the effectiveness of such corrections ultimately depends on the quality and resolution of the available observational data. The dominance of annual and multi-annual means and the scarcity of monthly-resolution data–ultimately limit the accuracy of the bias-adjusted accumulation at sub-annual timescales. To improve the accuracy of bias corrections, future efforts should prioritise expanding high-resolution in situ measurements, including direct snow-water-equivalent observations that are independent of density assumptions.

As our model is setupconfigured, new datasets can be readily integrated to further improve bias-correction. Here we have confined the bias-adjustment to the accumulation zone, enabling the use of consistent variables across the three models (precipitation minus evaporation/sublimation) to represent accumulation, accumulation rather than full SMB. This choice avoids reliance on uncertain snowpack or density modelling components, which are often inconsistent or unavailable. However, with sufficient observational constraints, the approach could be directly transferred to full SMB fields or other parametrisations and extended to the entire model domain, due to the lack of sufficient data to constrain runoff. Bias-adjusted accumulation fields may be combined with respective model runoff output to obtain partially bias-adjusted SMB estimates. Our framework can also be adapted to provide bias-corrected fields for other climate variables, as well as other regions such as the Antarctic ice-sheet.

Future work could explore temporal extrapolation of accumulation fields beyond the reanalysis period through leveraging relationships between EOF modes and large-scale climatic drivers. Preliminary analysis indicates that the PCs studied here correlate with climate indices such as the North Atlantic Oscillation, Greenland Blocking Index, and sea ice cover, consistent with previous studies. Modelling PC variability through these indices, combined with proxies such as air temperature, air pressure, ice cores, lake sediments and tree rings, could enable spatially-complete reconstructions of past accumulation patterns.

Code and data availability. Bias-adjusted accumulation fields are available at https://doi.org/10.5281/zenodo.18199332, along with minimal working code to reproduce results for HIRHAM, MAR, RACMO, and CARRA from their EOF decompositions using our processed SUMup dataset. The code can also be applied to other models to derive bias-adjusted fields from gridded accumulation output.

Appendix A: Appendix

A1 Details of EOF Analysis

This appendix provides supplementary details supporting the EOF analysis outlined in Section 3.1.

The model output, $\mathbf{X}(x,y,t)$, is first centred by removing the temporal mean, $\mathbf{M}(x,y)$, and the climatology, $\mathbf{C}(x,y,m)$. The centred data, $\mathbf{X}'(x,y,t)$, is rearranged into matrix form $\mathbf{X}'$, where each row (i) corresponds to a time index, and each column, (j), represents a grid cell, (x_j, y_j). The EOF computation is weighted by the square root of the fractional area of each cell.

To compute the EOFs, the covariance matrix, $\mathbf{\Psi}$, of the anomalies, $\mathbf{X}'$, is calculated as:

$$\mathbf{\Psi} = \frac{1}{N_t - 1} \mathbf{X'}^{\mathrm{T}} \mathbf{X}'. \tag{A1}$$

The EOFs are derived by solving the eigenvalue problem, $\mathbf{\Psi E} = \mathbf{E\Lambda}$, where the eigenvectors, $\mathbf{E}$, are the EOFs and $\mathbf{\Lambda}$ are the eigenvalues arranged in a diagonal matrix. The EOFs are ordered by their corresponding eigenvalues such that the first EOF captures the greatest amount of variance in the data. The Principle Components (PCs) are obtained by projecting the centred data onto the EOFs:

$$\mathbf{PC} = \mathbf{E}^T \mathbf{X}', \tag{A2}$$

where each column of $\mathbf{PC}$ represents the time series of the corresponding mode, expressing how much each mode contributes to the variability through time.

The reconstructed accumulation, $\mathbf{RCM}(x,y,t)$ can thereby be expressed as:

$$\mathbf{RCM}(x,y,t) = \mathbf{M}(x,y,t) + \mathbf{C}(x,y,m) + \sum_{i=1}^{N} \mathbf{PC}_i(t) \cdot \mathbf{EOF}_i(x,y). \tag{A3}$$

It is common to de-trend data prior to EOF decomposition to prevent a long-term linear or low-frequency signal from dominating the leading modes. However, as accumulation trends vary strongly by region and no clear trend was seen to dominate the PCs, there was no advantage in removing a single linear trend. By not de-trending the data, the resulting modes can reflect both the variability and long-term evolution, allowing the bias-adjustment to account for trends in a way that appropriately scales with the rest of the data.

As the common mask introduces some mismatch in glaciarised pixels, SMB components are unavailable in some marginal grid cells. Thus, we calculate extrapolated EOFs, $\mathbf{EOF}_{\mathrm{ext}}$, to fill in these pixels. Within common ice-sheet mask, the anomalies, $\mathbf{X}'_{full}(x,y,t)$ can be expressed as:

$$\mathbf{X}'_{full}(x,y,t) = \sum_{i=1}^{N_t} \mathbf{PC}_i(t) \cdot \mathbf{EOF}_{ext,i}(x,y). \tag{A4}$$

Eq. A4 is projected onto $\mathbf{PC}_i(t)$ and rearranged to obtain an expression for $\mathbf{EOF}_{ext,i}(x,y)$:

$$\mathbf{EOF}_{\mathrm{ext},i}(x,y) = \frac{\mathbf{PC}_i(t) \cdot \mathbf{X'}_{ext}(x,y,t)}{\sum_{i=1}^{N_t} \mathbf{PC}_i^2}. \tag{A5}$$

A2 Appendix Figures

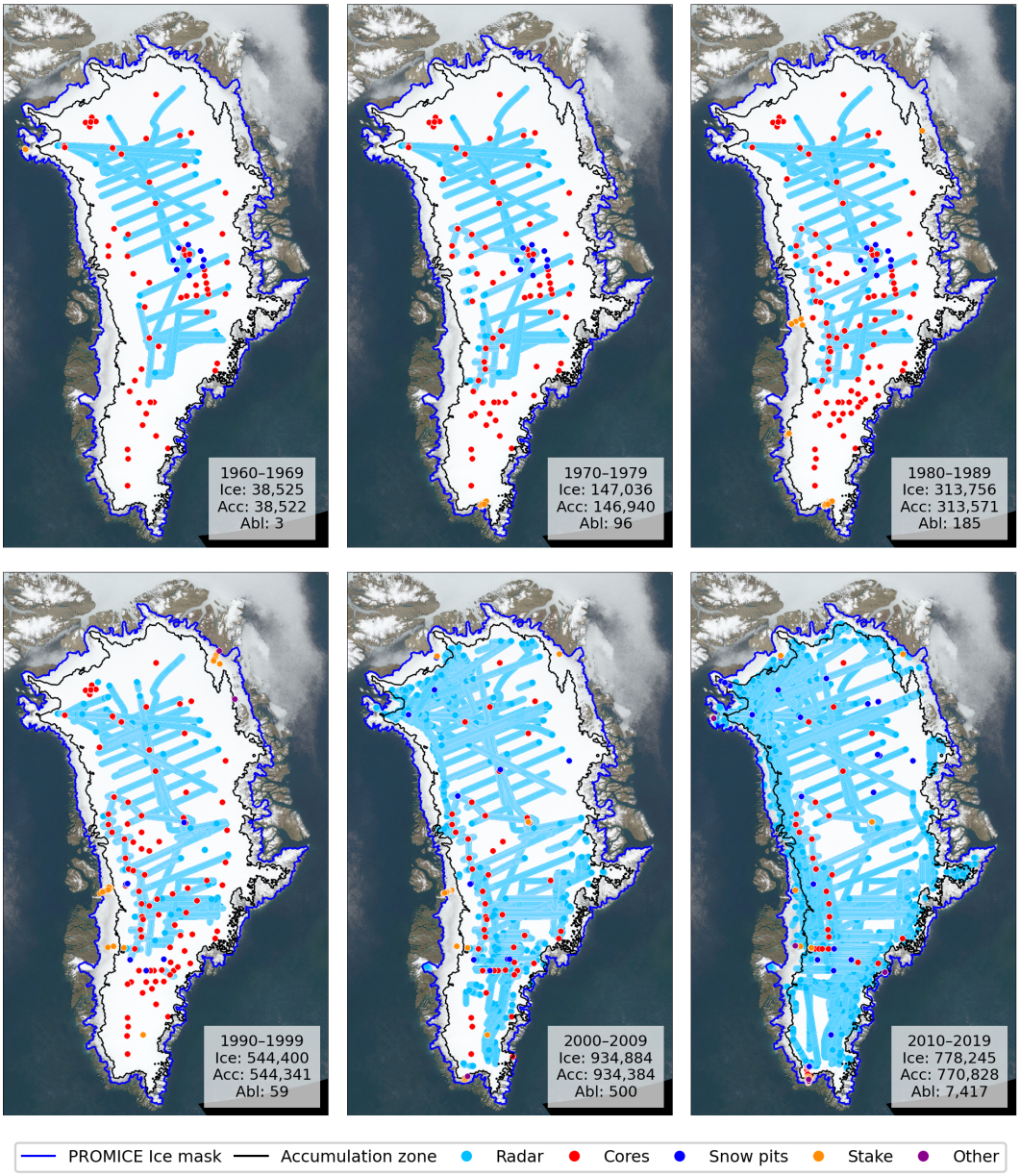

Figure A1. ~~Mean maps of model accumulation~~ SUMup data distribution by decade, illustrated by measurement type. The method type 'other' includes measurements from mass balance profile and ~~bias over the 1991–2022 overlap period~~SnowFox sensors. Values ~~stated in the lower corners~~ for 'Ice', 'Acc' and 'Abl' indicate the ~~spatial mean over~~ total number of data points for the ice-sheet, accumulation ~~zone (left)~~ and ~~ice sheet (right). First row: original mean accumulation~~ ablation zones before ~~adjustment~~radar grouping.~~Second row: mean bias-corrected accumulation. Third row: mean bias in mm yr^{-1}. Fourth row: mean percentage bias.~~

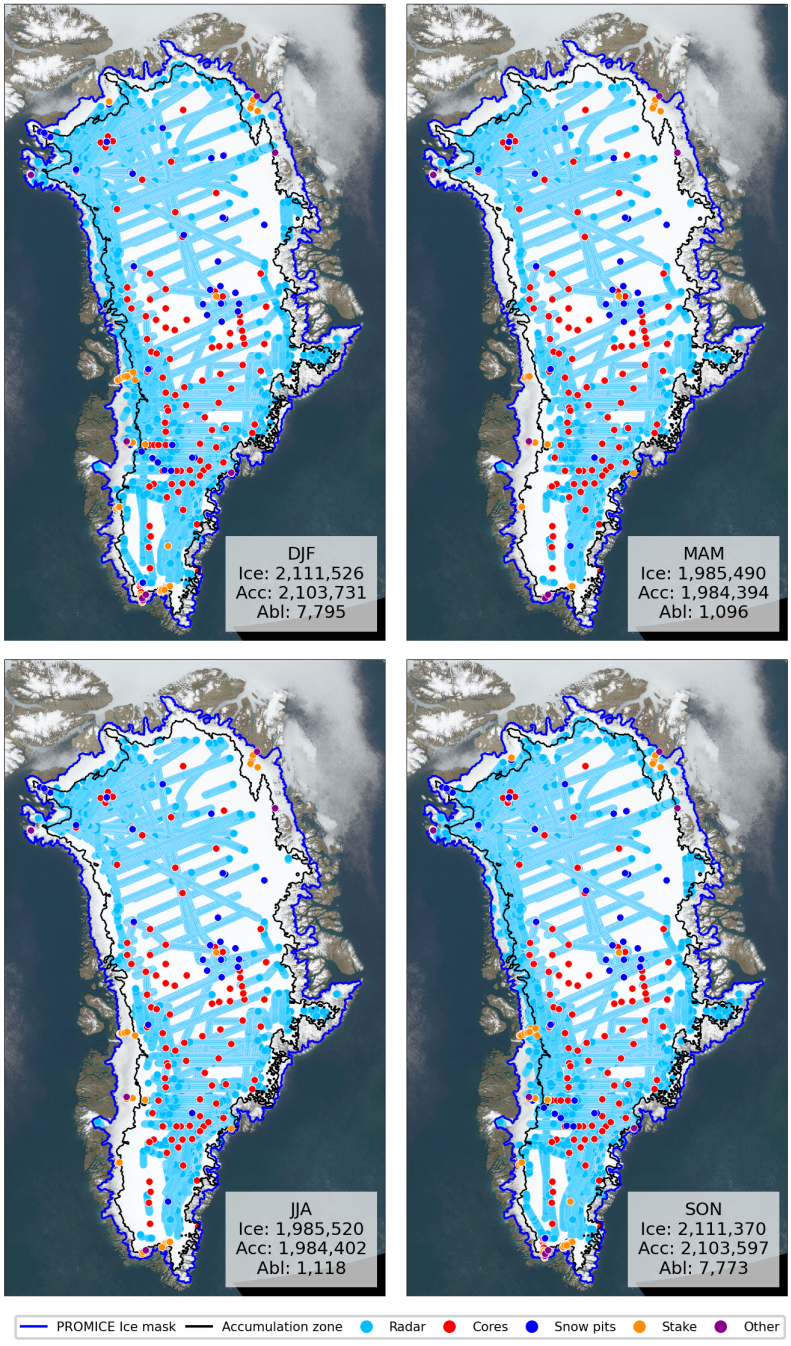

Figure A2. SUMup data distribution by ~~decade~~season (1960-2022), ~~plotted over HIRHAM decadal bias with mean~~illustrated by measurement type. The method type 'other' includes measurements from mass balance profile and SnowFox sensors. Values for 'Ice', ~~minimum~~ 'Acc' and ~~maximum bias values printed~~ 'Abl' indicate the total number of data points for ~~each decade~~the ice-sheet, accumulation and ablation zones before radar grouping.

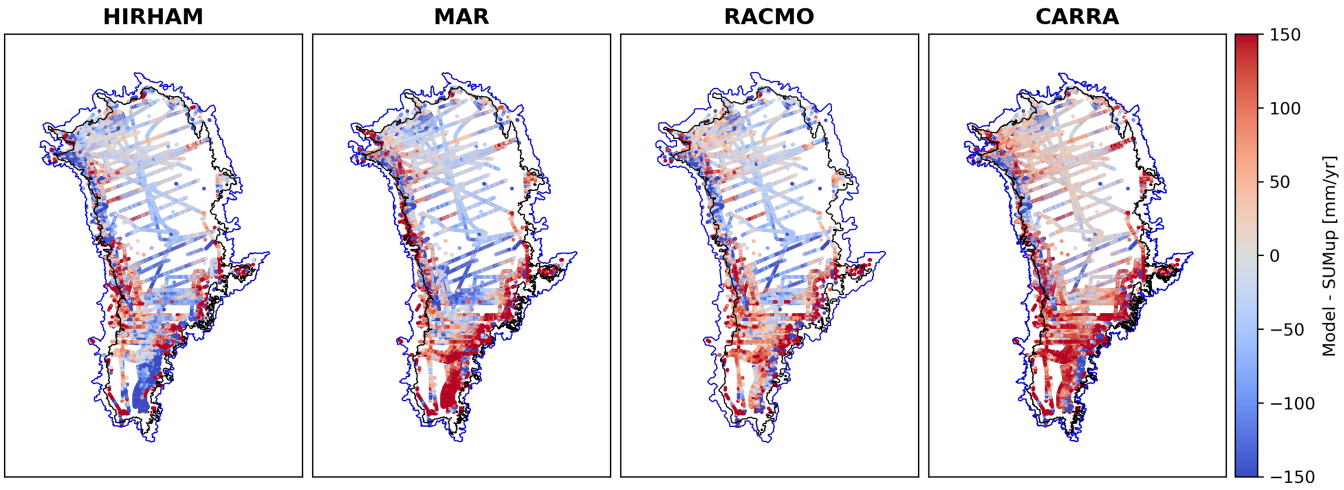

Figure A3. ~~First three EOF patterns for HIRHAM~~ SUMup point-wise bias (~~1960-2022), RACMO (1980-2022) and CARRA (~~1991-2022)~~over~~ . The blue contour indicates the boundary of the PROMICE ice-sheet mask and the black contour shows the boundary of the accumulation zone.

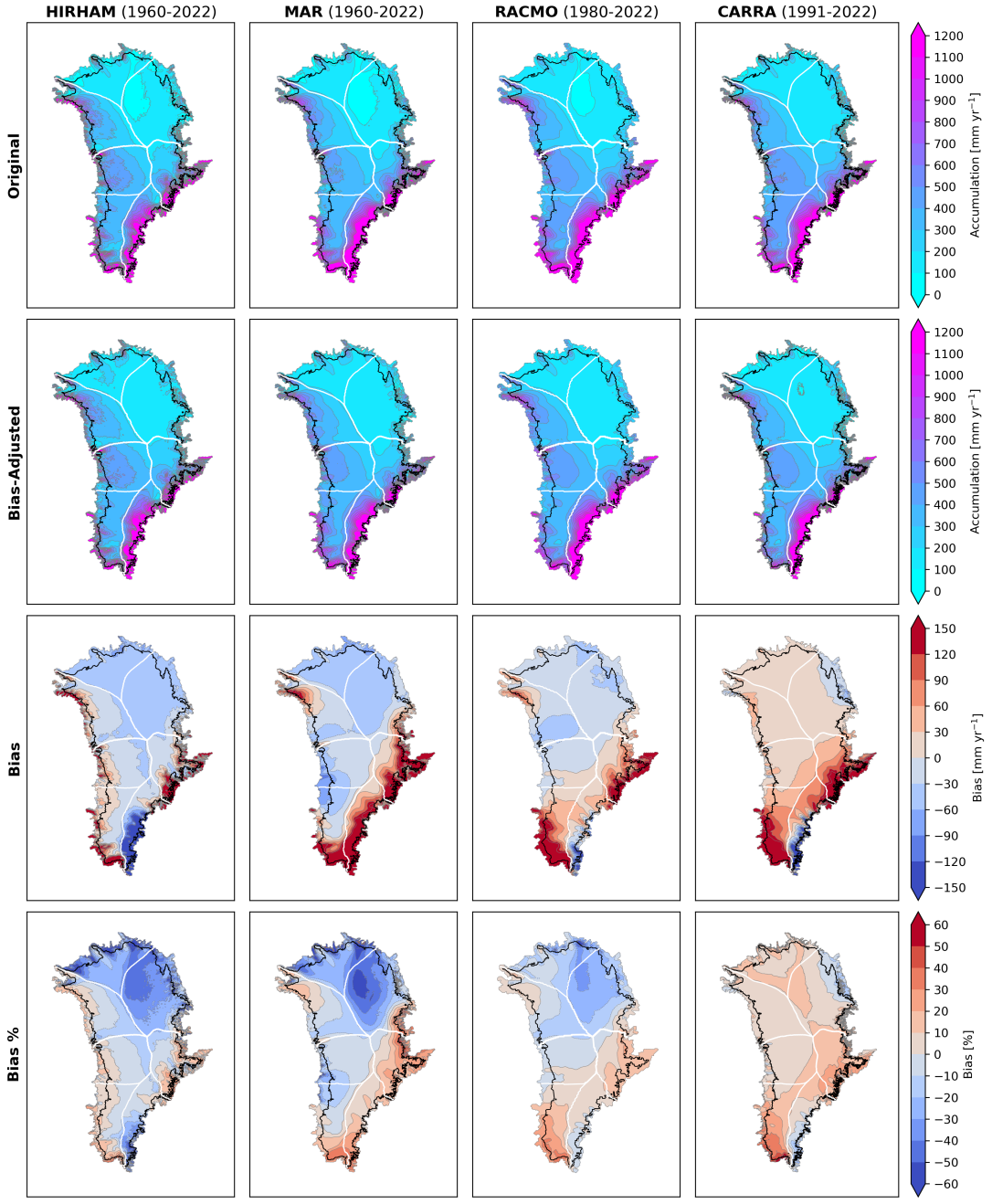

Figure A4. Mean maps of model accumulation and bias for the full model periods, HIRHAM (1960-2022), MAR (1960-2022), RACMO (1980-2022) and CARRA (1991-2022). The black line indicates the boundary of the accumulation zone. First row: original mean accumulation before adjustment. Second row: mean bias-corrected accumulation. Third row: mean bias in mm yr^{-1}. Fourth row: mean relative bias. PROMICE drainage basin boundaries are indicated in white.

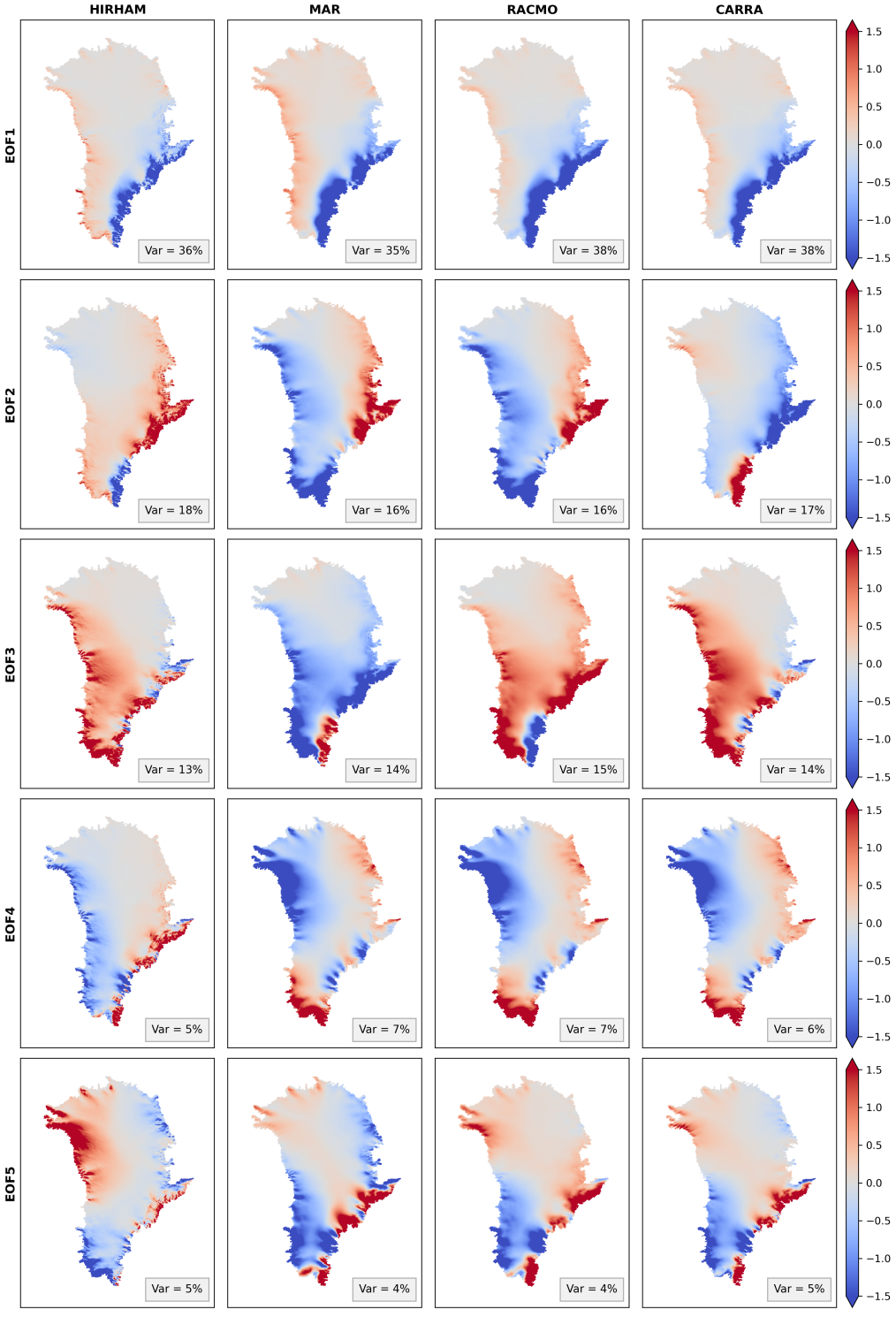

Figure A5. First five EOF patterns for HIRHAM, MAR, RACMO and CARRA over 1991-2022.

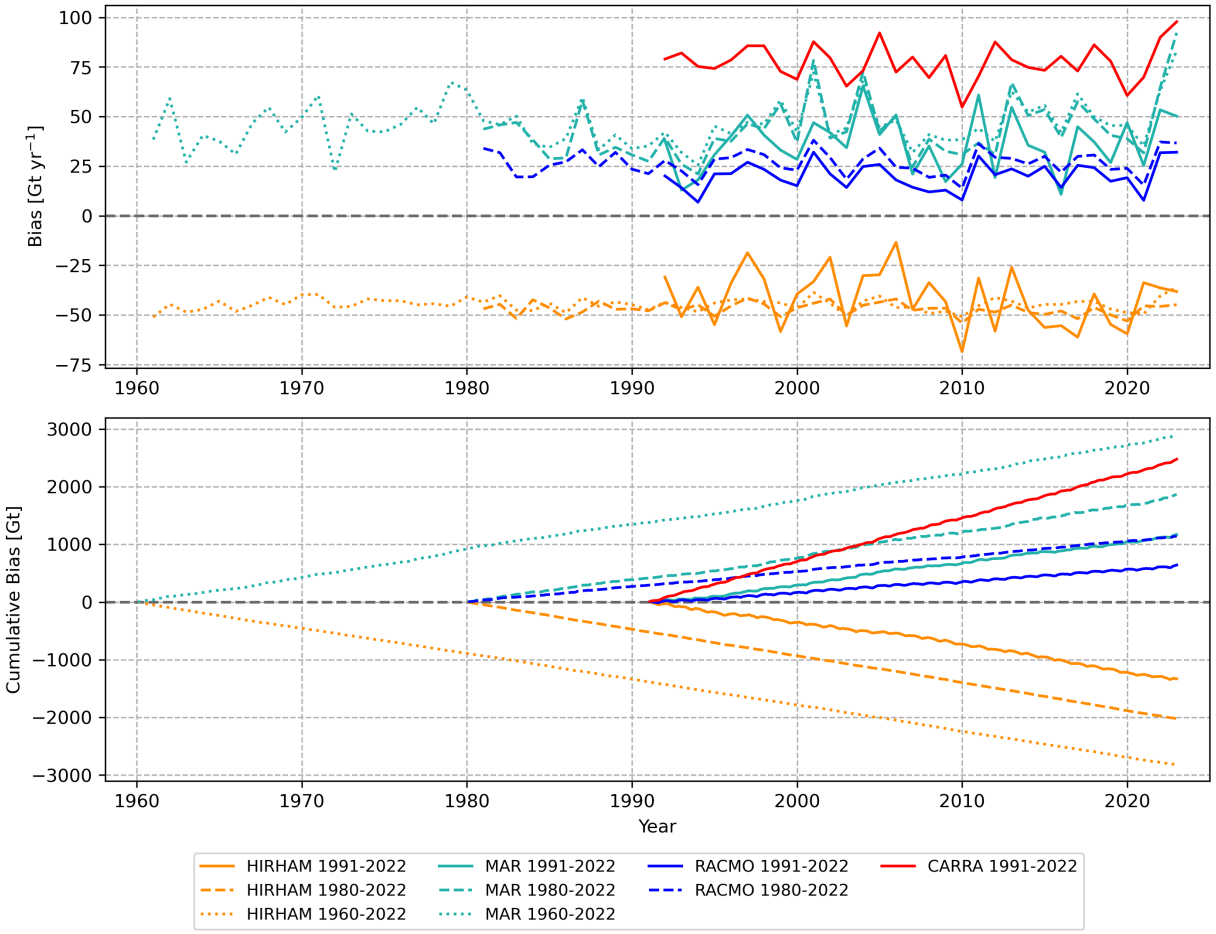

Figure A6. ~~Mean~~ Spatially integrated annual bias [Gt yr^{-1}] for ~~HIRHAM~~each model over the 1960-2022, ~~RACMO~~ 1980-2022 and ~~CARRA plotted against time with temporal trends~~ 1991-2022 fitting periods, shown by year (upper) and ~~standard deviations~~as the cumulative sum (lower), indicating the net effect of the adjustment through time.

~~Evaluation of model performance against observations from 6 ice core sites before and after bias-adjustment.~~

		Ice Sheet			Accumulation Zone			Ablation Zone		
Period	**Model**	**Acc**	**Acc_{adj}**	**Bias**	**Acc**	**Acc_{adj}**	**Bias**	**Acc**	**Acc_{adj}**	**Bias**
		~~Gt yr^{-1}~~	[Gt yr^{-1}]	~~Gt yr^{-1}~~	[Gt yr^{-1}]	~~Gt yr^{-1}~~	[Gt yr^{-1}]			
1960–2022	~~Gt yr^{-1}~~HIRHAM	~~Gt yr^{-1}~~782	~~Gt yr^{-1}~~827 ± 48	−45	514	555 ± 26	−42	269	272 ± 23	−3
	MAR	754	708 ± 21	+46	556	530 ± 13	+26	199	178 ± 9	+21
1980–2022	HIRHAM	795	842 ± 48	−47	522	564 ± 23	−43	274	278 ± 25	−4
	MAR	765	722 ± 19	+43	562	538 ± 12	+24	203	184 ± 8	+19
	RACMO	809	783 ± 23	+27	547	537 ± 13	+10	262	246 ± 11	+17
1991–2022	HIRHAM	805	846 ± 43	−42	528	571 ± 20	−44	277	275 ± 23	+2
	MAR	779	742 ± 21	+37	572	550 ± 13	+21	207	192 ± 9	+15
	RACMO	820	800 ± 19	+20	555	549 ± 10	+6	265	251 ± 9	+14
	CARRA	808	730 ± 14	+77	608	551 ± 8	+56	200	179 ± 6	+21

Table A1. Spatially integrated mean annual accumulation over the ice sheet, accumulation zone, and ablation zone expressed in Gt yr^{-1} for original (Acc) and bias-adjusted (Acc_{adj}) accumulation. Net bias is defined as Acc − Acc_{adj}. Uncertainties for Acc_{adj} are obtained by eq. 10.

Period	**Model**	**N**	**NE**	**CE**	**SE**	**SW**	**CW**	**NW**
1960–2022	HIRHAM	~~259~~ 0.9 / 0.8	~~282~~ 7.7 / 7.8	~~−23~~ 25.8 / 26.0	~~474~~ 17.3 / 18.0	~~503~~ 5.4 / 5.5	~~−29~~ 2.8 / 2.7	2.1 / 1.6
	MAR	0.4 / 1.0	8.4 / 6.6	26.0 / 23.5	18.1 / 21.2	5.0 / 2.1	3.3 / 2.5	2.9 / 3.3
1980–2022	HIRHAM	~~263~~ -3.8 / -3.9	~~287~~ 7.0 / 7.0	~~−24~~ 25.7 / 26.4	~~481~~ 47.4 / 48.2	~~511~~ -1.5 / -1.3	~~−29~~ -0.6 / -0.5	8.0 / 8.0
	MAR	-2.2 / -2.1	10.5 / 9.2	30.4 / 33.9	56.2 / 54.4	3.9 / -4.3	1.6 / -2.4	10.5 / 6.4
	RACMO	~~301~~ -2.4 / -3.1	~~300~~ 10.5 / 7.8	~~+1~~ 22.5 / 23.1	~~560~~ 45.2 / 46.1	~~536~~ 0.1 / 1.3	~~+24~~ 1.7 / 1.2	7.7 / 5.4
1991–2022	HIRHAM	~~266~~ -5.6 / -5.8	~~288~~ 7.8 / 7.8	~~−22~~ 30.5 / 34.9	~~486~~ 57.7 / 65.7	~~514~~ -14.3 / -11.4	~~−27~~ -4.2 / -1.9	4.5 / 5.4
	MAR	-3.1 / -4.2	14.1 / 14.6	34.4 / 33.5	66.0 / 64.2	-7.8 / -5.7	-1.6 / -3.0	5.2 / 0.5
	RACMO	~~305~~ -3.7 / -5.2	~~302~~ 9.3 / 10.1	~~+3~~ 24.6 / 24.9	~~567~~ 52.4 / 53.1	~~540~~ -13.4 / -10.7	~~+27~~ -2.9 / -4.4	5.7 / 0.1
	CARRA	~~315~~ -2.5 / -6.1	~~285~~ 10.5 / 10.2	~~+30~~ 14.9 / 21.5	~~562~~ 34.2 / 36.1	~~503~~ -15.5 / -13.0	~~+59~~ -8.0 / -6.1	6.0 / -0.8

Table A2. ~~Mean annual~~ Basin-wise accumulation ~~over the accumulation zone~~ trends (mm yr^{-1} decade^{-1}) before (left) and ~~ice sheet~~ after bias adjustment (right) for each model and evaluation period. Values for each basin are shown before (left) and after ~~bias-adjustment, including absolute~~ (right) bias ~~, in Gt yr^{-1}~~ adjustment.

Period	Model	N	NE	CE	SE	SW	CW	NW
1960–2022	HIRHAM	2.1 / 1.5	20.6 / 15.9	13.6 / 15.2	5.9 / 5.1	2.3 / 2.3	2.8 / 2.5	2.8 / 2.6
	MAR	1.4 / 2.3	21.8 / 15.3	14.4 / 18.1	6.8 / 9.3	1.7 / -1.3	2.6 / 1.7	2.9 / 3.4
1980–2022	HIRHAM	-5.5 / -4.3	12.6 / 10.8	9.0 / 10.3	7.4 / 5.6	-2.8 / -2.8	0.6 / 0.4	7.0 / 6.9
	MAR	-1.6 / -1.2	20.7 / 17.5	12.4 / 20.6	12.2 / 14.3	-0.5 / -4.7	1.7 / -1.4	9.8 / 5.7
	RACMO	-3.6 / -3.9	15.0 / 13.3	8.9 / 10.6	9.0 / 9.2	-0.8 / -0.6	2.4 / 1.9	6.1 / 4.3
1991–2022	HIRHAM	-9.3 / -7.6	7.8 / 7.2	8.5 / 11.9	9.0 / 8.1	-12.5 / -10.8	-2.2 / -1.2	4.1 / 4.7
	MAR	-2.6 / -3.4	20.2 / 22.3	11.6 / 16.5	14.4 / 15.8	-9.5 / -10.2	-1.5 / -4.3	4.9 / 0.0
	RACMO	-6.5 / -7.9	12.0 / 11.5	7.4 / 8.8	11.0 / 10.8	-10.0 / -11.4	-1.3 / -2.5	3.8 / 0.2
	CARRA	-4.1 / -9.4	9.9 / 14.2	1.3 / 8.1	5.4 / 5.4	-11.4 / -13.2	-4.6 / -4.2	5.1 / -0.3

Table A3. Basin-wise spatial mean accumulation sensitivity to temperature (% K^{-1}) for each model and evaluation period. Values for each basin are shown before (left) and after (right) bias adjustment.

Author contributions. JLC and AG designed the bias-adjustment method. BV provided the figure of model evaluation against the 6 individual ice core sites. JLC wrote the initial manuscript, prepared and filtered the SUMup dataset, and created the remaining figures and tables. All authors participated in the data interpretation and commented on the paper.

Competing interests. No competing interests are present.

Acknowledgements. JLC, AG and CH received funding from the Novo Nordisk Foundation (NNF Challenge, PRECISE – Prediction of Ice Sheets on Earth, grant no. NNF23OC0081251). CH received funding from the European Union (Horizon Europe, ICELINK, grant no. 101184621). The authors thank Martin Olesen (Danish Meteorological Institute) for providing HIRHAM5 data (1960-2022), Kristiina Verro (Danish Meteorological Institute) for providing RACMO data (1980-2022), and Clément Cherblanc for valuable feedback on the manuscript. The SUMup 2024 dataset was supported by PROMICE.

References

Bales, R. C., Guo, Q., Shen, D., McConnell, J. R., Du, G., Burkhart, J. F., Spikes, V. B., Hanna, E., and Cappelen, J.: Annual accumulation for Greenland updated using ice core data developed during 2000–2006 and analysis of daily coastal meteorological data, Journal of Geophysical Research: Atmospheres, 114, https://doi.org/10.1029/2008JD011208, 2009.

Banta, J. R. and McConnell, J. R.: Annual accumulation over recent centuries at four sites in central Greenland, Journal of Geophysical Research: Atmospheres, 112, https://doi.org/10.1029/2006JD007887, 2007.

Barnston, A. G. and Livezey, R. E.: Classification, Seasonality and Persistence of Low-Frequency Atmospheric Circulation Patterns, https://journals.ametsoc.org/view/journals/mwre/115/6/1520-0493_1987_115_1083_csapol_2_0_co_2.xml, section: Monthly Weather Review, 1987.

Batrak, Y., Cheng, B., and Kallio-Myers, V.: Sea ice cover in the Copernicus Arctic Regional Reanalysis, The Cryosphere, 18, 1157–1183, https://doi.org/10.5194/tc-18-1157-2024, publisher: Copernicus GmbH, 2024.

Bengtsson, L., Andrae, U., Aspelien, T., Batrak, Y., Calvo, J., Rooy, W. d., Gleeson, E., Hansen-Sass, B., Homleid, M., Hortal, M., Ivarsson, K.-I., Lenderink, G., Niemelä, S., Nielsen, K. P., Onvlee, J., Rontu, L., Samuelsson, P., Muñoz, D. S., Subias, A., Tijm, S., Toll, V., Yang, X., and Køltzow, M. : The HARMONIE–AROME Model Configuration in the ALADIN–HIRLAM NWP System, https://doi.org/10.1175/MWR-D-16-0417.1, section: Monthly Weather Review, 2017.

Bennartz, R., Fell, F., Pettersen, C., Shupe, M. D., and Schuettemeyer, D.: Spatial and temporal variability of snowfall over Greenland from CloudSat observations, Atmospheric Chemistry and Physics, 19, 8101–8121, https://doi.org/10.5194/acp-19-8101-2019, 2019.

Bingham, R. G., Bodart, J. A., Cavitte, M. G. P., Chung, A., Sanderson, R. J., Sutter, J. C. R., Eisen, O., Karlsson, N. B., MacGregor, J. A., Ross, N., Young, D. A., Ashmore, D. W., Born, A., Chu, W., Cui, X., Drews, R., Franke, S., Goel, V., Goodge, J. W., Henry, A. C. J., Hermant, A., Hills, B. H., Holschuh, N., Koutnik, M. R., Leysinger Vieli, G. J.-M. C., MacKie, E. J., Mantelli, E., Martín, C., Ng, F. S. L., Oraschewski, F. M., Napoleoni, F., Parrenin, F., Popov, S. V., Rieckh, T., Schlegel, R., Schroeder, D. M., Siegert, M. J., Tang, X., Teisberg, T. O., Winter, K., Yan, S., Davis, H., Dow, C. F., Fudge, T. J., Jordan, T. A., Kulessa, B., Matsuoka, K., Nyqvist, C. J., Rahnemoonfar, M., Siegfried, M. R., Singh, S., Višnjević, V., Zamora, R., and Zuhr, A.: Review article: AntArchitecture – building an age–depth model from Antarctica's radiostratigraphy to explore ice-sheet evolution, The Cryosphere, 19, 4611–4655, https://doi.org/10.5194/tc-19-4611-2025, publisher: Copernicus GmbH, 2025.

Bochow, N., Poltronieri, A., and Boers, N.: Projections of precipitation and temperatures in Greenland and the impact of spatially uniform anomalies on the evolution of the ice sheet, The Cryosphere, 18, 5825–5863, https://doi.org/10.5194/tc-18-5825-2024, 2024.

Bolzan, J. F. and Strobel, M.: Accumulation-rate variations around Summit, Greenland, Journal of Glaciology, 40, 56–66, https://doi.org/10.3189/s0022143000003798, 1994.

Bolzan, J. F. and Strobel, M.: Oxygen isotope data from snowpit at GISP2 Site 13, PANGAEA, https://doi.org/10.1594/PANGAEA.55510, 1999a.

Bolzan, J. F. and Strobel, M.: Oxygen isotope data from snowpit at GISP2 Site 15, PANGAEA, https://doi.org/10.1594/PANGAEA.55511, 1999b.

Bolzan, J. F. and Strobel, M.: Oxygen isotope data from snowpit at GISP2 Site 31, PANGAEA, https://doi.org/10.1594/PANGAEA.55512, 1999c.

Bolzan, J. F. and Strobel, M.: Oxygen isotope data from snowpit at GISP2 Site 37, PANGAEA, https://doi.org/10.1594/PANGAEA.55513, 1999d.

Bolzan, J. F. and Strobel, M.: Oxygen isotope data from snowpit at GISP2 Site 51, PANGAEA, https://doi.org/10.1594/PANGAEA.55514, 1999e.

Bolzan, J. F. and Strobel, M.: Oxygen isotope data from snowpit at GISP2 Site 57, PANGAEA, https://doi.org/10.1594/PANGAEA.55515, 1999f.

Bolzan, J. F. and Strobel, M.: Oxygen isotope data from snowpit at GISP2 Site 73, PANGAEA, https://doi.org/10.1594/PANGAEA.55516, 1999g.

Bolzan, J. F. and Strobel, M.: Oxygen isotope data from snowpit at GISP2 Site 44, PANGAEA, https://doi.org/10.1594/PANGAEA.59995, 2001a.

Bolzan, J. F. and Strobel, M.: Oxygen isotope data from snowpit at GISP2 Site 571, PANGAEA, https://doi.org/10.1594/PANGAEA.59996, 2001b.

Box, J. E.: Greenland ice sheet surface mass-balance variability: 1991–2003, Annals of Glaciology, 42, 90–94, https://doi.org/10.3189/172756405781812772, 2005.

Box, J. E., Bromwich, D. H., and Bai, L.-S.: Greenland ice sheet surface mass balance 1991–2000: Application of Polar MM5 mesoscale model and in situ data, Journal of Geophysical Research: Atmospheres, 109, https://doi.org/10.1029/2003JD004451, 2004.

Box, J. E., Bromwich, D. H., Veenhuis, B. A., Bai, L.-S., Stroeve, J. C., Rogers, J. C., Steffen, K., Haran, T., and Wang, S.-H.: Greenland Ice Sheet Surface Mass Balance Variability (1988–2004) from Calibrated Polar MM5 Output, https://doi.org/10.1175/JCLI3738.1, 2006.

Box, J. E., Yang, L., Bromwich, D. H., and Bai, L.-S.: Greenland Ice Sheet Surface Air Temperature Variability: 1840–2007, https://doi.org/10.1175/2009JCLI2816.1, 2009.

Box, J. E., Cressie, N., Bromwich, D. H., Jung, J.-H., Broeke, M. v. d., Angelen, J. H. v., Forster, R. R., Miège, C., Mosley-Thompson, E., Vinther, B., and McConnell, J. R.: Greenland Ice Sheet Mass Balance Reconstruction. Part I: Net Snow Accumulation (1600–2009), https://doi.org/10.1175/JCLI-D-12-00373.1, 2013.

Box, J. E., Wehrlé, A., Van As, D., Fausto, R. S., Kjeldsen, K. K., Dachauer, A., Ahlstrøm, A. P., and Picard, G.: Greenland Ice Sheet Rainfall, Heat and Albedo Feedback Impacts From the Mid-August 2021 Atmospheric River, Geophysical Research Letters, 49, e2021GL097 356, https://doi.org/10.1029/2021GL097356, 2022.

Box, J. E., Nielsen, K. P., Yang, X., Niwano, M., Wehrlé, A., van As, D., Fettweis, X., Køltzow, M. A. , Palmason, B., Fausto, R. S., van den Broeke, M. R., Huai, B., Ahlstrøm, A. P., Langley, K., Dachauer, A., and Noël, B.: Greenland ice sheet rainfall climatology, extremes and atmospheric river rapids, Meteorological Applications, 30, e2134, https://doi.org/10.1002/met.2134, 2023.

Brun, E., David, P., Sudul, M., and Brunot, G.: A numerical model to simulate snow-cover stratigraphy for operational avalanche forecasting, Journal of Glaciology, 38, 13–22, https://doi.org/10.3189/S0022143000009552, 1992.

Buchardt, S. L., Clausen, H. B., Vinther, B. M., and Dahl-Jensen, D.: Investigating the past and recent δ^{18}O-accumulation relationship seen in Greenland ice cores, Climate of the Past, 8, 2053–2059, https://doi.org/10.5194/cp-8-2053-2012, 2012.

Burgess, E. W., Forster, R. R., Box, J. E., Mosley-Thompson, E., Bromwich, D. H., Bales, R. C., and Smith, L. C.: A spatially calibrated model of annual accumulation rate on the Greenland Ice Sheet (1958–2007), Journal of Geophysical Research: Earth Surface, 115, https://doi.org/10.1029/2009JF001293, 2010.

Calanca, P., Gilgen, H., Ekholm, S., and Ohmura, A.: Gridded temperature and accumulation distributions for Greenland for use in cryospheric models, Annals of Glaciology, 31, 118–120, https://doi.org/10.3189/172756400781820345, 2000.

Chandler, D. M., Alcock, J. D., Wadham, J. L., Mackie, S. L., and Telling, J.: Seasonal changes of ice surface characteristics and productivity in the ablation zone of the Greenland Ice Sheet, The Cryosphere, 9, 487–504, https://doi.org/10.5194/tc-9-487-2015, 2015.

Chandler, D. M., Wadham, J. L., Nienow, P. W., Doyle, S. H., Tedstone, A. J., Telling, J., Hawkings, J., Alcock, J. D., Linhoff, B., and Hubbard, A.: Rapid development and persistence of efficient subglacial drainage under 900 m-thick ice in Greenland, Earth and Planetary Science Letters, 566, 116 982, https://doi.org/10.1016/j.epsl.2021.116982, 2021.

Chen, X., Zhang, X., Church, J. A., Watson, C. S., King, M. A., Monselesan, D., Legresy, B., and Harig, C.: The increasing rate of global mean sea-level rise during 1993–2014, Nature Climate Change, 7, 492–495, https://doi.org/10.1038/nclimate3325, publisher: Nature Publishing Group, 2017.

Clapeyron, : Mémoire sur la puissance motrice de la chaleur, J. Gabay, Paris, [reproduction en fac-similé] edn., ISBN 978-2-87647-283-9, http://catalogue.bnf.fr/ark:/12148/cb40936143n, 2006.

Clausen, H., Gundestrup, N., Johnsen, S., Bindschadler, R., and Zwally, J.: Glaciological Investigations in the Crête Area, Central Greenland: A Search for a new Deep-Drilling Site, Annals of Glaciology, 10, 10–15, https://doi.org/10.3189/s0260305500004080, 1988.

Clausius, R.: Ueber die bewegende Kraft der Wärme und die Gesetze, welche sich daraus für die Wärmelehre selbst ableiten lassen, Annalen der Physik, 155, 368–397, https://doi.org/10.1002/andp.18501550306, 1850.

Cogley, J. G.: Greenland accumulation: An error model, Journal of Geophysical Research: Atmospheres, 109, https://doi.org/10.1029/2003JD004449, 2004.

Copernicus Climate Change Service: Arctic regional reanalysis on single levels from 1991 to present, https://doi.org/10.24381/CDS.713858F6, 2021a.

Copernicus Climate Change Service: CARRA User Guide, Tech. rep., European Centre for Medium-Range Weather Forecasts, https://climate.copernicus.eu/copernicus-arctic-regional-reanalysis-carra, 2021b.

Dawson, A.: eofs: A Library for EOF Analysis of Meteorological, Oceanographic, and Climate Data, Journal of Open Research Software, 4, https://doi.org/10.5334/jors.122, 2016.

Delhasse, A., Kittel, C., Amory, C., Hofer, S., van As, D., S. Fausto, R., and Fettweis, X.: Brief communication: Evaluation of the near-surface climate in ERA5 over the Greenland Ice Sheet, The Cryosphere, 14, 957–965, https://doi.org/10.5194/tc-14-957-2020, publisher: Copernicus GmbH, 2020.

Dibb, J. E. and Fahnestock, M.: Snow accumulation, surface height change, and firn densification at Summit, Greenland: Insights from 2 years of in situ observation, Journal of Geophysical Research: Atmospheres, 109, https://doi.org/10.1029/2003jd004300, 2004.

DMI, Christensen, B., and Christensen, H.: The HIRHAM Regional Climate Model. Version 5 (beta), Technical Report, 2017.

Ettema, J., van den Broeke, M. R., van Meijgaard, E., van de Berg, W. J., Bamber, J. L., Box, J. E., and Bales, R. C.: Higher surface mass balance of the Greenland ice sheet revealed by high-resolution climate modeling, Geophysical Research Letters, 36, https://doi.org/10.1029/2009GL038110, 2009.

Ettema, J., van den Broeke, M. R., van Meijgaard, E., van de Berg, W. J., Box, J. E., and Steffen, K.: Climate of the Greenland ice sheet using a high-resolution climate model – Part 1: Evaluation, The Cryosphere, 4, 511–527, https://doi.org/10.5194/tc-4-511-2010, publisher: Copernicus GmbH, 2010.

Fausto, R. S.: Snow-water equivalent of snowpacks, GEUS Dataverse, N/A, N/A, https://doi.org/10.22008/FK2/B5KVJV, 2021.

Fausto, R. S., Andersen, S. B., Ahlstrøm, A. P., van As, D., Box, J. E., Binder, D., Citterio, M., Colgan, W., Haubner, K., Hansen, K., Karlsson, N. B., Mankoff, K. D., Pedersen, A. , Solgaard, A., and Vandecrux, B.: Greenland ice sheet – snowline elevations at the end of the melt seasons from 2000 to 2017, Geological Survey of Denmark and Greenland Bulletin, 41, 71–74, 2018.

Fausto, R. S., van As, D., Mankoff, K. D., Vandecrux, B., Citterio, M., Ahlstrøm, A. P., Andersen, S. B., Colgan, W., Karlsson, N. B., Kjeldsen, K. K., Korsgaard, N. J., Larsen, S. H., Nielsen, S., Pedersen, A. , Shields, C. L., Solgaard, A. M., and Box, J. E.: Programme

for Monitoring of the Greenland Ice Sheet (PROMICE) automatic weather station data, Earth System Science Data, 13, 3819–3845, https://doi.org/10.5194/essd-13-3819-2021, 2021.

Fetterer, F.; Knowles K.; Meier W.; Savoie M.; Windnagel A.: Sea Ice Index, Version 3, https://doi.org/10.7265/N5K072F8, 2017.

Fettweis, X. and Grailet, J.-F.: MAR (Modèle Atmosphérique Régional) version 3.14, https://doi.org/10.5281/ZENODO.13151274, language: en, 2024.

Fettweis, X., Hanna, E., Gallée, H., Huybrechts, P., and Erpicum, M.: Estimation of the Greenland ice sheet surface mass balance for the 20th and 21st centuries, The Cryosphere, 2, 117–129, https://doi.org/10.5194/tc-2-117-2008, 2008.

Fettweis, X., Tedesco, M., van den Broeke, M., and Ettema, J.: Melting trends over the Greenland ice sheet (1958–2009) from spaceborne microwave data and regional climate models, The Cryosphere, 5, 359–375, https://doi.org/10.5194/tc-5-359-2011, publisher: Copernicus GmbH, 2011.

Fettweis, X., Hofer, S., Krebs-Kanzow, U., Amory, C., Aoki, T., Berends, C. J., Born, A., Box, J. E., Delhasse, A., Fujita, K., Gierz, P., Goelzer, H., Hanna, E., Hashimoto, A., Huybrechts, P., Kapsch, M.-L., King, M. D., Kittel, C., Lang, C., Langen, P. L., Lenaerts, J. T. M., Liston, G. E., Lohmann, G., Mernild, S. H., Mikolajewicz, U., Modali, K., Mottram, R. H., Niwano, M., Noël, B., Ryan, J. C., Smith, A., Streffing, J., Tedesco, M., van de Berg, W. J., van den Broeke, M., van de Wal, R. S. W., van Kampenhout, L., Wilton, D., Wouters, B., Ziemen, F., and Zolles, T.: GrSMBMIP: intercomparison of the modelled 1980–2012 surface mass balance over the Greenland Ice Sheet, The Cryosphere, 14, 3935–3958, https://doi.org/10.5194/tc-14-3935-2020, publisher: Copernicus GmbH, 2020.

Freitag, J., Kipfstuhl, S., Weißbach, S., Karlsson, N. B., Münch, T., and Hörhold, M.: Accumulation rate of the NG2012 firn core, PANGAEA, https://doi.org/10.1594/PANGAEA.944514, 2022a.

Freitag, J., Kipfstuhl, S., Weißbach, S., Karlsson, N. B., Münch, T., and Hörhold, M.: Accumulation rate of the B23_2012 firn core, PANGAEA, https://doi.org/10.1594/PANGAEA.944513, 2022b.

Freitag, J., Kipfstuhl, S., Weißbach, S., Karlsson, N. B., Münch, T., and Hörhold, M.: Accumulation rate of the B18_2012 firn core, PANGAEA, https://doi.org/10.1594/PANGAEA.944454, 2022c.

Gallée, H. and Schayes, G.: Development of a Three-Dimensional Meso-γ Primitive Equation Model: Katabatic Winds Simulation in the Area of Terra Nova Bay, Antarctica, Monthly Weather Review, 122, 671–685, https://doi.org/10.1175/1520-0493(1994)122<0671:DOATDM>2.0.CO;2, publisher: American Meteorological Society Section: Monthly Weather Review, 1994.

Gan, R., Huang, G., and Hu, K.: The Diverse Impacts of El Niño on Northeastern Canada and Greenland Surface Air Temperatures, https://doi.org/10.1175/JCLI-D-22-0677.1, 2023.

Graeter, K. A., Osterberg, E. C., Ferris, D. G., Hawley, R. L., Marshall, H. P., Lewis, G., Meehan, T., McCarthy, F., Overly, T., and Birkel, S. D.: Ice Core Records of West Greenland Melt and Climate Forcing, Geophysical Research Letters, 45, 3164–3172, https://doi.org/10.1002/2017gl076641, 2018.

Haacker, J., Wouters, B., Fettweis, X., Glissenaar, I. A., and Box, J. E.: Atmospheric-river-induced foehn events drain glaciers on Novaya Zemlya, Nature Communications, 15, 7021, https://doi.org/10.1038/s41467-024-51404-8, publisher: Nature Publishing Group, 2024.

Hammer, C. U. and Dahl-Jensen, D.: GRIP Accumulation Rates, PANGAEA, https://doi.org/10.1594/PANGAEA.55084, 1999.

Hanna, E., Huybrechts, P., Janssens, I., Cappelen, J., Steffen, K., and Stephens, A.: Runoff and mass balance of the Greenland ice sheet: 1958–2003, Journal of Geophysical Research: Atmospheres, 110, https://doi.org/10.1029/2004JD005641, 2005.

Hanna, E., McConnell, J., Das, S., Cappelen, J., and Stephens, A.: Observed and Modeled Greenland Ice Sheet Snow Accumulation, 1958–2003, and Links with Regional Climate Forcing, Journal of Climate, 19, 344–358, https://doi.org/10.1175/jcli3615.1, 2006.

Hanna, E., Huybrechts, P., Steffen, K., Cappelen, J., Huff, R., Shuman, C., Irvine-Fynn, T., Wise, S., and Griffiths, M.: Increased Runoff from Melt from the Greenland Ice Sheet: A Response to Global Warming, https://doi.org/10.1175/2007JCLI1964.1, 2008.

Hanna, E., Huybrechts, P., Cappelen, J., Steffen, K., Bales, R. C., Burgess, E., McConnell, J. R., Peder Steffensen, J., Van Den Broeke, M., Wake, L., Bigg, G., Griffiths, M., and Savas, D.: Greenland Ice Sheet surface mass balance 1870 to 2010 based on Twentieth Century Reanalysis, and links with global climate forcing: GREENLAND ICE SHEET MASS BALANCE, Journal of Geophysical Research: Atmospheres, 116, https://doi.org/10.1029/2011JD016387, 2011.

Hanna, E., Cropper, T. E., Hall, R. J., and Cappelen, J.: Greenland Blocking Index 1851–2015: a regional climate change signal, International Journal of Climatology, 36, 4847–4861, https://doi.org/10.1002/joc.4673, _eprint: https://rmets.onlinelibrary.wiley.com/doi/pdf/10.1002/joc.4673, 2016.

Hanna, E., Topál, D., Box, J. E., Buzzard, S., Christie, F. D. W., Hvidberg, C., Morlighem, M., De Santis, L., Silvano, A., Colleoni, F., Sasgen, I., Banwell, A. F., van den Broeke, M. R., DeConto, R., De Rydt, J., Goelzer, H., Gossart, A., Gudmundsson, G. H., Lindbäck, K., Miles, B., Mottram, R., Pattyn, F., Reese, R., Rignot, E., Srivastava, A., Sun, S., Toller, J., Tuckett, P. A., and Ultee, L.: Short- and long-term variability of the Antarctic and Greenland ice sheets, Nature Reviews Earth & Environment, 5, 193–210, https://doi.org/10.1038/s43017-023-00509-7, 2024.

Harper, J., Saito, J., and Humphrey, N.: Cold Season Rain Event Has Impact on Greenland's Firn Layer Comparable to Entire Summer Melt Season, Geophysical Research Letters, 50, e2023GL103 654, https://doi.org/10.1029/2023GL103654, 2023.

Hawley, R. L., Courville, Z. R., Kehrl, L. M., Lutz, E. R., Osterberg, E. C., Overly, T. B., and Wong, G. J.: Recent accumulation variability in northwest Greenland from ground-penetrating radar and shallow cores along the Greenland Inland Traverse, Journal of Glaciology, 60, 375–382, https://doi.org/10.3189/2014jog13j141, 2014.

Hermann, M., Box, J. E., Fausto, R. S., Colgan, W. T., Langen, P. L., Mottram, R., Wuite, J., Noël, B., van den Broeke, M. R., and van As, D.: Application of PROMICE Q-Transect in Situ Accumulation and Ablation Measurements (2000–2017) to Constrain Mass Balance at the Southern Tip of the Greenland Ice Sheet, Journal of Geophysical Research: Earth Surface, 123, 1235–1256, https://doi.org/10.1029/2017JF004408, 2018.

Herrera, S., Fita, L., Fernández, J., and Gutiérrez, J. M.: Evaluation of the mean and extreme precipitation regimes from the ENSEMBLES regional climate multimodel simulations over Spain, Journal of Geophysical Research: Atmospheres, 115, https://doi.org/10.1029/2010jd013936, 2010.

Hersbach, H., Bell, W., Berrisford, P., Horányi, A., J., M.-S., Nicolas, J., Radu, R., Schepers, D., Simmons, A., Soci, C., and Dee, D.: Global reanalysis: goodbye ERA-Interim, hello ERA5, https://doi.org/10.21957/VF291HEHD7, publisher: ECMWF, 2019.

Hersbach, H., Bell, B., Berrisford, P., Hirahara, S., Horányi, A., Muñoz-Sabater, J., Nicolas, J., Peubey, C., Radu, R., Schepers, D., Simmons, A., Soci, C., Abdalla, S., Abellan, X., Balsamo, G., Bechtold, P., Biavati, G., Bidlot, J., Bonavita, M., De Chiara, G., Dahlgren, P., Dee, D., Diamantakis, M., Dragani, R., Flemming, J., Forbes, R., Fuentes, M., Geer, A., Haimberger, L., Healy, S., Hogan, R. J., Hólm, E., Janisková, M., Keeley, S., Laloyaux, P., Lopez, P., Lupu, C., Radnoti, G., de Rosnay, P., Rozum, I., Vamborg, F., Villaume, S., and Thépaut, J.-N.: The ERA5 global reanalysis, Quarterly Journal of the Royal Meteorological Society, 146, 1999–2049, https://doi.org/10.1002/qj.3803, _eprint: https://rmets.onlinelibrary.wiley.com/doi/pdf/10.1002/qj.3803, 2020.

Hofer, S., Lang, C., Amory, C., Kittel, C., Delhasse, A., Tedstone, A., and Fettweis, X.: Greater Greenland Ice Sheet contribution to global sea level rise in CMIP6, Nature Communications, 11, 6289, https://doi.org/10.1038/s41467-020-20011-8, 2020.

Howat, I. M., de la Peña, S., Desilets, D., and Womack, G.: Autonomous ice sheet surface mass balance measurements from cosmic rays, The Cryosphere, 12, 2099–2108, https://doi.org/10.5194/tc-12-2099-2018, 2018.

Huai, B., van den Broeke, M. R., Reijmer, C. H., and Noël, B.: A Daily 1-km Resolution Greenland Rainfall Climatology (1958–2020) From Statistical Downscaling of a Regional Atmospheric Climate Model, Journal of Geophysical Research: Atmospheres, 127, e2022JD036 688, https://doi.org/10.1029/2022JD036688, _eprint: https://agupubs.onlinelibrary.wiley.com/doi/pdf/10.1029/2022JD036688, 2022.

Huang, B., Thorne, P. W., Banzon, V. F., Boyer, T., Chepurin, G., Lawrimore, J. H., Menne, M. J., Smith, T. M., Vose, R. S., and Zhang, H.-M.: Extended Reconstructed Sea Surface Temperature, Version 5 (ERSSTv5): Upgrades, Validations, and Intercomparisons, https://doi.org/10.1175/JCLI-D-16-0836.1, section: Journal of Climate, 2017.

Intergovernmental Panel On Climate Change, ed.: Climate Change 2013 – The Physical Science Basis: Working Group I Contribution to the Fifth Assessment Report of the Intergovernmental Panel on Climate Change, Cambridge University Press, 1 edn., ISBN 978-1-107-05799-9 978-1-107-66182-0 978-1-107-41532-4, https://www.cambridge.org/core/product/identifier/9781107415324/type/book, 2014.

Isaksen, K., Nordli, , Ivanov, B., Køltzow, M. A. , Aaboe, S., Gjelten, H. M., Mezghani, A., Eastwood, S., Førland, E., Benestad, R. E., Hanssen-Bauer, I., Brækkan, R., Sviashchennikov, P., Demin, V., Revina, A., and Karandasheva, T.: Exceptional warming over the Barents area, Scientific Reports, 12, 9371, https://doi.org/10.1038/s41598-022-13568-5, publisher: Nature Publishing Group, 2022.

Jia, Y., Xiao, K., Lin, M., and Zhang, X.: Analysis of Global Sea Level Change Based on Multi-Source Data, Remote Sensing, 14, 4854, https://doi.org/10.3390/rs14194854, 2022.

Kawakami, K., Iizuka, Y., Sasage, M., Matsumoto, M., Saito, T., Hori, A., Ishino, S., Fujita, S., Fujita, K., Takasugi, K., Hatakeyama, T., Hamamoto, S., Watari, A., Esashi, N., Otsuka, M., Uemura, R., Horiuchi, K., Minowa, M., Hattori, S., Aoki, T., Hirabayashi, M., Kawamura, K., and Matoba, S.: SE-Dome II Ice Core Dating With Half-Year Precision: Increasing Melting Events From 1799 to 2020 in Southeastern Greenland, Journal of Geophysical Research: Atmospheres, 128, https://doi.org/10.1029/2023jd038874, 2023.

Khan, S. A., Aschwanden, A., Bjørk, A. A., Wahr, J., Kjeldsen, K. K., and Kjær, K. H.: Greenland ice sheet mass balance: a review, Reports on Progress in Physics, 78, 046 801, https://doi.org/10.1088/0034-4885/78/4/046801, 2015.

Kjær, H., Zens, P., Edwards, R., Olesen, M., Mottram, R., Lewis, G., Holme, C., Black, S., Lund, K., Schmidt, M., Dahl-Jensen, D., Vinther, B., Svensson, A., Karlsson, N., Box, J., Kipfstuhl, S., and Vallelonga, P.: Recent North Greenland temperature warming and accumulation, 2021.

Koenig, L. S., Ivanoff, A., Alexander, P. M., MacGregor, J. A., Fettweis, X., Panzer, B., Paden, J. D., Forster, R. R., Das, I., McConnell, J. R., Tedesco, M., Leuschen, C., and Gogineni, P.: Annual Greenland accumulation rates (2009–2012) from airborne snow radar, The Cryosphere, 10, 1739–1752, https://doi.org/10.5194/tc-10-1739-2016, 2016.

Kokhanovsky, A., Vandecrux, B., Wehrlé, A., Danne, O., Brockmann, C., and Box, J. E.: An Improved Retrieval of Snow and Ice Properties Using Spaceborne OLCI/S-3 Spectral Reflectance Measurements: Updated Atmospheric Correction and Snow Impurity Load Estimation, Remote Sensing, 15, 77, https://doi.org/10.3390/rs15010077, publisher: Multidisciplinary Digital Publishing Institute, 2023.

Kopec, B. G., Feng, X., Michel, F. A., and Posmentier, E. S.: Influence of sea ice on Arctic precipitation, Proceedings of the National Academy of Sciences, 113, 46–51, https://doi.org/10.1073/pnas.1504633113, 2016.

Køltzow, M., Schyberg, H., Støylen, E., and Yang, X.: Value of the Copernicus Arctic Regional Reanalysis (CARRA) in representing near-surface temperature and wind speed in the north-east European Arctic, Polar Research, 41, https://doi.org/10.33265/polar.v41.8002, 2022.

Langen, P. L., Mottram, R. H., Christensen, J. H., Boberg, F., Rodehacke, C. B., Stendel, M., As, D. v., Ahlstrøm, A. P., Mortensen, J., Rysgaard, S., Petersen, D., Svendsen, K. H., Aðalgeirsdóttir, G., and Cappelen, J.: Quantifying Energy and Mass Fluxes Controlling Godthåbsfjord Freshwater Input in a 5-km Simulation (1991–2012), https://doi.org/10.1175/JCLI-D-14-00271.1, 2015.

Langen, P. L., Fausto, R. S., Vandecrux, B., Mottram, R. H., and Box, J. E.: Liquid Water Flow and Retention on the Greenland Ice Sheet in the Regional Climate Model HIRHAM5: Local and Large-Scale Impacts, Frontiers in Earth Science, 4, https://doi.org/10.3389/feart.2016.00110, 2017.

Lenssen, N., Schmidt, G. A., Hendrickson, M., Jacobs, P., Menne, M. J., and Ruedy, R.: A NASA GISTEMPv4 Observational Uncertainty Ensemble, Journal of Geophysical Research: Atmospheres, 129, e2023JD040 179, https://doi.org/10.1029/2023JD040179, _eprint: https://agupubs.onlinelibrary.wiley.com/doi/pdf/10.1029/2023JD040179, 2024.

Lewis, G., Osterberg, E., Hawley, R., Whitmore, B., Marshall, H. P., and Box, J.: Regional Greenland accumulation variability from Operation IceBridge airborne accumulation radar, The Cryosphere, 11, 773–788, https://doi.org/10.5194/tc-11-773-2017, 2017.

Lewis, G., Osterberg, E., Hawley, R., Marshall, H. P., Meehan, T., Graeter, K., McCarthy, F., Overly, T., Thundercloud, Z., and Ferris, D.: Recent precipitation decrease across the western Greenland ice sheet percolation zone, The Cryosphere, 13, 2797–2815, https://doi.org/10.5194/tc-13-2797-2019, 2019.

Lucas-Picher, P., Wulff-Nielsen, M., Christensen, J. H., Aðalgeirsdóttir, G., Mottram, R., and Simonsen, S. B.: Very high resolution regional climate model simulations over Greenland: Identifying added value, Journal of Geophysical Research: Atmospheres, 117, https://doi.org/10.1029/2011JD016267, 2012.

Luetzenburg, G., Korsgaard, N. J., Deichmann, A. K., Socher, T., Gleie, K., Scharffenberger, T., Meyer, R. P., Fahrner, D., Nielsen, E. B., How, P., Bjørk, A. A., Kjeldsen, K. K., Ahlstrøm, A. P., and Fausto, R. S.: PROMICE-2022 Ice Mask: A high-resolution outline of the Greenland Ice Sheet from August 2022, Earth System Science Data Discussions, pp. 1–23, https://doi.org/10.5194/essd-2025-415, publisher: Copernicus GmbH, 2025.

Machguth, H., MacFerrin, M., van As, D., Box, J. E., Charalampidis, C., Colgan, W., Fausto, R. S., Meijer, H. A. J., Mosley-Thompson, E., and van de Wal, R. S. W.: Greenland meltwater storage in firn limited by near-surface ice formation, Nature Climate Change, 6, 390–393, https://doi.org/10.1038/nclimate2899, 2016.

Matsumura, S., Yamazaki, K., and Suzuki, K.: Slow-down in summer warming over Greenland in the past decade linked to central Pacific El Niño, Communications Earth & Environment, 2, 1–8, https://doi.org/10.1038/s43247-021-00329-x, 2021.

McConnell, J. R., Lamorey, G., Hanna, E., Mosley-Thompson, E., Bales, R. C., Belle-Oudry, D., and Kyne, J. D.: Annual net snow accumulation over southern Greenland from 1975 to 1998, Journal of Geophysical Research: Atmospheres, 106, 33 827–33 837, https://doi.org/10.1029/2001JD900129, 2001.

Medley, B., Joughin, I., Das, S. B., Steig, E. J., Conway, H., Gogineni, S., Criscitiello, A. S., McConnell, J. R., Smith, B. E., van den Broeke, M. R., Lenaerts, J. T. M., Bromwich, D. H., and Nicolas, J. P.: Airborne-radar and ice-core observations of annual snow accumulation over Thwaites Glacier, West Antarctica confirm the spatiotemporal variability of global and regional atmospheric models, Geophysical Research Letters, 40, 3649–3654, https://doi.org/10.1002/grl.50706, 2013.

Miege, C., R. Forster, R., E. Box, J., W. Burgess, E., R. McConnell, J., R. Pasteris, D., and B. Spikes, V.: SE Greenland snow accumulation rates from GPR and 3 firn cores, https://doi.org/10.18739/A2ST7DX47, 2014.

Miller, H. and Schwager, M.: Accumulation rate and stable oxygen isotope ratios of ice core ngt14C93.2 from the North Greenland Traverse, PANGAEA, p. N/A, https://doi.org/10.1594/PANGAEA.57158, 2000a.

Miller, H. and Schwager, M.: Accumulation rate and stable oxygen isotope ratios of ice core ngt27C94.2 from the North Greenland Traverse, PANGAEA, https://doi.org/10.1594/PANGAEA.57291, 2000b.

Miller, H. and Schwager, M.: Accumulation rate and stable oxygen isotope ratios of ice core ngt37C95.2 from the North Greenland Traverse, PANGAEA, https://doi.org/10.1594/PANGAEA.57297, 2000c.

Miller, H. and Schwager, M.: Accumulation rate and stable oxygen isotope ratios of ice core ngt42C95.2 from the North Greenland Traverse, PANGAEA, https://doi.org/10.1594/PANGAEA.57654, 2000d.

Miller, H. and Schwager, M.: Accumulation rate and stable oxygen isotope ratios of ice core ngt03C93.2 from the North Greenland Traverse, PANGAEA, p. N/A, https://doi.org/10.1594/PANGAEA.218274, 2004.

Miège, C., Forster, R. R., Box, J. E., Burgess, E. W., Mcconnell, J. R., Pasteris, D. R., and Spikes, V. B.: Southeast Greenland high accumulation rates derived from firn cores and ground-penetrating radar, Annals of Glaciology, 54, 322–332, https://doi.org/10.3189/2013AoG63A358, publisher: Cambridge University Press, 2013.

Montgomery, L., Koenig, L., Lenaerts, J. T. M., and Kuipers Munneke, P.: Accumulation rates (2009–2017) in Southeast Greenland derived from airborne snow radar and comparison with regional climate models, Annals of Glaciology, 61, 225–233, https://doi.org/10.1017/aog.2020.8, 2020.

Morice, C. P., Kennedy, J. J., Rayner, N. A., Winn, J. P., Hogan, E., Killick, R. E., Dunn, R. J. H., Osborn, T. J., Jones, P. D., and Simpson, I. R.: An Updated Assessment of Near-Surface Temperature Change From 1850: The HadCRUT5 Data Set, Journal of Geophysical Research: Atmospheres, 126, e2019JD032 361, https://doi.org/10.1029/2019JD032361, 2021.

Mosley-Thompson, E., McConnell, J. R., Bales, R. C., Li, Z., Lin, P.-N., Steffen, K., Thompson, L. G., Edwards, R., and Bathke, D.: Local to regional-scale variability of annual net accumulation on the Greenland ice sheet from PARCA cores, Journal of Geophysical Research: Atmospheres, 106, 33 839–33 851, https://doi.org/10.1029/2001JD900067, 2001.

Mouginot, J., Rignot, E., Bjørk, A. A., van den Broeke, M., Millan, R., Morlighem, M., Noël, B., Scheuchl, B., and Wood, M.: Forty-six years of Greenland Ice Sheet mass balance from 1972 to 2018, Proceedings of the National Academy of Sciences, 116, 9239–9244, https://doi.org/10.1073/pnas.1904242116, 2019.

Nicola, L., Notz, D., and Winkelmann, R.: Revisiting temperature sensitivity: how does Antarctic precipitation change with temperature?, The Cryosphere, 17, 2563–2583, https://doi.org/10.5194/tc-17-2563-2023, 2023.

Niwano, M., Yamaguchi, S., Yamasaki, T., and Aoki, T.: Near-surface snow physics data from SIGMA-Traverse 2018, Arctic Data archive System (ADS), Japan, N/A, N/A, https://doi.org/10.17592/001.2020091101, 2020.

Noël, B., Van De Berg, W. J., Lhermitte, S., Wouters, B., Schaffer, N., and Van Den Broeke, M. R.: Six Decades of Glacial Mass Loss in the Canadian Arctic Archipelago, Journal of Geophysical Research: Earth Surface, 123, 1430–1449, https://doi.org/10.1029/2017JF004304, 2018.

Ohmura, A. and Reeh, N.: New precipitation and accumulation maps for Greenland, Journal of Glaciology, 37, 140–148, https://doi.org/10.3189/S0022143000042891, 1991.

Ohmura, A., Calanca, P., Wild, M., and Anklin, M.: Precipitation, accumulation and mass balance of the Greenland ice sheet, Zeitschrift fur Gletscherkunde und Glazialgeologie, 35, 1–20, https://cir.nii.ac.jp/crid/1573668925528684544, 1999.

Osman, M. B., Coats, S., Das, S. B., McConnell, J. R., and Chellman, N.: North Atlantic jet stream projections in the context of the past 1,250 years, Proceedings of the National Academy of Sciences, 118, https://doi.org/10.1073/pnas.2104105118, 2021.

Otosaka, I. N., Shepherd, A., Ivins, E. R., Schlegel, N.-J., Amory, C., van den Broeke, M. R., Horwath, M., Joughin, I., King, M. D., Krinner, G., Nowicki, S., Payne, A. J., Rignot, E., Scambos, T., Simon, K. M., Smith, B. E., Sørensen, L. S., Velicogna, I., Whitehouse, P. L., A, G., Agosta, C., Ahlstrøm, A. P., Blazquez, A., Colgan, W., Engdahl, M. E., Fettweis, X., Forsberg, R., Gallée, H., Gardner, A., Gilbert, L., Gourmelen, N., Groh, A., Gunter, B. C., Harig, C., Helm, V., Khan, S. A., Kittel, C., Konrad, H., Langen, P. L., Lecavalier, B. S., Liang, C.-C., Loomis, B. D., McMillan, M., Melini, D., Mernild, S. H., Mottram, R., Mouginot, J., Nilsson, J., Noël, B., Pattle, M. E., Peltier, W. R., Pie, N., Roca, M., Sasgen, I., Save, H. V., Seo, K.-W., Scheuchl, B., Schrama, E. J. O., Schröder, L., Simonsen, S. B., Slater, T., Spada, G.,

Sutterley, T. C., Vishwakarma, B. D., van Wessem, J. M., Wiese, D., van der Wal, W., and Wouters, B.: Mass balance of the Greenland and Antarctic ice sheets from 1992 to 2020, Earth System Science Data, 15, 1597–1616, https://doi.org/10.5194/essd-15-1597-2023, 2023.

Ridder, K. D. and Schayes, G.: The IAGL Land Surface Model, Journal of Applied Meteorology and Climatology, 36, 167–182, https://doi.org/10.1175/1520-0450(1997)036<0167:TILSM>2.0.CO;2, publisher: American Meteorological Society Section: Journal of Applied Meteorology and Climatology, 1997.

Robin, G. D. Q., Evans, S., and Bailey, J. T.: Interpretation of Radio Echo Sounding in Polar Ice Sheets, Philosophical Transactions of the Royal Society of London. Series A, Mathematical and Physical Sciences, 265, 437–505, https://www.jstor.org/stable/73767, 1969.

Robinson, A., Calov, R., and Ganopolski, A.: Multistability and critical thresholds of the Greenland ice sheet, Nature Climate Change, 2, 429–432, https://doi.org/10.1038/nclimate1449, 2012.

Roeckner, E., Bäuml, G., Bonaventura, L., Brokopf, R., Esch, M., Giorgetta, M., Hagemann, S., Kirchner, I., Kornblueh, L., Manzini, E., Rhodin, A., Schlese, U., Schulzweida, U., and Tompkins, A.: The atmospheric general circulation model ECHAM 5. PART I: Model description, https://doi.org/10.17617/2.995269, 2003.

Rohde, R. A. and Hausfather, Z.: The Berkeley Earth Land/Ocean Temperature Record, Earth System Science Data, 12, 3469–3479, https://doi.org/10.5194/essd-12-3469-2020, publisher: Copernicus GmbH, 2020.

Ryan, J. C., Smith, L. C., Wu, M., Cooley, S. W., Miège, C., Montgomery, L. N., Koenig, L. S., Fettweis, X., Noel, B. P. Y., and van den Broeke, M. R.: Evaluation of CloudSat's Cloud-Profiling Radar for Mapping Snowfall Rates Across the Greenland Ice Sheet, Journal of Geophysical Research: Atmospheres, 125, e2019JD031 411, https://doi.org/10.1029/2019JD031411, _eprint: https://agupubs.onlinelibrary.wiley.com/doi/pdf/10.1029/2019JD031411, 2020.

Sandberg Sørensen, L., Simonsen, S. B., Forsberg, R., Khvorostovsky, K., Meister, R., and Engdahl, M. E.: 25 years of elevation changes of the Greenland Ice Sheet from ERS, Envisat, and CryoSat-2 radar altimetry, Earth and Planetary Science Letters, 495, 234–241, https://doi.org/10.1016/j.epsl.2018.05.015, 2018.

Schaller, C. F., Freitag, J., Kipfstuhl, S., Laepple, T., Steen-Larsen, H. C., and Eisen, O.: A representative density profile of the North Greenland snowpack, The Cryosphere, 10, 1991–2002, https://doi.org/10.5194/tc-10-1991-2016, 2016.

Schmidt, L. S., Schuler, T. V., Thomas, E. E., and Westermann, S.: Meltwater runoff and glacier mass balance in the high Arctic: 1991–2022 simulations for Svalbard, The Cryosphere, 17, 2941–2963, https://doi.org/10.5194/tc-17-2941-2023, 2023.

Schyberg, H., Yang, X., Køltzow, M. A. , Amstrup, B., Bakketun, , Bazile, E., Bojarova, J., Box, J. E., Dahlgren, P., Hagelin, S., Homleid, M., Horányi, A., Høyer, J., Johansson, , Killie, M. A., Körnich, H., Le Moigne, P., Lindskog, M., Manninen, T., Nielsen Englyst, P., Nielsen, K. P., Olsson, E., Palmason, B., Peralta Aros, C., Randriamampianina, R., Samuelsson, P., Stappers, R., Støylen, E., Thorsteinsson, S., Valkonen, T., and Wang, Z. Q.: Arctic regional reanalysis on single levels from 1991 to present, https://doi.org/10.24381/cds.713858f6, 2020.

Shepherd, A., Ivins, E. R., A, G., Barletta, V. R., Bentley, M. J., Bettadpur, S., Briggs, K. H., Bromwich, D. H., Forsberg, R., Galin, N., Horwath, M., Jacobs, S., Joughin, I., King, M. A., Lenaerts, J. T. M., Li, J., Ligtenberg, S. R. M., Luckman, A., Luthcke, S. B., McMillan, M., Meister, R., Milne, G., Mouginot, J., Muir, A., Nicolas, J. P., Paden, J., Payne, A. J., Pritchard, H., Rignot, E., Rott, H., Sørensen, L. S., Scambos, T. A., Scheuchl, B., Schrama, E. J. O., Smith, B., Sundal, A. V., van Angelen, J. H., van de Berg, W. J., van den Broeke, M. R., Vaughan, D. G., Velicogna, I., Wahr, J., Whitehouse, P. L., Wingham, D. J., Yi, D., Young, D., and Zwally, H. J.: A Reconciled Estimate of Ice-Sheet Mass Balance, Science, 338, 1183–1189, https://doi.org/10.1126/science.1228102, 2012.

Simmons, A. J. and Gibson, J. K.: ERA-40 Project Report Series No., 2000.

Steig, E. J., Mayewski, P. A., Dixon, D. A., Kaspari, S. D., Frey, M. M., Schneider, D. P., Arcone, S. A., Hamilton, G. S., Spikes, V. B., Albert, M., Meese, D., Gow, A. J., Shuman, C. A., White, J. W. C., Sneed, S., Flaherty, J., and Wumkes, M.: High-resolution ice cores from US ITASE (West Antarctica): development and validation of chronologies and determination of precision and accuracy, Annals of Glaciology, 41, 77–84, https://doi.org/10.3189/172756405781813311, 2005.

Tedesco, M. and Fettweis, X.: Unprecedented atmospheric conditions (1948–2019) drive the 2019 exceptional melting season over the Greenland ice sheet, The Cryosphere, 14, 1209–1223, https://doi.org/10.5194/tc-14-1209-2020, 2020.

The IMBIE Team: Mass balance of the Greenland Ice Sheet from 1992 to 2018, Nature, 579, 233–239, https://doi.org/10.1038/s41586-019-1855-2, 2020.

Undén, P., Rontu, L., Jarvinen, H., Lynch, P., Calvo Sánchez, F. J., Cats, G., Cuxart, J., Eerola, K., Fortelius, C., García-Moya, J. A., Jones, C., Lenderink, G., McDonald, A., McGrath, R., Navascués, B., Woetman-Nielsen, N., Odegaard, V., Rodríguez Camino, E., Rummukainen, M., Room, R., Sattler, K., Hansen Sass, B., Savijärvi, H., Wichers Schreur, B., Sigg, R., Han, T., and Tijm, A.: HIRLAM-5 Scientific documentation, https://repositorio.aemet.es/handle/20.500.11765/6323, 2002.

van Dalum, C. T., van de Berg, W. J., Gadde, S. N., van Tiggelen, M., van der Drift, T., van Meijgaard, E., van Ulft, L. H., and van den Broeke, M. R.: First results of the polar regional climate model RACMO2.4, The Cryosphere, 18, 4065–4088, https://doi.org/10.5194/tc-18-4065-2024, 2024.

van den Broeke, M., Bamber, J., Ettema, J., Rignot, E., Schrama, E., van de Berg, W. J., van Meijgaard, E., Velicogna, I., and Wouters, B.: Partitioning Recent Greenland Mass Loss, Science, 326, 984–986, https://doi.org/10.1126/science.1178176, 2009.

van den Broeke, M., Box, J., Fettweis, X., Hanna, E., Noël, B., Tedesco, M., van As, D., van de Berg, W. J., and van Kampenhout, L.: Greenland Ice Sheet Surface Mass Loss: Recent Developments in Observation and Modeling, Current Climate Change Reports, 3, 345–356, https://doi.org/10.1007/s40641-017-0084-8, 2017.

van den Broeke, M. R., Enderlin, E. M., Howat, I. M., Kuipers Munneke, P., Noël, B. P. Y., van de Berg, W. J., van Meijgaard, E., and Wouters, B.: On the recent contribution of the Greenland ice sheet to sea level change, The Cryosphere, 10, 1933–1946, https://doi.org/10.5194/tc-10-1933-2016, 2016.

van der Schot, J., Abermann, J., Silva, T., Rasmussen, K., Winkler, M., Langley, K., and Schöner, W.: Seasonal snow cover indicators in coastal Greenland from in situ observations, a climate model, and reanalysis, The Cryosphere, 18, 5803–5823, https://doi.org/10.5194/tc-18-5803-2024, 2024.

Vandecrux, B., MacFerrin, M., Machguth, H., Colgan, W. T., van As, D., Heilig, A., Stevens, C. M., Charalampidis, C., Fausto, R. S., Morris, E. M., Mosley-Thompson, E., Koenig, L., Montgomery, L. N., Miège, C., Simonsen, S. B., Ingeman-Nielsen, T., and Box, J. E.: Firn data compilation reveals widespread decrease of firn air content in western Greenland, The Cryosphere, 13, 845–859, https://doi.org/10.5194/tc-13-845-2019, publisher: Copernicus GmbH, 2019.

Vandecrux, B., Box, J., Ahlstrøm, A., Fausto, R., Karlsson, N., Rutishauser, A., Citterio, M., Larsen, S., Heuer, J., Solgaard, A., How, P., Colgan, W., and Fahrner, D.: GEUS snow and firn data in Greenland, GEUS Dataverse, https://doi.org/10.22008/FK2/9QEOWZ, 2023a.

Vandecrux, B., Box, J. E., Ahlstrøm, A. P., Andersen, S. B., Bayou, N., Colgan, W. T., Cullen, N. J., Fausto, R. S., Haas-Artho, D., Heilig, A., Houtz, D. A., How, P., Iosifescu Enescu, I., Karlsson, N. B., Kurup Buchholz, R., Mankoff, K. D., McGrath, D., Molotch, N. P., Perren, B., Revheim, M. K., Rutishauser, A., Sampson, K., Schneebeli, M., Starkweather, S., Steffen, S., Weber, J., Wright, P. J., Zwally, H. J., and Steffen, K.: The historical Greenland Climate Network (GC-Net) curated and augmented level-1 dataset, Earth System Science Data, 15, 5467–5489, https://doi.org/10.5194/essd-15-5467-2023, 2023b.

Vandecrux, B., Amory, C., Ahlstrøm, A. P., Akers, P. D., Albert, M., Alley, R. B., Castro, M. A. d., Arnaud, L., Baker, I., Bales, R., Benson, C., Box, J. E., Brucker, L., Buizert, C., Chandler, D., Charalampidis, C., Cherblanc, C., Clerx, N., Colgan, W., Covi, F., Dattler, M., Denis, G., Derksen, C., Dibb, J. E., Ding, M., Dixon, D., Eisen, O., Fahrner, D., Fausto, R., Favier, V., Fernandoy, F., Freitag, J., Gerland, S., Harper, J., Hawley, R. L., Heuer, J., Hock, R., Hou, S., How, P., Humphrey, N., Hubbard, B., Iizuka, Y., Isaksson, E., Kameda, T., Karlsson, N. B., Kawakami, K., Kjær, H. A., Kreutz, K., Munneke, P. K., Lazzara, M., Lemeur, E., Lenaerts, J. T. M., Lewis, G., Lindau, F. G. L., Lindsey-Clark, J., MacFerrin, M., Machguth, H., Magand, O., Mankoff, K. D., Marquetto, L., Martinerie, P., McConnell, J. R., Medley, B., Miège, C., Miles, K. E., Miller, O., Miller, H., Montgomery, L., Morris, E., Mosley-Thompson, E., Mulvaney, R., Niwano, M., Oerter, H., Osterberg, E., Otosaka, I., Picard, G., Polashenski, C., Reijmer, C., Rennermalm, A., Rutishauser, A., Scanlan, K., Simoes, J. C., Simonsen, S. B., Smeets, P. C. J. P., Smith, A., Solgaard, A., Spencer, M., Steen-Larsen, H. C., Stevens, C. M., Sugiyama, S., Svensson, J., Tedesco, M., Thomas, E., Thompson-Munson, M., Tsutaki, S., As, D. v., Broeke, M. R. V. d., Tiggelen, M. v., Wang, Y., Wilhelms, F., Winstrup, M., Xiao, J., and Xiao, C.: The SUMup collaborative database: Surface mass balance, subsurface temperature and density measurements from the Greenland and Antarctic ice sheets (2024 release), https://arcticdata.io/catalog/view/doi%3A10.18739%2FA2M61BR5M, 2024.

Velicogna, I., Sutterley, T. C., and van den Broeke, M. R.: Regional acceleration in ice mass loss from Greenland and Antarctica using GRACE time-variable gravity data, Geophysical Research Letters, 41, 8130–8137, https://doi.org/10.1002/2014GL061052, 2014.

Vernon, C. L., Bamber, J. L., Box, J. E., van den Broeke, M. R., Fettweis, X., Hanna, E., and Huybrechts, P.: Surface mass balance model intercomparison for the Greenland ice sheet, The Cryosphere, 7, 599–614, https://doi.org/10.5194/tc-7-599-2013, 2013.

Vinther, B. M., Freitag, J., Kipfstuhl, S., Weißbach, S., Karlsson, N. B., Münch, T., and Hörhold, M.: Accumulation rate of the B26_2011 firn core, PANGAEA, https://doi.org/10.1594/PANGAEA.945666, 2022.

Virtanen, P., Gommers, R., Oliphant, T. E., Haberland, M., Reddy, T., Cournapeau, D., Burovski, E., Peterson, P., Weckesser, W., Bright, J., van der Walt, S. J., Brett, M., Wilson, J., Millman, K. J., Mayorov, N., Nelson, A. R. J., Jones, E., Kern, R., Larson, E., Carey, C. J., Polat, , Feng, Y., Moore, E. W., VanderPlas, J., Laxalde, D., Perktold, J., Cimrman, R., Henriksen, I., Quintero, E. A., Harris, C. R., Archibald, A. M., Ribeiro, A. H., Pedregosa, F., and van Mulbregt, P.: SciPy 1.0: fundamental algorithms for scientific computing in Python, Nature Methods, 17, 261–272, https://doi.org/10.1038/s41592-019-0686-2, 2020.

Wong, G. J., Osterberg, E. C., Hawley, R. L., Courville, Z. R., Ferris, D. G., and Howley, J. A.: Coast-to-interior gradient in recent northwest Greenland precipitation trends (1952–2012), Environmental Research Letters, 10, 114 008, https://doi.org/10.1088/1748-9326/10/11/114008, 2015.

Yang, X., Schyberg, H., Palmason, B., Bojarova, J., Box, J. E., Pagh Nielsen, K., Amstrup, B., Peralta, C., Høyer, J., Nielsen Englyst, P., Homleid, M., Køltzow, M. A. , Randriamampianina, R., Dahlgren, P., Støylen, E., Valkonen, T., Thorsteinsson, S., Körnich, H., Lindskog, M., and Mankoff, K.: C3S arctic regional reanalysis — full system documentation, Tech. rep., Copernicus Climate Change Service (C3S), ECMWF, https://confluence.ecmwf.int/display/CKB/Copernicus+Arctic+Regional+Reanalysis+%28CARRA%29%3A+Full+system+documentation, 2020.